4-27-2018

CMOS Integration of High Performance Quantum Dot Lasers For Silicon Photonics

Zihao Wang
zw4491@rit.edu

R.I.T

CMOS INTEGRATION OF HIGH PERFORMANCE QUANTUM DOT LASERS FOR SILICON PHOTONICS

by

ZIHAO WANG

A dissertation submitted in partial fulfillment of the requirements
for the degree of Doctor of Philosophy in Microsystems Engineering

Microsystems Engineering
Kate Gleason College of Engineering

Rochester Institute of Technology
Rochester, New York
April 27, 2018

NOTICE OF COPYRIGHT

REPRODUCTION PERMISSION STATEMENT

Permission Granted

TITLE:

"CMOS INTEGRATION OF HIGH PERFORMANCE QUANTUM DOT LASERS FOR SILICON PHOTONICS"

I, Zihao Wang, hereby grant permission to the Wallace Library of the Rochester Institute of Technology to reproduce my dissertation in whole or in part. Any reproduction will not be for commercial use or profit.

Signature of Author: _____Date: _____

CMOS Integration of High Performance Quantum Dot Lasers for Silicon Photonics

By

Zihao Wang

Committee Approval:

We, the undersigned committee members, certify that we have advised and/or supervised the candidate on the work described in this dissertation. We further certify that we have reviewed the dissertation manuscript and approve it in partial fulfillment of the requirements of the degree of Doctor of Philosophy in Microsystems Engineering.

_____

Dr. Stefan F. Preble — Date
Associate Professor, Microsystems Engineering (Advisor)

_____

Dr. Seth Hubbard — Date
Professor, Microsystems Engineering

_____

Dr. Jing Zhang — Date
Assistant Professor, Electrical and Microelectronic Engineering

_____

Dr. Parsian K. Mohseni — Date
Assistant Professor, Microsystems Engineering

_____

Dr. Pratik P. Dholabhai — Date
Assistant Professor, Physics and Astronomy

Certified by:

_____

Dr. Bruce W. Smith — Date
Director, Microsystems Engineering Program

ABSTRACT

Kate Gleason College of Engineering
Rochester Institute of Technology

Degree: Doctor of Philosophy **Program:** Microsystems Engineering

Name of Candidate: Zihao Wang

Name of Advisor: Stefan F. Preble
Degree: Doctor of Philosophy **Program:** Microsystems Engineering

Title: CMOS Integration of High Performance Quantum Dot Lasers for Silicon Photonics

Integration of III-V components on Si substrates is required for realizing the promise of Silicon Photonic systems. Specifically, the direct bandgap of many III-V materials is required for light sources, efficient modulators and photodetectors. Several different approaches have been taken to integrate III-V lasers into the silicon photonic platform, such as wafer bonding, direct growth, butt coupling, etc. Here, we have devised a novel laser design that overcomes the above limitations. In our approach, we use InAs quantum dot (QD) lasers monolithically integrated with silicon waveguides and other Si photonic passive components. Due to their unique structures, the QD lasers have been proven by several groups to have the combination of high temperature stability, large modulation bandwidth and low power consumption compared with their quantum well counterparts, which makes it an ideal candidate for Si photonic applications. The first section of this dissertation introduces the theory and novelty of QD lasers, the DC and RF characterization methods of QD lasers are also discussed. The second section is focused on the growth of QD gain chip which a broadband gain chip based on QD inhomogeneous broadening properties was demonstrated. In third section, the lasers devices are built on Si substrate by Pd wafer bonding technology. Firstly, a ridge waveguide QD laser is demonstrated in this section which have better heat dissipation and lower threshold current compared to the unbonded lasers. In section four, a on Si comb laser is also developed. Due to inhomogeneous broadening and ultrafast carrier dynamics, InAs quantum dots have key advantages that make them well suited for Mode-locked lasers (MLLs). In section five, a passively mode-locked InAs quantum dots laser on Si is achieved at a repetition rate of ~7.3 GHz under appropriate bias conditions. In section six, a butt-joint integration configuration based on QD lasers and silicon photonics ring resonator is tested by using to translation stage. In order to achieve the on chip butt-joint integration, an on chip laser facet was created in section seven. A novel facet etching method is developed by using Br-ion beam assist etching (Br-IBAE). In section eight, a Pd-GaAs butt-joint integration platform was proposed, a hybrid tunable QD laser which consist of a QD SOA gain chip butt joint coupled with a passive Si_3N_4 photonic integrated circuit is proof of concept by using an external booster SOA coupled with a Si_3N_4 ring reflector feedback circuit. The final section summarized the work discussed in this thesis and also discussed some future approaches by using QD lasers integrated with silicon photonics integrated circuits based on the Pd-GaAs wafer bonding butt-joint coupled platform.

DEDICATION

To my family

ACKNOWLDEDGMENTS

Time passed quickly, it is almost the six years of my graduate life at RIT and it's the time to start the new journey from here. I felt so fortunate to spend this period of time with my friends, advisors and colleagues here who made me still remain the original aspiration to the field of photonics as the time when I started here. Now it is my pleasure to thank all of you for the emotional supports, novel ideas, valuable experiences and technical guidance which keep me on the right track to complete the degree.

First of all, I would like to thank my advisor, Professor Stefan F. Preble, for giving me opportunity to work in his research group and supporting throughout my graduate studies. Stefan provides a flexible and freedom research environment to his group members which help us become more self-driven and independent researchers. His abundance of knowledge, rigorous attitude of scholarship, and hard-working spirit inspired each of his students, and I am privileged to be one of them.

I would like to express my deepest appreciation to Professor Seth Hubbard, Professor Jing Zhang, Professor Parsian K. Mohseni and Professor Pratik P.Dholabhai for serving as my dissertation committee, and for their generosity in sharing their invaluable opinions and all sorts of resources for the maximum good of my research.

I would like to thank the staff members at Cornell NanoScale Science and Technology Facility (CNF), and the staff members in the Semiconductor and Microsystems Fabrication Laboratory (SMFL), without them, I could not get my work done at all.

I want to express my gratitude to my former colleagues Dr. Liang Cao, Dr. Abdelsalam Aboketaf, Dr. Kaifeng Shi, and all the current colleagues in integrated photonics group: Dr.Pual Thomas, Dr. John Serafini, Mr.Md Ibrahim Khalil, Mr.Nathan Tiberio, and Mr. Nathan Rummage. And especially thanks to Mr. Jeffrey Steidle, Mr. Michael Fanto and Mr. Peichuan Yin for their help about the fabrications, characterization setups and their constructive suggestions, without them my experiments would not be progressing smoothly.

I want to express my thanks to all the other colleagues in Microsystems department. Especially, Dr. Michael Slocum, Dr.Steve Polly, Dr. Yushuai Dai, Zac Bittner from Nano PV group trained me to use their facilities. Thanks to Prof. Zhaolin Lu, generously shared his o-band tunable laser for my research. Thanks to Mr. Thomas Wilhelm, collaborated with me successfully developed the MAC etch process to AlGaAs/GaAs systems. Thanks to Prof Jiandi Wan, Dr. Rong Fan, Mr. Toby Mea, Mr. Xinye Chen, Mrs. Sitong Zhou for the collaboration to develop microfluidic enhanced TiO2 nanotube growth, red blood filtering masks and photonics biosensors. Thanks to Mr. Cheng Liu, also my friend from high school, for the collaboration to characterize the high speed UV LEDs. Thanks to Lisa Zimmerman for her help as staff specialist in Microsystems Engineering Ph.D. program.

I also would like to thank our collaborators outside RIT: Prof. Luke F. Lester from Virginia Tech provides us QD laser samples and helpful discussions for the MLL's project.

Dr. Xin Zhu from Matrix Opto Co., Ltd sent us dummy AlGaAs-GaAs epitaxy samples and Dr. Evan Chen from Enablence Technologies Inc. provided us their high speed laser samples.

Special thanks to my former advisor, Professor Wei Guo, who led me into the photonics field, specifically, the quantum dot lasers area. Although he joined Umass-Lowell in my second year of Ph.D., he still generous trained me to use their MBE facilities, shared us the laser cleaving tool and his thoughtful discussions on my research. I also would like to thank my former group members, Mr. Ruizhe Yao and Dr. Chi-sen Lee for their knowledge and guidance of MBE growth. Especially, Chi-sen generously shared with me his years of experience in quantum dots lasers growth, fabrication and characterizations.

Finally, I would thank my loving parents and grandparents, for being patient with me and being believing in me to spend years of study abroad, where 6600 miles away from them figuring out what I wanted to do in life.

TABLE OF CONTENTS

1 Introduction 1

1.1 The challenge of Moore's Law 1

1.2 Optical Interconnects 4

1.3 Silicon Photonics 5

1.4 Laser Integration with Silicon Photonics 6

1.5 Quantum Dot Lasers 8

1.6 Characterization of the semiconductor laser 11

1.6.1 Threshold current J_{th} and transparent current density J_{tr} ($J_{th,\infty}$) 11

1.6.2 Differential quantum efficiency $\eta_{d,}$ internal quantum efficiency η_i and internal loss α_i 11

1.6.3 Temperature dependence of threshold current 12

1.7 Dissertation overview 13

2 Dip-free Broadband InAs Quantum Dot Superluminescence Light Emitting Diodes 15

2.1 Introduction 16

2.2 Experiment 17

2.3 Characterization and Discussion 20

2.4 Conclusion....24

3 High Performance InAs Quantum Dot Lasers on Silicon Substrates by Low Temperature Pd-GaAs Wafer Bonding....25

3.1 Introduction....26

3.2 Experiment....27

3.3 Characterization and Discussion....29

3.4 Conclusion....37

4 InAs Quantum Dot Comb Lasers on Silicon Substrates by Wafer Bonding....39

4.1 Introduction....40

4.2 Experiment....41

4.3 Characterization and Discussion....44

4.4 Conclusion....46

5 Passive mode-locked InAs quantum dot lasers on silicon substrate by Pd-GaAs Wafer bonding....47

5.1 Introduction....48

5.2 Experiment....49

5.3 Characterization and Discussion....51

5.4 Conclusion....58

6 Characterizations of Optical Feedback Effects in InAs Quantum Dot Lasers Butt-Joint Coupled with Silicon Photonics Waveguides 60

6.1 Introduction 61

6.2 Experiments 62

6.2.1 InAs Quantum dot (QD) Laser 62

6.2.2 SOI silicon waveguide 63

6.2.3 Butt-joint coupling 63

6.3 Butt-joint couple characterization 65

6.4 Optical feedback by transfer matrix method 67

6.5 Conclusion 69

7 InAs Quantum Dot Lasers With Dry Etched Facet by Br-Ion Beam-Assisted Etching 70

7.1 Introduction 71

7.2 Br-IBAE Etching of $Al_x Ga_{1-x} As$ 72

7.3 Quantum dot lasers with dry-etched facets 73

7.4 Conclusion 77

8 Butt-joint heterogeneous integration platform by Pd-GaAs wafer bonding 79

8.1 Introduction 80

8.2 Butt-joint heterogeneous integration platform by Pd-GaAs wafer bonding 83

8.3 Detailed design and simulation of butt-joint heterogeneous integration.....87

8.4 Hybrid tunable InAs QD lasers butt-joint heterogeneously integrated on a Si substrate 90

8.5 Proof of concept demonstration of the hybrid tunable lasers 91

8.5.1 Design and simulation 91

8.5.2 Experiment.....94

8.5.3 Characterization and discussion 96

8.6 Conclusion.....99

9 Summary and future work 101

9.1 InAs QD broadband gain chip.....102

9.2 Hybrid QD Laser on Silicon by Pd-GaAs wafer bonding.....102

9.3 Preparation of InAs QD Laser integration to PICs.....103

9.4 Butt-joint heterogeneous integration platform by Pd-GaAs wafer bonding 104

9.5 Future work 105

10 Publications 108

11 Appendices 111

12 Reference.....116

List of Figures

Figure 1-1 40 years of microprocessor data from Intel.....1

Figure 1-2 Power density trend of CPUs. Courtesy of Intel. 2

Figure 1-3 Copper interconnects in a CPU. Courtesy of IBM.....3

Figure 1-4: The trend of transmission distance vs. device volume for optical interconnects. 4

Figure 1-5 Building blocks of silicon photonic systems.....6

Figure 1-6 Schematic structures and corresponding density of states of a) bulk; b) quantum well, c) quantum wire and d) quantum dot. 9

Figure 2-1. (a) AFM image of the InAs QDs with the average base diameter and height of 45 and 8 nm, respectively. (b) PL spectra of the InAs QDs capped with different strain-reducing layer thickness and combinations. 19

Figure 2-2(a) Power-dependent PL spectra of the ten stack InAs QD heterostructures before annealing, including four, three, and three stacks of InAs QDs with strain-reducing layer thickness of 0 nm, 1 nm $In_{0.2}Al_{0.8}As$, and 1 nm/2 nm $In_{0.2}Al_{0.8}As/In_{0.15}Ga_{0.75}As$, respectively. (b) Spectrum 3-dB bandwidth versus pumping power. 21

Figure 2-3(a) Power-dependent PL spectra of the ten stack InAs QD heterostructures after annealing at 750 °C for 30 s. (Inset) Comparison of PL spectra before (solid) and after annealing (dashed). (b) Spectrum 3-dB bandwidth (black square

symbols) and spectrum intensity dip (blue round symbols) versus pumping power after annealing at 750 °C for 30 s. 22

Figure 2-4 (a) Light–current (L–I) characteristics of a SLED with the diagram of device dimensions, i.e.,the cavity length and waveguide width of 1.5 mm and 9 _m, respectively; the superlinear L–I dependence is a signature characteristic of SLED devices. (Inset) Diagram of the titled waveguide design. (b) EL spectra of InAs QD SLEDs at the injection current levels from 50 mA to 100 mA, where the EL spectra exhibit a uniform broadening in the injection current from 50 mA to 100 mA.....23

Figure 3-1 Schematic of the InAs QD Laser diode heterostructure.....28

Figure 3-2(a) HR-TEM images of the InAs QDs; (b) I-V characteristics of the bonding structure with top contact and bottom contact method,respectively. The inset shows a schematic of the bonding structure. 31

Figure 3-3(a) Light current (L-I) characteristics of the bonded laser (solid line) and the unbonded laser (dashed line). The inset shows the electroluminescence (EL) spectrum of the bonded laser. Both the bonded and unbonded lasers have a cavity length and waveguide width of 1.5 mm and 5 μm, respectively. (b) Measured threshold current density of the bonded and unbonded (circled) lasers of different reciprocal cavity lengths. (c) emission spectra of the bonded and unbonded lasers below threshold ($0.9I_{th}$) 32

Figure 3-4 Heat transfer simulation thermal profile of bonded and unbonded lasers at temperature of (a) 0k and (b)373K. 34

Figure 3-5(a) Light-current (L-I) characteristics of bonded laser under the different operation temperature from 50˚C to 100˚C with the laser cavity length and waveguide width of 1.5 mm and 5 μm, respectively. (b) Natural logarithm of the threshold current versus stage temperature for the bonded laser with the same device in Figure 3-3a. 35

Figure 3-6 (a) High-speed laser characterization setup. (b)Eye diagram characterization of bonded InAs quantum dot lasers. (c) Small signal modulation characteristics of InAs bonded lasers. 37

Figure 4-1 Schematic of the InAs QD superluminescence light emitting diode heterostructures 42

Figure 4-2 HR-TEM images of 7 stacks layers of the InAs QDs. Inset: AFM images of QDs. 43

Figure 4-3(a) Light-current-voltage (L-I-V) characteristics of a SLED with the cavity and waveguide width of 1 mm and 50 μm, respectively; (b) EL spectra of InAs QD SLEDs at the injection current of 1400 A/cm^2, the emission spectrum has a linewidth of 20 nm and 30 nm at 3 dB and 10 dB, respectively. 44

Figure 4-4 Injection current vs. peak wavelength position, where the continuous blue-shift of peak emission indicates the quasi-continuous interband transition characteristics in QDs 45

Figure 5-1(a) Heterostructure schematic and (b) diagram of the InAs QD mode-locked laser diode on silicon. 50

Figure 5-2 (a) Magnified cross-section SEM image of the laser facet with a 70° tilted angle and (inset) unmagnified SEM image of the same region. (b) Top view SEM image and I-V characteristics (inset) of dry etched electrical isolation gap between the gain and saturable absorber sections.....51

Figure 5-3 Light current (L-I) characteristics of the bonded mode-locked laser under reverse bias voltages of 0V and -4V with forward and backward sweep current. Upper right inset: close-in L-I around threshold current. Lower left inset: electroluminescence (EL) of bonded mode-locked laser with a reverse bias voltage of 0V with injection current of 150 mA.....52

Figure 5-4 (a) Optical and (b) RF spectra evolutions with injection current from 100 mA to 240 mA at 0V bias. (c) Optical and (d) RF spectra evolutions with injection current from 100 mA to 240 mA at -7V bias. Inset: RF spectra at optimized injection (I_g=125 mA) and at bifurcated spectrum operation (I_g=215 mA). The RF signal degrades significantly at higher injection currents where the optical spectrum splits. 54

Figure 5-5 (a) RF spectrum and pulse train (inset); (b) optical spectrum and temporal pulse width (inset) of bonded mode-locked QD laser under the optimized bias condition of I_g=124 mA and V_a=-7 V, respectively. 55

Figure 5-6 Schematic drawing of three configurations for passive mode-locked laser: a) two section mode-locked laser, b) single cavity mode-locked laser, and c) colliding pulse mode-locked laser. 56

Figure 5-7 a)RF spectrum of colliding pulse QD mode-locked laser and b) RF spectrum of a single cavity mode locked laser bonded on Si. 58

Figure 6-1 Schematics and micrograph image (inset) of the Si waveguide and QD laser butt joint couple experimental setup 64

Figure 6-2: (a) L-I characteristics of butt-joint coupled (solid line) and uncoupled (dashed line) QD lasers, where a reduced threshold current from 455 A/cm2 to 435 A/cm2 compared to uncoupled QD lasers is observed; (b) Laser output power vs. time characteristics of uncoupled (red) and coupled (black) lasers, where a laser output power self-pulsing is measured from the coupled QD lasers.....66

Figure 6-3 The schematic model of optical feedback from the silicon photonics interface and equivalent cavity model, which considered all the reflections on butt joint, coupled side as one effective reflectivity. 67

Figure 6-4 (a) Reciprocal differential efficiency η^{-1} vs. cavity length L; (b) Laser threshold current density J_{th} and vs. Reciprocal of cavity length 69

Figure 7-1 Etching rate vs. substrate temperature and Bromine pressure. 72

Figure 7-2 Light-current (L-I) characteristics of a QD laser with the cavity length and waveguide width of 1.2 mm and 30 μm, respectively, and dry-etched/as-

cleaved facets (solid) and as-cleaved/as-cleaved facets (dash); inset: electroluminescent spectrum of QD laser. 74

Figure 7-3(a) Plot of threshold current density (J_{th}) vs. reciprocal cavity length (1/L), and the mirror reflectivity R of the dry-etched fact of 0.28 is obtained; (b) Temperature dependence of threshold current density, J_{th}, (solid) and slope efficiency, η_d, (dash) of a typical QD laser with cleaved/dry-etched facets under pulsed bias operation. 77

Figure 8-1 Three methods to integrate laser source to a photonic integrated circuit on silicon to form a hybrid laser: (a) fiber-to-chip integration, (b) flip-chip bonding, and (c) hybrid monolithic integration.[6] 81

Figure 8-2 Flip-chip bonding laser source sehmatics of a)back side alignment and b) self-aligned bump bonding.[4, 5].....82

Figure 8-3 Shematic of a) a silicon evanescent laser and b) a adiabatic III-V/Si laser integration platform.[1-3] 83

Figure 8-4 Fabrication flow of butt-joint heterogeneous integration platform by Pd-GaAs wafer bonding 84

Figure 8-5 Butt-joint heterogeneous integration platform by Pd-GaAs wafer bonding 86

Figure 8-6 Schematic illustration of laser diode chip integrated on Si waveguide with the spot-size converter.[161] 88

Figure 8-7 Top: Schematic of tunable QD lasers monolithically integrated on silicon by Pd-GaAs wafer bonding platform. Bottom right: the broad band QD-SLD optical spectrum. Bottom left: simulation reflection spectrum of traditional ring resonator and DBR. 91

Figure 8-8 3D FDTD simulation results: (a) power distribution and (b) wavelength dependent response of directional coupler for TE mode; (c) power distribution and (d) wavelength dependent response of 1×2 multi-mode interferometer (MMI) for TE mode 92

Figure 8-9 Simulation results of HR and AR SOA facet coating 93

Figure 8-10 Layout designs of QD gain chip (SOA and LD) and silicon nitride passive devices (straight waveguide and ring reflectors). 94

Figure 8-11 Schematic diagram of the experimental setup to characterize the hybrid tunable laser Si_3N_4 PICs. Inset is the optical microscope picture of a Si_3N_4 ring reflector PIC. 95

Figure 8-12 L-I characterization of external-cavity laser. Inset shows the infrared picture of silicon nitride ring in resonance.....96

Figure 8-13 Optical spectrum of the external cavity laser with the injection currents at a) 50mA, 53mA, b) 210mA and c) 60mA (inset: zoom in optical spectrum at 60mA injection current). 97

Figure 8-14 (a) Laser tuning optical spectra with temperatures ranging from 22.8 to 27.5 ˚C. (b) Linear fitting of the thermal tuning coefficient of Si_3N_4 feedback ring resonator. Inset: picture of external laser set up. 98

Figure 8-15 Optical spectrum of external laser with temperature tuned from 27.8 to 28.2˚C 99

Figure 9-1 OTDM takes in short optical pulses operating at 5Gb/s (left) and multiplexes them to 5N Gbit/s (right) by splitting the original pulses into N separate channels and then recombining them after they go through bit-rate determined delays ΔL.[173].....107

List of Tables

Table 8-1 Comparisons of different integration approaches.....86

Table 8-2 Specification of Si vs. SiN waveguide platform 89

Table of Acronyms

AC.....Alternating Current

AFM .....Atomic Force Microscope

AMR .....Adiabatic Micro-Ring

AR .....Antireflection Coating

BCB .....Benzocyclobutene

CMOS .....Complementary Metal-Oxide-Semiconductor

CW .....Continuum Wave

CWDM .....Coarse Wavelength Division Multiplexing

DBR .....Distributed Bragg Reflector

DC.....Direct Current

DFB.....Distributed Feedback Bragg

DOS.....Density of State

DWDM .....Dense Wavelength Division Multiplexing

EL.....Electroluminescence

FIB .....Focused Ion Beam

FP .....Fabry-Perot

FSR .....Free Spectral Range

FTTH.....Fiber To The Home

FWHM.....Full Width at Half Maximum

GR.....Growth Interruption

GRIN.....Graded Index/Gradient-Index

HR.....High reflection

IBAE .....Ion Beam-Assisted Etching

IC.....Integrated Circuit

ICP-RIE.....Coupled Plasma Reactive-ion Etching

IR.....Infrared

MBE.....Molecular Beam Epitaxy

ML.....Mode-locked

MOCVD .....Metal-Organic Chemical Vapour Deposition NIR

OCT.....Optical Coherence Tomography

OSA.....Optical Spectrum Analyzer

OTDM.....Optical Time-Division Multiplxing

PECVD .....Plasma-enhanced Chemical Vapor Deposition

PIC .....Photonic Integrated Circuit

PL.....Photoluminescence

QD .....Quantum Dot

QW .....Quantum Well

RC .....Resistive-Capacitive

RF.....Radio Frequency

RSOA.....Reflective Semiconductor Optical Amplifier

RT .....Room Temperature

RTA.....Rapid Thermal Annealing

RWG .....Ridge Waveguide

SAG.....Selective Area Growth

SCH.....Separate Confinement Heterostructure

SEM .....Scanning Electron Microscopy

SLD.....Superluminescent Diode

SLED .....Superluminescent light diode

SiP.....Silicon photonic

SiPIC.....Silicon photonics integrated circuit

SOA .....Semiconductor Optical Amplifier

SOI .....Silicon on Insulator

SSC .....Spot Size Converter

TEC.....Temperature Electric Controller

TEM.....Transmission Electron Microscopy

TMM .....Transfer Matrix Method

UHNA .....Ultra-High Numerical Aperture

WDM .....Wavelength-Division Multiplexing

1 INTRODUCTION

1.1 The challenge of Moore's Law

We are now living in what is known as the 'information age' which evolved from the industrial age. One of the most significant inventions of this era was that of the transistor by Bell Laboratories in 1947; an innovation that opened the door to the digital world. It was this innovation that led to the rapid development of semiconductor technologies over the half-century that followed. The trend in development is often described by the number of transistors in a microprocessor via Moore's law, "The complexity for minimum component costs has increased at a rate of roughly a factor of two per year".[7] This law was later simplified to be the number of components per integrated circuit doubling every 18-24 months.

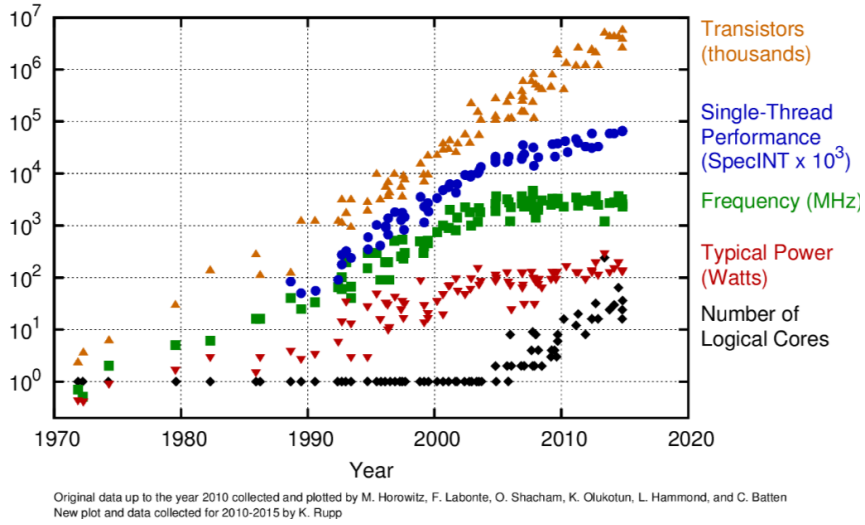

Figure 1-1 40 years of microprocessor data from Intel

While Moore's law is still valid today ,as shown in Figure 1-1, other performance metrics such as clock frequency, power consumption, and single thread performance have seen minimal change since 2005. To assist Moore's Law, the electronics industry has moved to larger wafers to minimize processing costs, pushed to smaller technology nodes, and increased the number logical cores per processor. However, there are some serious problems that need to be solved in order to continue following the trend of Moore's Law.

The first bottleneck is with power dissipation. The power dissipation of a microprocessor is proportional to its clock frequency and device density of each core. As shown in Figure 1-2, the power density of a CPU has reached levels comparable to those of a nuclear reactor. This is the primary reason why the clock frequency of CPUs has been unchanged for so many years. In order to continue seeing performace gains, additional logical cores have been implemented to operate in parallel. As a result, there is a growing need for an efficient inter\intra chip interconnects to wire up the increasing numbers of cores within microprocessors.

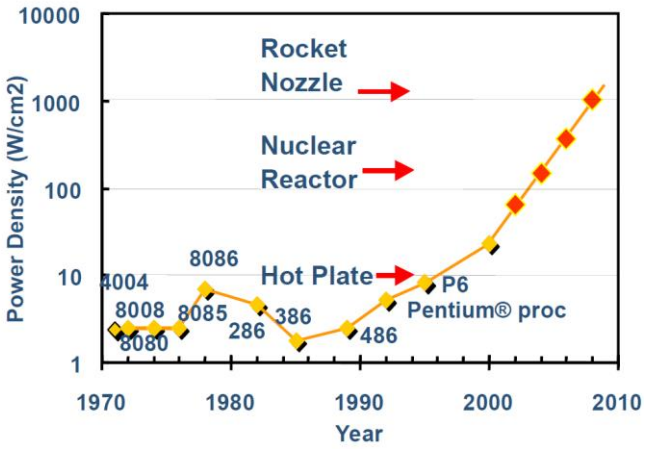

Figure 1-2 Power density trend of CPUs. Courtesy of Intel.

The second major problem is the limited space for electrical interconnects that has resulted from the dramatic increase in the number of transistors. Figure 2-3 shows the copper wire

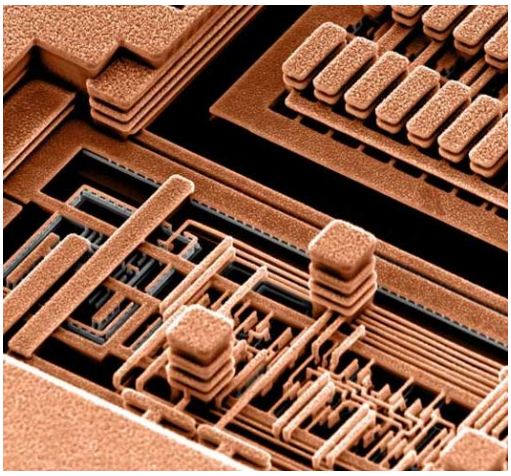

Figure 1-3 Copper interconnects in a CPU. Courtesy of IBM.

interconnects inside a microprocessor from IBM. As the dimensions of these electrical interconnects are decreased, both resistance (loss) and RC signal delay (bandwidth) increase, limiting the performance gain. Also, as can be seen in Figure 1-3, there is almost no room to add more wires in current processors. As a result, an interconnect solution having higher bandwidth is needed to overcome this limitation.

Another area of high demand for low power consumption interconnects is in data centers. The rapid development of the internet and internet of things (IOTs) generates a huge amount of data to the cloud which is the so-called data center to store and process all of the data. However, traditional data centers are still using electrical interconnects which consume 15%-30% more power when compared to optical interconnects.[8] Among these data centers, a large number of them have been built in the northern parts of the country to take advantage of the cold weather. It is also argued that the annual costs of power-

supplying and cooling high-performance switches in data centers have reached the annual cost of purchasing new ones from the business point of view. [9]

1.2 Optical Interconnects

As we discussed above, either in chip level or in a large scale data center, a high speed, large bandwidth, low power consumption interconnect solution is required to maintain the fast development of the information age. Light, as a transfer medium, perfectly meets all of the criteria due its high speed, large bandwidth and ultra-low transmission loss. As a result, the so-called optical interconnect is defined by using light to transfer data. In fact, we have used optical interconnects in the form of optical fiber for long-haul networks since early 1980's. Figure 1-4 shows the current development of optical

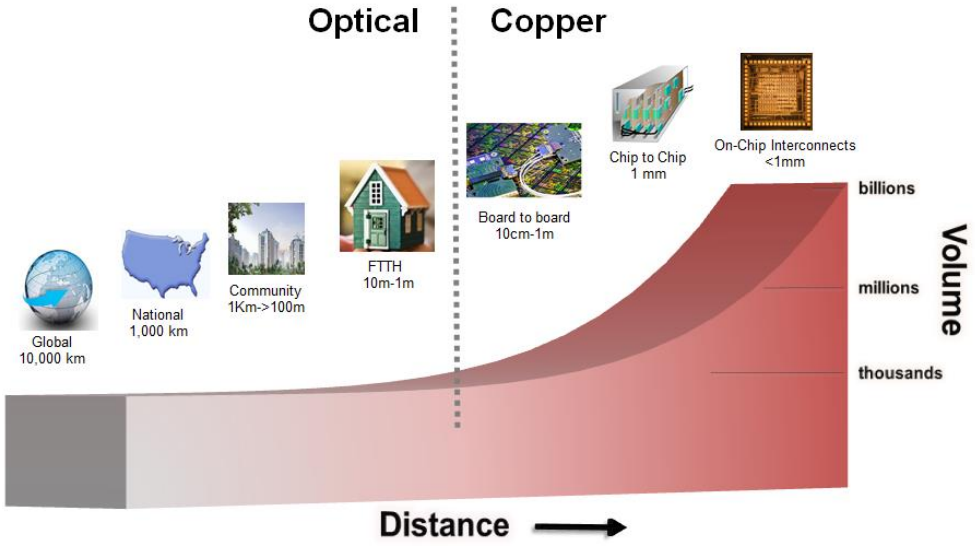

Figure 1-4: The trend of transmission distance vs. device volume for optical interconnects.

interconnects. As one of the major inventions of the 20th century, low loss optical fiber has successfully taken over the electrical interconnection in long-haul telecommunication

down to fiber-to-the-home (FTTH). In order to solve the problems discussed in the first section, the electrical interconnects needs to be further replaced from board-to-board (as in data centers) to chip-to-chip scale, and eventuallyon-chip optical interconnection as in photonic integrated circuits (PICs). However, as shown in Figure 1-4, the volume of devices dramatically increased as you move to a smaller transition distance which will also simultaneously increase the cost and complexity of the optical interconnect system. The challenge we are facing right now is to find a cost-effective solution to build up a highly integrated photonic circuit.

1.3 Silicon Photonics

The traditional complementary metal oxide semiconductor (CMOS) infrastructure has been built up up with silicon as the primary material for over 40 years, leading to a mature and cost effective solution for electronic integrated circuits. Along with the maturity of the processing techniques, silicon is transparent at the standard telecom bands making it an ideal material system for photonics. The base material for silicon photonics is not simply silicon wafers but high quality silicon-on-insulator wafers which can provide strong optical confinement from huge index differences between Si (n=3.45) and SiO_2 (n=1.45). By using SOI as a platform, as shown in Figure 1-5, individual silicon photonic devices are demonstrated. At the beginning, the low loss waveguide [10] and passive components such as Mach-Zehnder interferometer and Multi/Demultiplexer were developed in the 1990's

[11, 12]. Later on, active devices were also demonstrated, such as high-speed modulators[13, 14] and detectors [15].

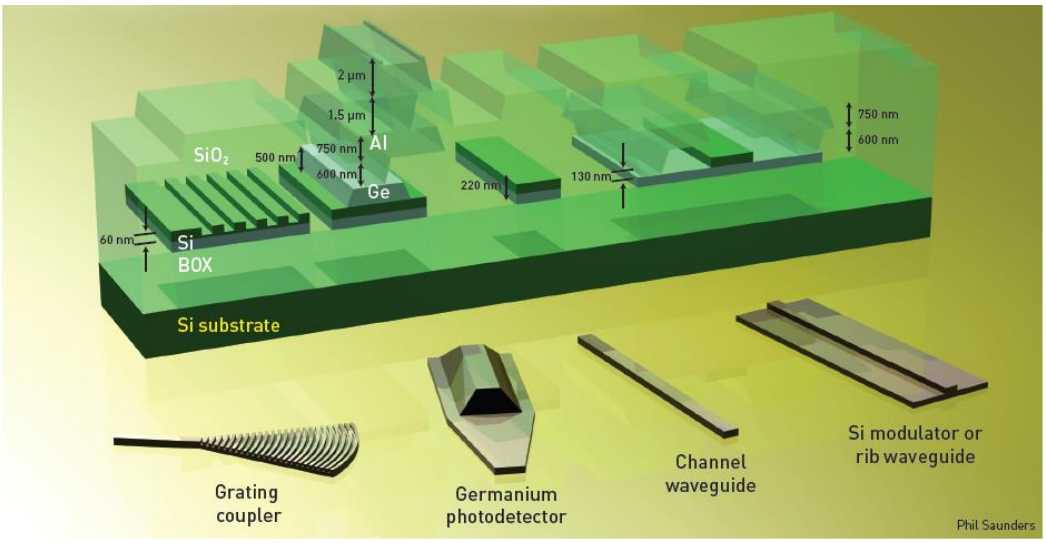

Figure 1-5 Building blocks of silicon photonic systems.

1.4 Laser Integration with Silicon Photonics

As one key component for integration, the laser source needs to be considered.[16] Due to the silicon's indirect bandgap, the injection current will primarily generate phonons (heat) instead of photons. By using unique nanotechnologies such as porous Si[17, 18], Si nanocrystals[19], SOI superlattice[20] and photonic crystal-like nanopatterns[21], people have tried to break the crystal-symmetry to localize phonon and get quantum confinement of the excitons in a nanometer scale crystalline structure[21]. However, it is still difficult to achieve room temperature continuous-wave laser operation. While silicon Raman laser have also been investigated, devices that operate at room temperature are optically pumped and required a complicated process for decreasing waveguide loss (free carrier absorption as well as two photon absorption).[22]

A breakthrough came in 2006 when the Optoelectronics Research Group from UCSB demonstrated a hybrid laser which used a III-V quantum well structure as a gain material and evanescent coupling to a Si waveguide to achieve an electrically pump state of the art laser working at telecom wavelengths. [2] Currently, this hybrid laser innovation is commercially available in Intel's 100G silicon photonic transceivers. Based on this evanescently coupled hybrid laser, an adiabatic laser was later developed with enhanced laser efficiency by coupling light into silicon waveguide only at two end edges of the gain material.[23] However, these lasers used either oxide or benzocyclobutene (BCB) as bonding layers resulting in poor heat dissipation. Also, the laser coupling efficiency to the silicon waveguide still has room for improvement when compared to the fiber coupled systems. In recent years, researchers made a lot of progress towards direct growth of III\V materials on silicon substrates. In order to eliminate the large lattice mismatch between the III\V and silicon, several technologies are applied such as using a tilted off-cut substrate, submicron trenches patterned into the substrate, and growing thicker superlattice buffer to decrease the dislocation density at the interface between silicon and III\V materials. [24-26] Also, quantum dot (QD) lasers are used to grow through these optimization technologies because QD lasers have more tolerance with dislocations compared to QW lasers. The downside of direct growth lasers for photonic integration is that lasers need selective area growth (SAG) on standard CMOS silicon substrates which is still under development.

In this proposal, we are trying to solve these above problems in three ways. First, we use metal mediated bonding technology to increase heat dissipation. Second, instead of

using the quantum well structure as the gain material, we grow QDs for the gain medium which is a good candidate for photonic integration applications as we will discuss in following sections. At the end of this thesis, a heterogeneous butt-coupled laser is proposed based on the Pd-GaAs wafer bonding technology we investigated through the thesis.

1.5 Quantum Dot Lasers

The history of semiconductor lasers started with a proposal based on p-n junction bulk material and experimentally realized in 1961.[27] However, both optical and quantum confinement were inefficient in the bulk material. Later on, Alferov and Herbert demonstrated the heterostructure laser by inserting a lower bandgap material between higher bandgap materials which enhanced the laser performance by improving both the optical confinement as well as the quantum efficiency. [28] During the 1960s, molecular beam epitaxy (MBE) was developed which enabled semiconductor heterostructures to be grown with high crystal quality. By using this MBE technology, the laser structure could be designed and grown with decreased dimension (on the order of the de Broglie wavelength of an electron), which resulted in higher order confinement of electrons. As shown in Figure 1-6, when the semiconductor structure is confined in 1-D, the so-called quantum well structure, the corresponding density of states (DOS) starts showing discontinuity. As the electrons are confined in 3-D, the energy-momentum (E-k) relationship shows a delta-function-like DOS, which means the charge carriers can only occupy a restricted set of energy levels similar to electrons in an atom. This 3-D quantum confinement structure can be experimentally achieved by growing quantum dot structure with molecular beam epitaxy (MBE). Using this quantum dot structure as the active region

of a laser makes both population inversion and transparency easier to achieve. This means that, in theory, quantum dot lasers can have lower threshold current density when compared to quantum well lasers. In addition, the 3-D quantum confinement structure also leads QD lasers having a temperature insensitive threshold current.

The first theoretical prediction of QD (called 3-D QW at that time) laser was by Arakawa in 1982 in which both the enhanced quantum confinement and temperature insensitive properties were discussed.[29] Later on, the first edge-emitting current injection

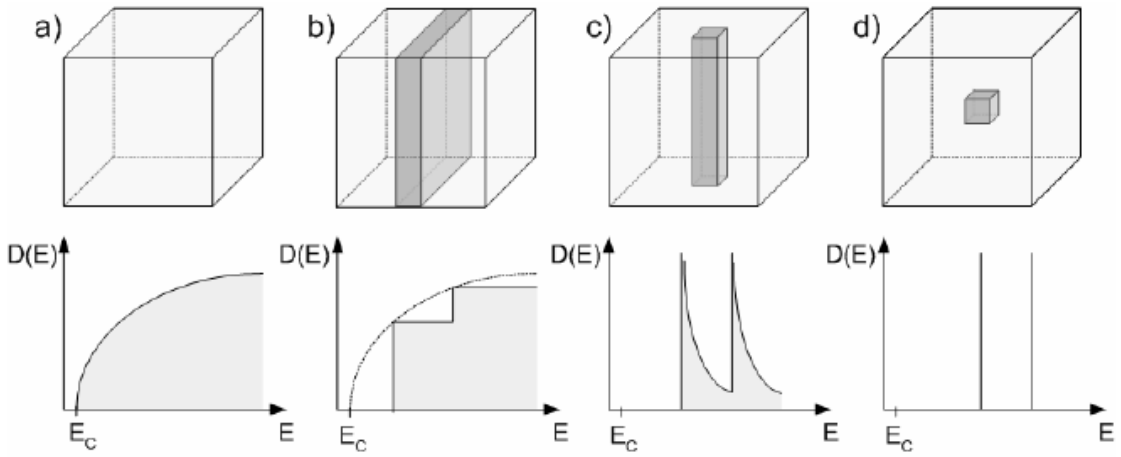

Figure 1-6 Schematic structures and corresponding density of states of a) bulk; b) quantum well, c) quantum wire and d) quantum dot.

QD lasers were experimentally achieved by InAs QDs embedded in an AlGaAs/GaAs GRIN-SCH structure in 1994.[30] It wasn't until 1999 that the threshold of a QD laser was demonstrated to be lower than QW lasers [31]. In 2004, using p-doped quantum dots, Fathpour et. al achieved temperature insensitive performance ($T0=\infty$) for laser operation from 5 to 75°C. [32]

The high performance QD lasers can be grown by either Molecular Beam Epitaxy (MBE) or Metal Organic Chemical Vapor Deposition (MOCVD) with a method known as

Stranski-Krastanov (S-K) growth.[33] In this growth technique, the film is initially grown layer by layer to form a strained wetting layer. After the wetting layer reaches a critical thickness, the strain inside film tends to relax and form three-dimensional islands which are the so-called quantum dots. Specifically, the InAs film lattice constant is 6.06 Å which has 7% misfit from GaAs film (5.64 Å). In order to achieve a high performance semiconductor laser, a high modal gain is needed from the QDs. In other words, the QDs in the active region are required to have high density as well as high uniformity. Also, the QDs need to be grown in stacks which enable even higher modal gain without increasing the internal optical mode loss.[34]

To achieve high density and uniform QDs, several technologies were used in our growth process. First, the seeds layer of QDs was grown with a fast growth rate for ~2ML in order to get a high density of dots as well as eliminate the formation of coalescent QDs. After that, the growth interruption (GR) method was used to let indium atoms migrate to the QD seed layer and form more uniform and larger QDs. After that, another 0.6ML of InAs was deposited and then capped with a 5 nm $In_{0.5}Ga_{0.85}As$ strain reducing layer to achieve emission at 1300nm. The V\III ratio of InAs QDs was also optimized since it related to the size and uniformity of the QDs. A higher ratio may cause coalescent dots while a relatively low ratio may let indium atom migrate better during growth, resulting in a more uniform distribution of dots. To characterize the QDs film quality, atomic force microscopy and photoluminescence were used to measure the density and uniformity of the dots, respectively. The optimum growth conditions were achieved with a V\III ratio of

15, interval time of 10 sec and growth rate of 0.1ML/s. As a result, the state of the art 7×10^{10} cm^{-2} dot density was achieved.

1.6 Characterization of the semiconductor laser

For semiconductor lasers, the light-current (L-I) characterization is the most commonly used method to test DC properties. Here, we introduce different characteristic parameters by fitting the L-I curves of different cavity lengths or temperatures.

1.6.1 Threshold current J_{th} and transparent current density J_{tr} ($J_{th,\infty}$)

The gain-current for a semiconductor laser can be described by the functions (Mcllroy et al., 1985; Coldren and Corzine, 1995, p. 173):

$$G_{peak} = G_{tr}\left(ln\frac{J}{J_{tr}} + 1\right) \text{..... (2.1)}$$

When the injection current reaches threshold:

$$G_{th} = \alpha_i + \frac{1}{2L}\ln\left(\frac{1}{R_1R_2}\right) = G_0\ln\left(\frac{J}{J_{tr}}\right) + G_0 \text{ ..... (2.2)}$$

Then the transparent current can be extracted by fitting the curve of (1/L) v.s. ln(J_{th}). The intercept of the fit describes the transparent current which gets rid of the mirror loss impact while the slope of the curve is proportional to the mirror loss.

1.6.2 Differential quantum efficiency η_d, internal quantum efficiency η_i and internal loss α_i

The differential quantum efficiency is defined by:

$$\eta_d = \frac{2\lambda(um)}{1.24}\frac{dP_{out}}{dI} = \eta_i\left(\frac{1}{1+\frac{\alpha_i}{\alpha_m}}\right) \text{ ……. (2.3)}$$

Where mirror loss $\alpha_m = \frac{1}{L} ln \frac{1}{R1R2}$, R1 and R2 are the reflectivity of front and back facet of the laser, respectively.

Then we have:

$$\eta_d{}^{-1} = \eta_i{}^{-1}(1 + \frac{\alpha_i L}{\ln(\frac{1}{R1R2})}) \text{ ……. (2.4)}$$

By fitting the curve of cavity length v.s. inverse differential quantum efficiency, the internal loss and internal quantum efficiency can be extracted.

1.6.3 Temperature dependence of threshold current

One drawback of semiconductor lasers is the fact that their threshold current is influenced by operation temperature. However, quantum dots devices have less temperature sensitivity due to the delta function like DOS. The characteristic of temperature dependency can be defined by a parameter T_0, J_0 is the threshold current density extrapolated to T=0K.

$$J_{th} = J_0 \exp\left(\frac{T}{T_0}\right) \text{……. (2.5)}$$

$$or\ ln\, J_{th} = \ln J_0 + \frac{T}{T_0} \text{ ……. (2.6)}$$

Thus, the characteristic temperature can be fitted by temperature dependence L-V characterization. The lower number of T_0 indicates a lager temperature dependence. For quantum dots lasers, the characteristic temperature has been demonstrated as infinite at

room temperature which shows the good potential to use QD lasers as a thermally insensitive light source.

1.7 Dissertation overview

This dissertation focuses on the development of high performance quantum dot hybrid lasers integrated with silicon photonics. Chapter 2 investigated the quantum dot material growth and a broadband InAs quantum dot gain chip was demonstrated. Chapter 3 describes the Pd-GaAs wafer bonding technology and the realization of electrically pumped continuous wave operation ridge waveguide (RWG) InAs quantum dot lasers bonded to Si substrates. Both DC and RF characteristics of these lasers were measured. Chapter 4 presents the comb laser source which was the material developed in Chapter 2 bonded to a Si substrate. Chapter 5 demonstrates a passively mode-locked InAs quantum dot laser bonded to silicon. Fourier transform limited pulses were successfully generated and two other passively mode-locked configurations: single cavity mode-locking and colliding pulse mode-locking are also presented. Chapter 6 presents the butt-joint integration platform by using a QD SOA coupled to a Si SOI waveguide chip. An AR coating was applied on the SOA facet to stabilize the laser power from the silicon waveguide. Chapter 7 investigates a dry etched facet approach which was fabricated by bromine ion beam-assisted etching (IBAE). The dry-etched facet results show the reasonable reflectivity which provided an approach to define the laser facet for monolithic integration without a cleaving step. Chapter 8 presents the design of the butt-joint heterogeneous integration platform by using Pd-GaAs wafer bonding. A proof of concept hybrid Si_3N_4 tunable laser was demonstrated by an externally coupled SOA to the Si_3N_4

photonic integrated chip. Chapter 9 concludes this dissertation with a discussion of the future development based on the InAs quantum dots wafer bonding technology and butt-joint heterogenous integration platform.

2 DIP-FREE BROADBAND INAS QUANTUM DOT SUPERLUMINESCENCE LIGHT EMITTING DIODES

Broadband InAs quantum dot (QD) super-luminescence light emitting diodes (SLEDs) have been grown by molecular beam epitaxy (MBE) system, fabricated and characterized. In order to eliminate the spectrum dip between the ground and excited states and achieve the broadband and uniform emission, the InAs quantum dots active regions with different strain reducing layers (SRLs) have been utilized and mixed in the design of the QD SLED active regions. In addition, a post-growth annealing process is employed to further smoothen the emission spectra. Room temperature photoluminescence measurements were used to characterize the emission spectra of the QDs. Finally, the electroluminescence spectra of the QD SLEDs were characterized under the continuous-wave (c-w) operation. At injection current level of 100 mA, a broad and uniform spectrum with a linewidth of 100 nm and 218 nm at 3 dB and 10 dB, respectively, was obtained and no significant spectrum dip is observed under the injection currents ranging from 50 μA to 100 mA.

2.1 Introduction

It has drawn great interests recently that the development of broadband light source and superluminescence light emitting diodes (SLEDs) in the near infrared (NIR) wavelength range in the applications of optical coherence tomography (OCT) biomedical imaging systems.[35-46] Due to the unique three dimensional confinement and the Stranski-Krastanov (S-K) self-assemble growth mechanism, the self-assembled InAs quantum dots (QDs) have been largely investigated as the active region in the broadband SLED devices and are considered to be beneficial to the broad gain applications.[47-52] Despite of be a promising candidate, there still remains challenges to achieve high performance QD SLEDs.[53-58] In particular, in order to achieve broadband and high output power, the QD SLEDs have to be operated at high injection levels, where the gain spectra usually exhibit a dip between the ground state and excited state due to the finite number of density-of-states in the QD heterostructures. In this respect, several techniques have been developed, such as post-growth annealing and mixed quantum dot structures, to alleviate the spectrum dip in QD broadband sources. However, in the mixed QD structures, the excited state emission of the QDs with longer ground state emission wavelengths will usually be interference with the ground state emission with other dots, and due to the complicated carrier dynamics in the QDs, it is very difficult to control the carrier distribution between the ground and excited states. This often results in non-uniform emission spectra across different injection currents in the QD broadband SLEDs,[59] which can be potential detrimental to their OCT applications.[60, 61] As a result, it is desirable to design the QD broadband structures without mixing the excited state

emissions. It is argued that, by using the large bandgap InAlAs strain reducing layers (SRLs), the QDs emission will exhibit enlarged ground and excited state separation,[62, 63] which can potentially accommodate ground state emission from other QDs and enable broadband mixed QDs with separated ground and excited state emissions. In this section, we demonstrated the growth, and characterization of InAs QD broadband heterostructures achieved by mixing QDs with different InAlAs SRLs, and post-growth annealing technique is also studied to further smoothen the emission spectra. Finlay, broadband QD SLEDs were fabricated and characterized to show broad and uniform emission spectra.

2.2 Experiment

The InAs quantum dot (QD) heterostructures were grown on (001) GaAs substrates in a Veeco GEN II molecular beam epitaxy (MBE) system. In the calibration experiments, one layer of InAs QD active region consisting of 2.6 monolayer (ML) of InAs QDs was grown at 500 ˚C at the growth rate of 0.1 ML/s, and the QDs were capped with $In_{0.2}Al_{0.8}As$ and $In_{0.2}Al_{0.8}As$ /$In_{0.15}Ga_{0.75}As$ SRLs with different thickness. Following the calibration runs, the broadband QD heterostructures with 10 stacks of InAs QD layers were investigated, where the 10-stack QD layers were divided into 3 groups, containing 4, 3, and 3 stacks of InAs QDs with the strain reducing layer of 0 nm, 1 nm $In_{0.2}Al_{0.8}As$ and 1nm/2nm nm $In_{0.2}Al_{0.8}As$ /$In_{0.15}Ga_{0.85}As$, respectively. The total number of each type QD stacks was chosen to compensate the intensity difference. P-type modulation doping of the QDs in each layer is carried out with beryllium at the doping concentration of $1x10^{18}$ cm^{-3} as well, as it has been reported that the p-type doped QDs exhibit broader gain spectrum due to the many body effect of the charged dopant ions. [64] In addition, in order to achieve

a uniform and flat gain spectrum, the as-grown QDs were also annealed in a rapid thermal annealing (RTA) process at 750 ˚C for 30 sec. The annealing process can effectively enhance the inter-diffusion between the InAs QD and surrounding capping layers and further increase the emission linewidth. This annealing method has been reported by several groups to obtain broadband InAs QD based gain chip devices.[65, 66]

In order to characterize the gain property of the InAs QD active regions, InAs QD SLED device heterostructures were epitaxially grown, where the 10 stack mixed QD structures were grown between the $Al_{0.4}Ga_{0.6}As$ cladding layers. The devices were fabricated by standard photolithography, dry etching, contact metallization, and cleaving techniques, where the ridge waveguide width and the cavity length were varied from 5 to 9 μm and 1000 – 2000 μm, respectively. All of the measurements reported here were performed with the SLED waveguide facets un-coated (as-cleaved). To prevent the SLED devices from lasing and the ridge waveguide is designed to be 7˚ tilted from the facets at both ends to reduce the reflection at the facets and enhance the facet mirror loss.

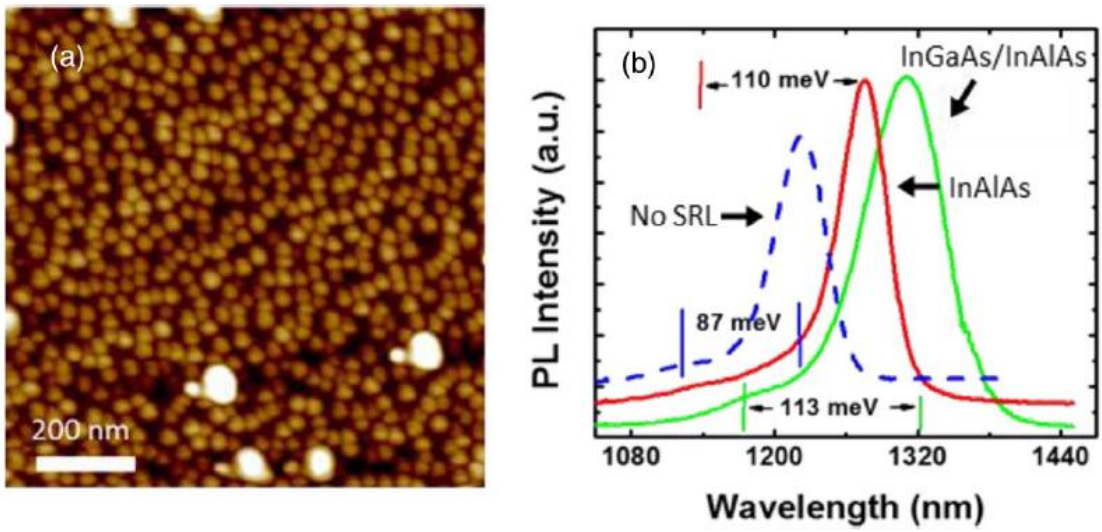

Figure 2-1. (a) AFM image of the InAs QDs with the average base diameter and height of 45 and 8 nm, respectively. (b) PL spectra of the InAs QDs capped with different strain-reducing layer thickness and combinations.

The structural and optical properties of the InAs QDs are investigated by atomic force microscope (AFM) and photoluminescence (PL) measurements, respectively. As shown in Figure 2-1a, the InAs QDs have an areal density of ~7 x 10^{10} cm^{-2} and average size and height of 45 nm and 8 nm, respectively. Figure 2-1b illustrate the room temperature PL characteristics of the InAs QDs with different strain reducing layer thickness and combinations. It is found that the, by changing the strain reducing layer thickness, the ground state emission can be effectively tuned in a range from 1230 to 1310 nm and, more importantly, with the 2 nm InAlAs strain reducing layer, the QD exhibit a ground state and excited state separation of 113meV. This is at least 20 meV larger than ground and excited state energy separation of InAs QDs with InGaAs SRLs.[67] As a result, it is possible to insert the other ground state emission in the final mixed spectra without interfering with the excited state emissions. It is worthy noting that, due to the

increased dot density, the QDs with SRLs usually exhibit stronger PL emission intensity compared to the QDs without SRLs.

2.3 Characterization and Discussion

Furthermore, Figure 2-2a illustrates the power dependent PL spectra of the 10 stack InAs QDs heterostructures including 4, 3 and 3 stack of InAs QDs with strain reducing layer thickness of 0 nm, 1 nm $In_{0.2}Al_{0.8}As$ and 1nm/2nm nm $In_{0.2}Al_{0.8}As$ /$In_{0.15}Ga_{0.75}As$, respectively. Two distinguish emission peaks at 1235 nm and 1142 nm are observed in the emission spectrum, where the broad Gaussian emission at 1235 nm is from the combination of the ground state emission of the three different type of QDs and the emission at 1142 nm is the emission of the excited state of the QDs with the 1nm/2nm nm $In_{0.2}Al_{0.8}As$ /$In_{0.15}Ga_{0.85}As$ SRLs. The excited state emissions from other QDs with shorter ground state emission wavelength is not seen in this measurement due to the limited pumping power. The square and diamond symbols in Figure2-2b show the relation of the PL intensity and 3 dB bandwidth vs. pumping power. It is found that, by using the InAlAs SRLs in the QDs, the ground and excited state emission of the QDs are clearly separated in the mixed QD structures and the 3 dB bandwidth of 197 nm from the ground state emissions is successfully achieved at the pump power of 50 mW.

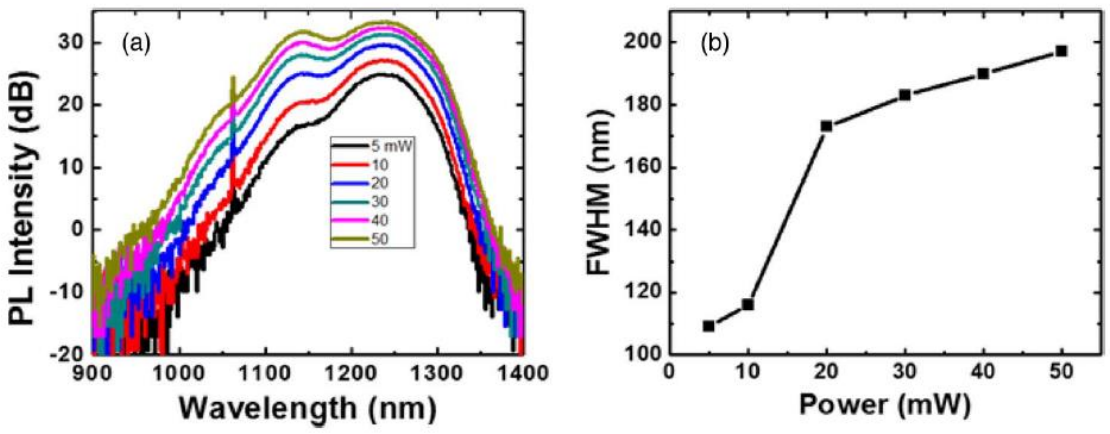

Figure 2-2(a) Power-dependent PL spectra of the ten stack InAs QD heterostructures before annealing, including four, three, and three stacks of InAs QDs with strain-reducing layer thickness of 0 nm, 1 nm $In_{0.2}Al_{0.8}As$, and 1 nm/2 nm $In_{0.2}Al_{0.8}As/In_{0.15}Ga_{0.75}As$, respectively. (b) Spectrum 3-dB bandwidth versus pumping power.

Finally, in order to further alleviate the gap between the ground and excited states, post-growth annealing process was performed. Figure 2-3 illustrates the power dependent PL spectra of the 10-stack QD samples after the annealing process, it is found that both the ground and excited state emissions are broadened due to the enhanced intermixing and the spectrum dip is reduced, where the 3dB bandwidth of 205 nm is achieved at the 50 mW pumping power by combining the ground and excited state emissions. Finally, for comparison, the dash curve in Fig. 3 shows the PL spectrum of the 10 stack mixed QDs after annealing. With our optimized annealing process, relative small PL intensity degradation in the post-growth annealing is obtained. Figure 2-3(b) shows the evolution of 3 dB bandwidth (black square symbols) and spectrum intensity dip (blue round symbols) vs. pumping power, where the 3 dB bandwidth of 205 nm is achieved at the 50 mW

pumping power by combining the ground and excited state emissions and a minimum spectrum dip ~0.6 dB is obtained as well.

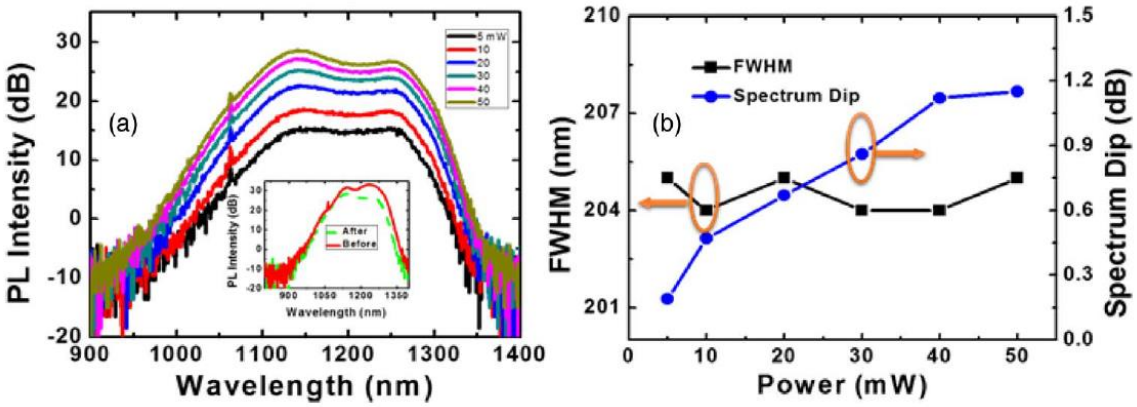

Figure 2-3(a) Power-dependent PL spectra of the ten stack InAs QD heterostructures after annealing at 750 °C for 30 s. (Inset) Comparison of PL spectra before (solid) and after annealing (dashed). (b) Spectrum 3-dB bandwidth (black square symbols) and spectrum intensity dip (blue round symbols) versus pumping power after annealing at 750 °C for 30 s.

The electrical characteristics of the SLED devices are measured with a customized probe station, where the samples were loaded with p-side up on a thermoelectric cooler (TEC) stage and device temperature was maintained at 10 ˚C during the measurements. Figure 2-4a shows the light-current-voltage (L-I) characteristics of a SLED with the cavity length and waveguide width of 1.5 mm and 9 μm, respectively. The ridge waveguide of the SLED was 7˚ tilted to the horizontal edges as the diagram as illustrated in the inset of Figure 2-4a. Figure 2-4b illustrates the electroluminescence (EL) spectra under varied injection current levels. It is found that the EL spectra of the InAs QD SLEDs exhibit a uniform broadening in the injection current ranging from 50 μA to 100 mA, which corresponds to a current density from 371 mA/cm^2 to 741 A/cm^2, respectively. At 100 mA injection current, the InAs QD SLEDs exhibit a broad and uniform spectrum with a

linewidth of 100 nm and 218 nm at 3 dB and 10 dB, respectively. The emission spectrum covers the wavelengths ranging from 1.1 to 1.3 μm. In addition, there is no obvious spectrum dip between the ground and excited states observed in the SLED emission spectra across the entire pumping current window. The linewidth broadening indicates the systematic filling of overlapping quantized states in the InAs QDs, which shifts the overall spectra toward the shorter wavelength regime (blue-shift). It is worth noting that in the SLEDs devices, only the ground state emissions is measured to contribute to the output spectra shown in Figure 2-4b.

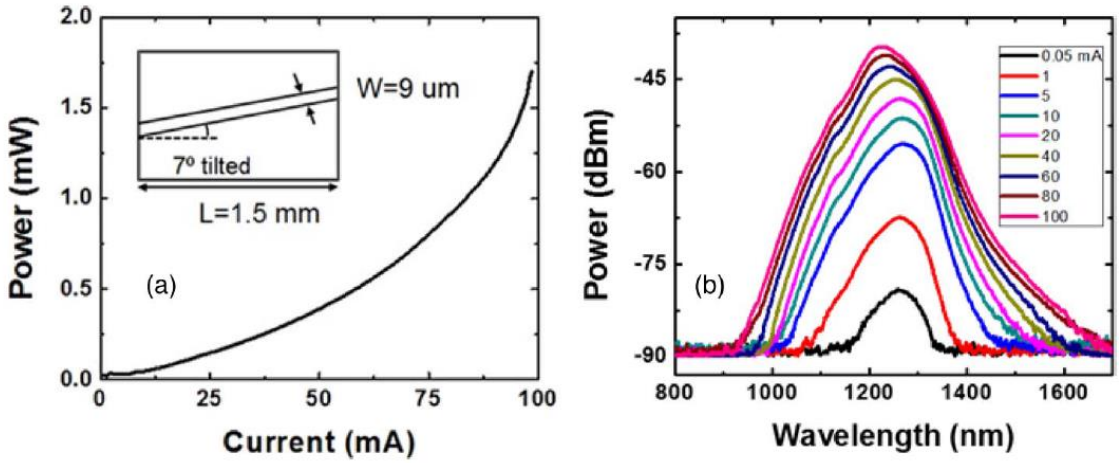

Figure 2-4 (a) Light–current (L–I) characteristics of a SLED with the diagram of device dimensions, i.e.,the cavity length and waveguide width of 1.5 mm and 9 _m, respectively; the superlinear L–I dependence is a signature characteristic of SLED devices. (Inset) Diagram of the titled waveguide design. (b) EL spectra of InAs QD SLEDs at the injection current levels from 50 mA to 100 mA, where the EL spectra exhibit a uniform broadening in the injection current from 50 mA to 100 mA.

2.4 Conclusion

In conclusion, we report the MBE growth and characterization of the broadband InAs QD heterostructures and their SLED devices. The InAs QDs with different SRLs were utilized to achieve the broad emission. The post-growth annealing process can effectively broaden the emission bandwidth and reduce the energy gaps between the ground and excited states in the InAs QDs, which is beneficial to the OCT applications requiring uniform and broadband gain. The InAs QD SLED device exhibited an emission spectrum with power and 3 dB linewidth of 1.5 mW and 100 nm, respectively for a 100 mA injection current level. Further work is under way to optimize the device efficiencies and reduce the device Joule heating. Nonetheless, the characteristics reported here indicate that the InAs QD SLED after some improvement in growth and fabrication can become serious contenders in various broadband applications such as OCT biomedical imaging.

3 HIGH PERFORMANCE INAS QUANTUM DOT LASERS ON SILICON SUBSTRATES BY LOW TEMPERATURE PD-GAAS WAFER BONDING

InAs quantum dot (QD) laser heterostructures have been grown by molecular beam epitaxy (MBE) system on GaAs substrates, and then transferred to Silicon substrates by a low temperature (250 ˚C) Pd-mediated wafer bonding process. A low interfacial resistivity of only 0.2 Ωcm^2 formed during the bonding process is characterized by the current-voltage (I-V) measurements. The InAs QD lasers on Si exhibit comparable characteristics to state-of-the-art QD lasers on silicon substrates, where the threshold current density J_{th} and differential quantum efficiency η_d of 240 A/cm^2 and 23.9%, respectively, at room temperature are obtained with laser bars of cavity length and waveguide ridge of 1.5 mm and 5 μm, respectively. The InAs QD lasers also show operation up to 100 ˚C with a threshold current density J_{th} and differential quantum efficiency η_d of 950 A/cm^2 and 9.3 %, respectively. The temperature coefficient T_0 of 69 K from 60 to 100 ˚C is characterized from the temperature dependent J_{th} measurements.

3.1 Introduction

Silicon photonics is one of the most promising alternatives to electronic interconnects and nearly all of the components of silicon photonic interconnects have been individually demonstrated.[14, 68-71] However, there still remain significant challenges to the realization of complete optical interconnects that are low-cost and have high performance. One of the biggest challenges is the monolithic integration of robust and low-powered lasers with silicon photonic devices. Specifically, current approaches are highly inefficient (<1% efficiency) and are not robust against temperature variations (requires T<40-60 ˚C for operation). [2, 72] In this context, InAs quantum dot (QD) lasers are attractive candidates due to their suitability for high temperature operation.[73-75] Recently, InAs QD lasers were monolithically grown on silicon substrates. [76-78] However, this required the use of Silicon (110) substrates offcut 4-6˚ toward [110] or [111] planes and various buffer layers were employed to reduce the lattice mismatch effects between III-V and silicon, both of which limit CMOS compatibility. Besides these direct growth techniques, wafer bonding technologies have also been used to integrate high performance InAs quantum dots lasers on silicon substrates. [79-81] The performance of such bonded InAs QD lasers is often degraded by the high temperature of the bonding process (> 300 ˚C for at least a few hours)[79-86], which intermixes the InAs QDs and their GaAs capping and spacer layers. On the other hand, it has been demonstrated that Palladium can form a solid alloy with III-V materials, such as Pd_4GaAs or Pd_xInP, by a solid-phase topotaxial reaction at room temperature. This Pd/III-V reaction has previously been used to bond III-V wafers on foreign substrates by E. Yablonovitch et. al. and Bowers

et. al. for electronic transistor applications, [87, 88] and demonstrated that the resulting metallurgical Pd/GaAs bond is an Ohmic contact, a thermal contact and a robust, permanent, adherent contact. However, the application of Pd/III-V low temperature bonding beyond the original electronic applications has not been investigated. In this section, we present the growth, fabrication and characterization of high performance InAs QD lasers on silicon substrates achieved by a low-temperature Pd/III-V bonding process. The advantages of using the Pd-mediated bonding process are also demonstrated and discussed.

3.2 Experiment

Figure 3-1 illustrates the InAs quantum dot laser heterostructures grown on (001) GaAs substrates in a molecular beam epitaxy (MBE) system. The active region contains 7 stacks of InAs QD layers. Each QD layer consists of 2.6 monolayer (ML) InAs grown at 500 ˚C under the growth rate of 0.1 ML/s and capped with 5 nm $In_{0.15}GaAs$. In our dot growth, compared to others,[89] we employed larger dots and small $In_{0.15}GaAs$ capping layer to achieve optimized QD density as well as uniformity and high photoluminescence intensity. In order to increase the temperature performance of the QD lasers, the InAs QDs were modulation doped by beryllium at the concentration of 2×10^{18} cm^{-3}. In the laser heterostructures, the p-type and n-type doped $Al_{0.4}Ga_{0.6}As$ cladding layers are designed to confine the QD emission in the III-V waveguide. Finally, an $Al_{0.85}GaAs$ etch stop layer with a thickness of 30 nm was inserted between the GaAs substrate and InAs QD laser heterostructure. After epitaxial growth, the QD laser heterostructure is bonded to a silicon

substrate in a Karl Suss SB8e substrate bonder by the Pd-mediated bonding process. In this process Ti/Pd with a thickness of 50/250 nm is deposited on a Si substrate by e-beam evaporation. The Ti serves as an adhesion promoter and the Pd is used to form the permanent bond to the GaAs. The III-V wafer is then put in contact with the Pd coated Silicon wafer and several bonding condition combinations were tested (200~350 ˚C, 1000~1500 mbar, 1~4 hour). It was found that permanent bonding can be achieved at a low temperature and time of 250 ˚C and 1.5 hours, respectively, at 1000 mbar pressure which is at least 50 ˚C and 50% less than previously described metal-mediated bonding techniques [79-81]. After bonding, the GaAs substrate is removed by a combination of mechanical polishing and wet chemical etching, where the 30 nm $Al_{0.85}GaAs$ in the heterostructure acts as an etch stop layer. After removing the $Al_{0.85}GaAs$ (HF for 30 s), the ridge waveguide lasers are fabricated by standard process where the waveguide width of 5 µm was fixed and the cavity lengths were varied from 1000 – 2000 µm, respectively. All

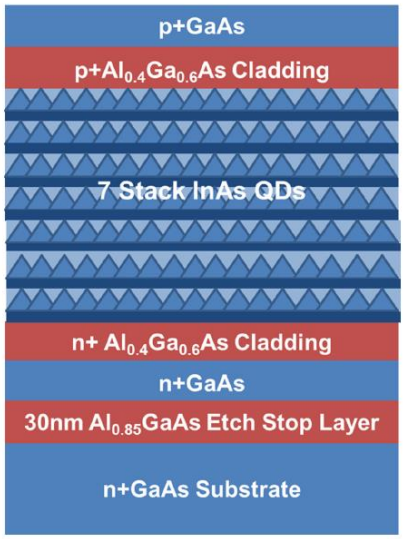

Figure 3-1 Schematic of the InAs QD Laser diode heterostructure.

the laser devices reported in this article are measured with the waveguide facets un-coated (as-cleaved).

The structural properties of the InAs QDs are characterized by atomic force microscope (AFM) and transmission electron microscope (TEM) measurements. In order to perform the AFM measurements, InAs quantum dots without the GaAs capping layers were grown in a separate experiment under the same growth conditions as the ones in the QD laser active regions. Figure 3-1a illustrates the AFM image of the InAs QDs in the area of 1 x 1 μm^2, and it shows that the InAs QDs have density of ~7 x 10^{10} cm^{-2} and average base diameter and height of 45 nm and 8 nm, respectively. The cross-sectional TEM image (Figure 3-2), taken under [110] zone axis illumination, shows that the quantum dots have a dome shape. The dot dimensions appeared to be smaller compared to the ones obtained from AFM measurements due to small strain contrast at the edge of the dots.

3.3 Characterization and Discussion

The electrical characteristics of the InAs QD lasers on Silicon are measured with a customized probe station, where the samples are loaded with n-side up on a thermoelectric cooler (TEC) stage, and, consequently, the device temperature was controlled by the TEC during the measurements. In order to characterize the series resistance at the Pd/III-V bonding interface, a highly doped p-type GaAs substrate was bonded to a low resistance p-type doped silicon substrates with the bonding recipe described above, and a mesa in the GaAs with a size of 0.4 cm^2 was etched to the Pd bonding interface. The top Ohmic metals to the p-type GaAs and bottom Ohmic metals to the Si consisted of Ti/Pt/Ti/Au with the

thickness of 20/20/20/300 nm and 200 nm of Aluminum, respectively. As shown in Figure 3-2b, the I-V characteristics between the top GaAs and bottom Si contacts exhibit a linear behavior and shows that the Ti/Pd contact is ohmic to both the Si and GaAs substrates. Specifically, the low temperature Pd-mediated bonding shows a very low interfacial resistivity of only 0.2 Ωcm^2, which is comparable to direct fusion bonding and other metal bonding results with the resistivity varying from 0.1-1.3 Ωcm^2.[81] Moreover, the solid line in Figure 3-2b shows the I-V characteristics between the top GaAs contacts and Pd contact, where it exhibits nearly the same electrical characteristics with slightly lower interfacial resistivity compared to the one obtained from the top/bottom contacts which is 0.24 Ωcm^2 (dotted line). The inset diagram in Figure 3-2b illustrates the current path in the measurements. The low contact resistance of the back contact is a unique advantage of this Pd-mediated bonding approach as it allows for convenient backside electrical contact to the III-V devices bonded to the Silicon substrate.

The optical characteristics of the InAs QD lasers are seen in Figure 3-3a. The solid curve shows the continuous-wave (cw) light-current (L-I) characteristics of the bonded InAs QD lasers with a cavity length and waveguide width of 1.5 mm and 5 μm, respectively, where a threshold current density J_{th} and differential quantum efficiency η_d of 240 A/cm^2 and 23.9%, respectively, is obtained at room temperature operation. In addition, an output power of ~5 mW is obtained (from both facets) at an injection current of 45 mA. The lasing spectrum of the hybrid InAs QD lasers is shown in the inset of Figure 3-3a and measured at room temperature with the injection current of 27 mA ($1.5I_{th}$). The lasing emission is around 1.24 μm, close to the O-band communication wavelength. The relatively large blueshift between the gain peak and lasing peak is due to the minimized heating effect and band filling effect in QDs.[90] Overall, the laser properties shown here

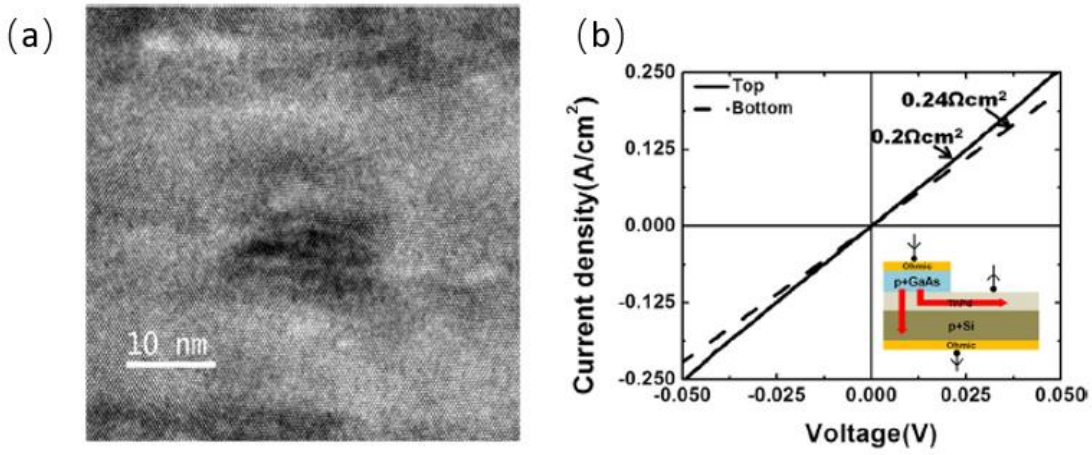

Figure 3-2(a) HR-TEM images of the InAs QDs; (b) I-V characteristics of the bonding structure with top contact and bottom contact method,respectively. The inset shows a schematic of the bonding structure.

are comparable to state-of-the-art self-assembled InAs quantum dots lasers on silicon substrates, where threshold current densities from 163 A/cm^2 to 900 A/cm^2 have been

reported with varied cavity length (0.6~3.5 mm) and ridge width (4~30 μm).[76, 77, 91-93]

In order to study the influence of the wafer bonding process, identical ridge waveguide laser devices were made on a native GaAs substrate. The results are seen in the

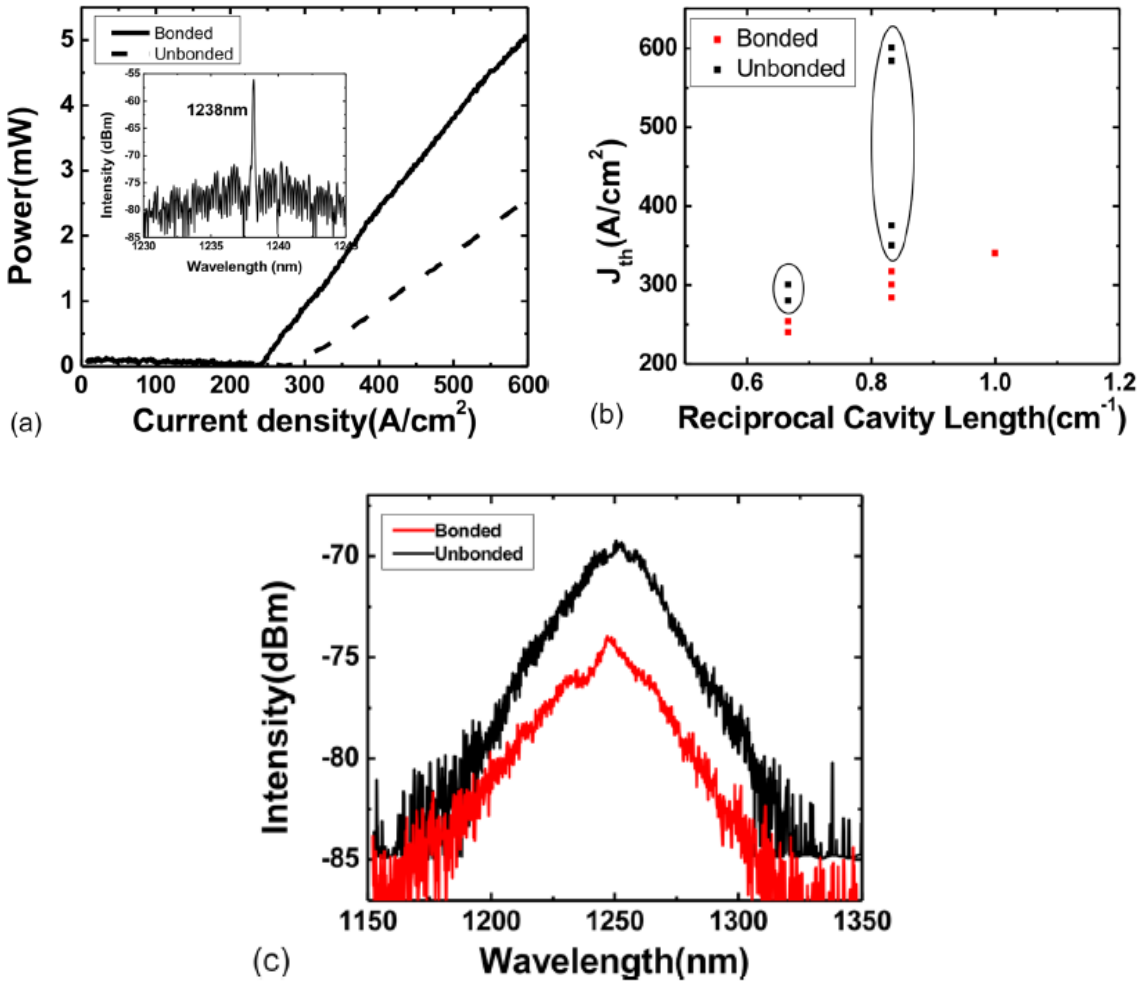

Figure 3-3(a) Light current (L-I) characteristics of the bonded laser (solid line) and the unbonded laser (dashed line). The inset shows the electroluminescence (EL) spectrum of the bonded laser. Both the bonded and unbonded lasers have a cavity length and waveguide width of 1.5 mm and 5 μm, respectively. (b) Measured threshold current density of the bonded and unbonded (circled) lasers of different reciprocal cavity lengths. (c) emission spectra of the bonded and unbonded lasers below threshold ($0.9I_{th}$)

dotted line in Figure 3-3a and an overall comparison is shown in Figure 3-3b. It is clear

that the bonded laser has better performance as it exhibits a lower threshold current density and improved slope efficiency (240 A/cm^2 and 23.9% for the bonded compared to 280 A/cm^2 and 10.4% for the unbonded). In addition, as seen in Figure 3-3b, this improved performance is consistently observed for multiple lasers of different cavity lengths. We do note that there is some variation in the unbonded lasers that we believe is due to un-optimized cleaving of the facets across the entire chip but even with this the improvement from bonding is clear. It is believed that the improved performance of the bonded laser can be attributed to the low temperature wafer bonding process and better heat dissipation through the Si substrates compared with the original GaAs substrates,[94, 95] where the thermal conductivity of silicon is three times larger than the one of GaAs (156 W/(m·K)) compared to 46 W/(m·K)). Finally, Figure 3-3c shows the emission spectra of the bonded and unbonded lasers below threshold ($0.9I_{th}$), where it is seen that both the spectrum shape and peak position were preserved after the bonding process. Thus, this observation also implies that the low temperature bonding process has negligible effect on the QD properties. This p-side down bonding configuration were simulated by using Lumerical Device Heat Transport (HT) to further investigate the heat transfer profile between bonded and unbonded lasers. The heat sources were defined in active regions of lasers, and the temperature were increased to 373K within 1 μs. The simulation heat transport profiles are shown in Figure 3-4, and Figure 3-4b shows the results of heated transformed at 1 μs which clearly illustrated the bonded laser could spread heat more efficient than the unbonded laser.

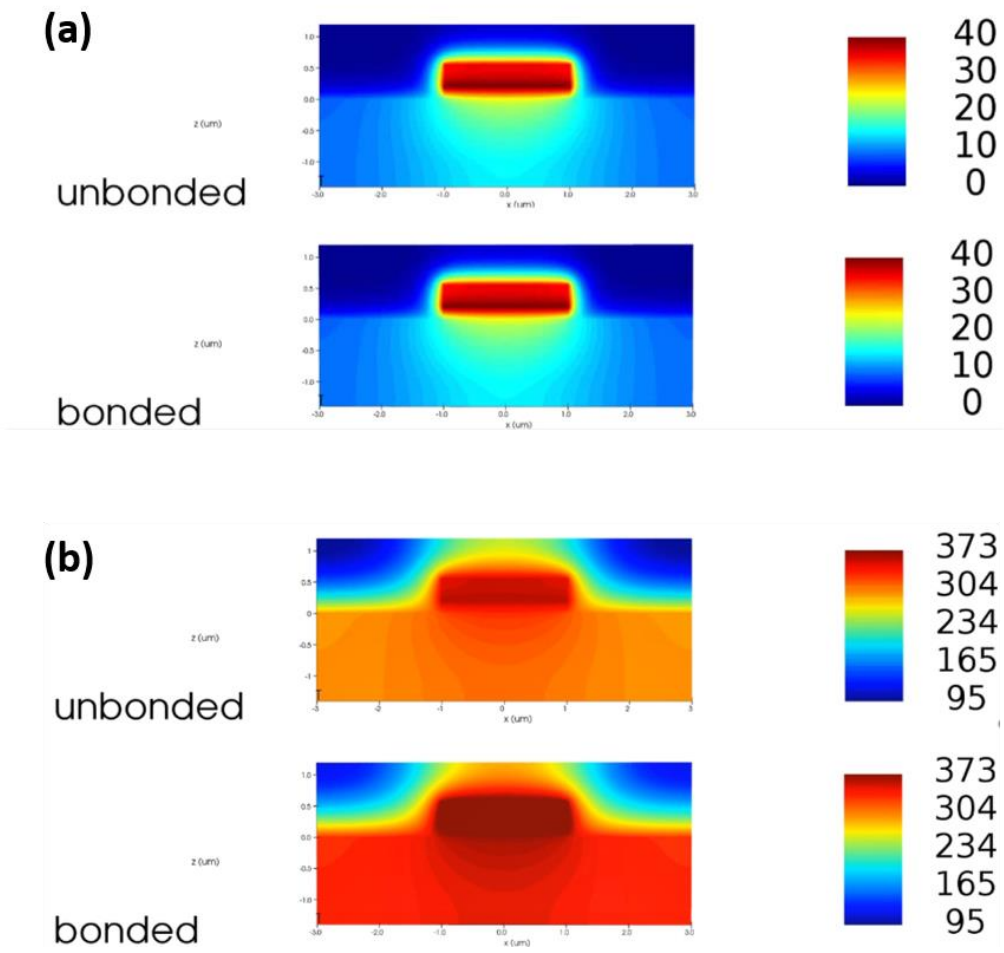

Figure 3-4 Heat transfer simulation thermal profile of bonded and unbonded lasers at temperature of (a) 0k and (b)373K.

This is also seen in Figure 3-5a which illustrates the L-I characteristics of the bonded InAs QD lasers at high temperatures from 60 to 100 ˚C, where a threshold current density, J_{th}, and efficiency, η, of 950 A/cm^2 and 9.3%, are achieved at 100 ˚C operation. We believe the power fluctuations are due to the high current density through the electrical probes used

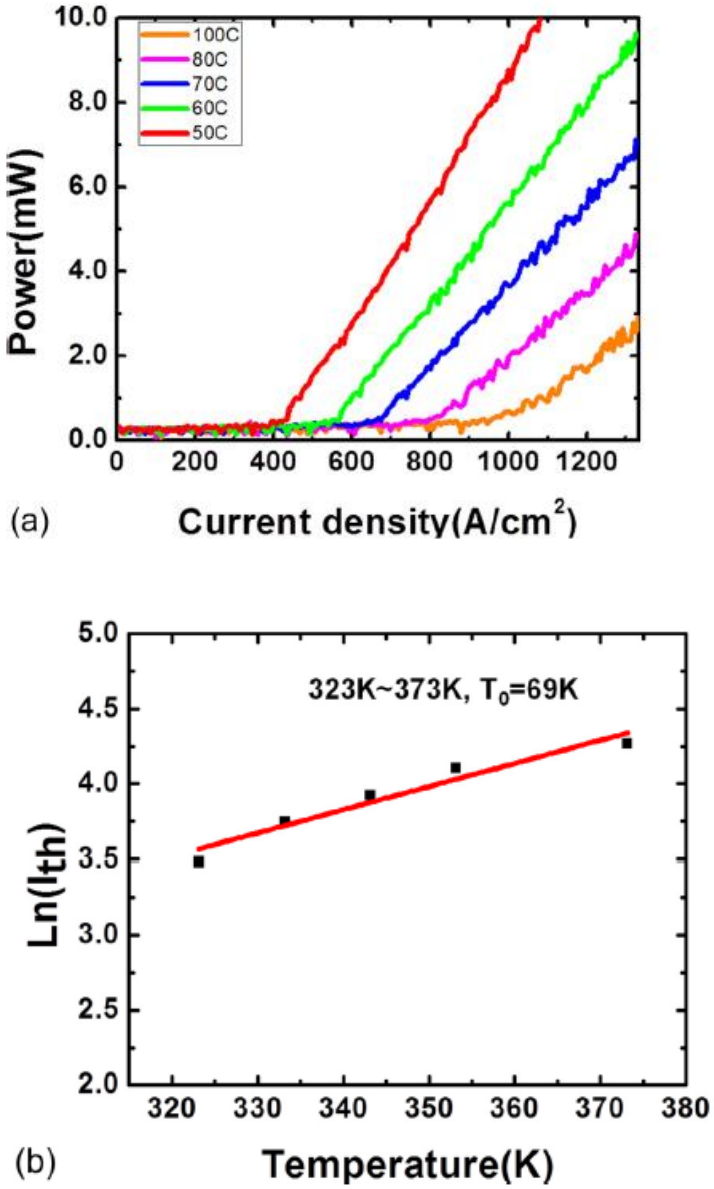

Figure 3-5 (a) Light-current (L-I) characteristics of bonded laser under the different operation temperature from 50˚C to 100˚C with the laser cavity length and waveguide width of 1.5 mm and 5 μm, respectively. (b) Natural logarithm of the threshold current versus stage temperature for the bonded laser with the same device in Figure 3-3a.

to contact the lasers. The measured temperature dependence of threshold current is shown in Figure 3-5b for a laser with a cavity length of 1.5 mm. The corresponding temperature coefficient T_0 of 69 K is obtained which is higher than other state of art hybrid lasers (~50

K),[76, 77, 96, 97] and the T_0 could be improved further by optimizing the p-type modulation doping of the quantum dots. [98, 99]

Some high-speed laser characterizations are also tested for this bonded laser. The test set up was shown in Figure 3-6a which consisted of two DC probes to operate laser beyond threshold current and a GSG RF probe to direct modulate laser. Figure 3-6b shows the eye diagrams characterizations by modulating the bonded laser directly from 1GHz to 5 GHz, the Pseudorandom Bit Streams (PRBS) rate is 2e7-1 and the RF signal Vpp is 300mV. As shown in Figure 3-6b, the distinction ratio was getting worse and the eye patterning became blurred at 5GHz modulation rate. Figure 3-6 c shows the small-signal modulation characteristics with different DC injection current. At 145mA, the 3dB-down modulation bandwidth reached 2 GHz. Since we haven't applied any design for high-speed laser operation for our boned QD laser epitaxy structure, the bonded laser can be only modulated up to 5GHz. However, we believe by introduced the design such us p-modulation doping, narrower barrier height and tunneling injection structure of epitaxy design, the modulation rate could be dramatically increased.

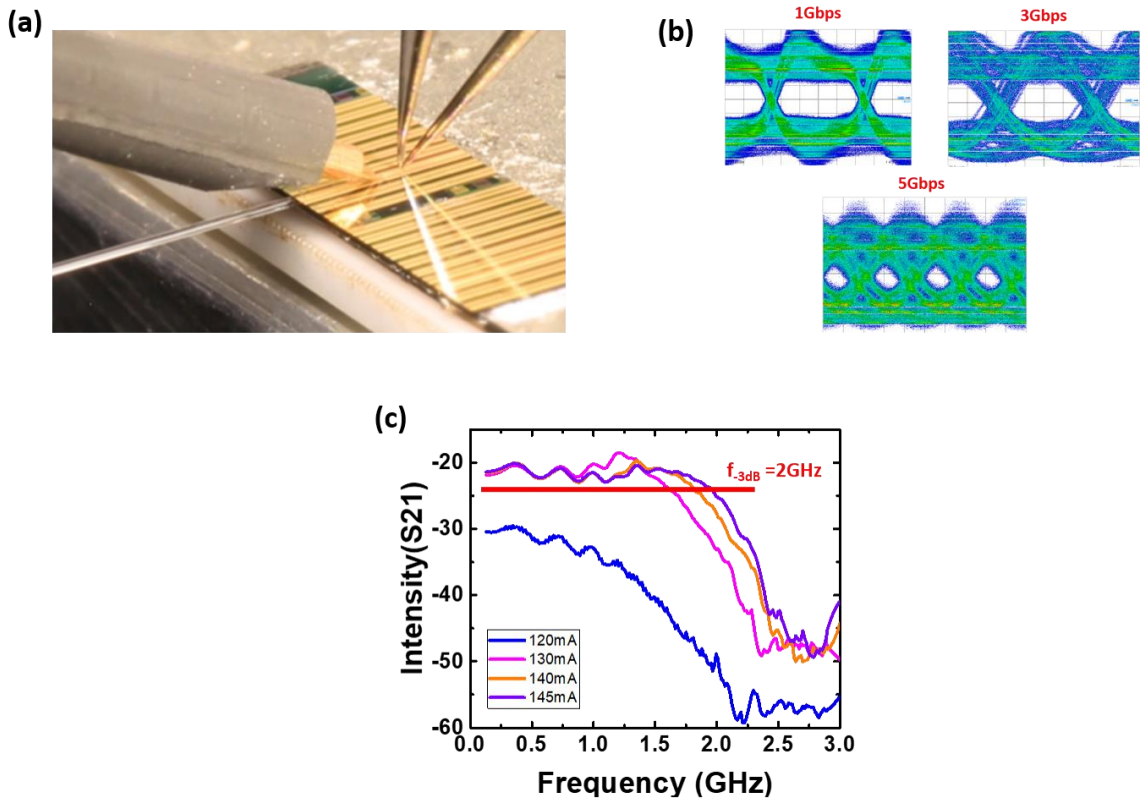

Figure 3-6 (a) High-speed laser characterization setup. (b)Eye diagram characterization of bonded InAs quantum dot lasers. (c) Small signal modulation characteristics of InAs bonded lasers.

3.4 Conclusion

In conclusion, a low interfacial resistivity, low-temperature Pd-mediated wafer bonding technique has been used to realize high quality InAs QD lasers on silicon substrates. The bonded lasers exhibited better performance than their unbonded counterparts, with a threshold current density and slope efficiency of 240 A/cm^2 and 23.9%, respectively, at room temperature. The InAs QD lasers on Si also yielded operation at up to 100 ˚C with no significant performance degradation. In addition, high-speed

modulation characteristics such as eye diagram and small signal modulation were also investigated which indicated the bonded laser can be operated up to 5 GHZ. After further optimization of the device efficiency and epitaxial process, the present hybrid InAs QD lasers can be made to operate at 1.3 μm, which will play a significant role for future silicon photonic integration.

4 INAS QUANTUM DOT COMB LASERS ON SILICON SUBSTRATES BY WAFER BONDING

InAs quantum dot (QD) comb lasers have been grown by molecular beam epitaxy (MBE) system, and integrated on silicon substrates by a low-temperature Pd-mediate wafer bonding process. A post-growth annealing process is employed to achieve the broad and uniform gain spectrum for the multi-wavelength comb lasers. The InAs QD comb lasers have a threshold current density J_{th}, and slope efficiency, η_i of 320 A/cm2 and 23.8%, respectively. Under the injection current of $4.37J_{th}$, the QD comb lasers exhibit multiple broad and uniform longitudinal modes with the 3 dB bandwidth of 20 nm. Further study has shown that the InAs comb lasers exhibit a continuous bandwidth broadening under increased injection currents, which is ideal for the multi-channel optical interconnection designs.

4.1 Introduction

In the research of silicon photonics, nearly all of the silicon photonics interconnect components have been individually demonstrated, such as, lasers, modulators and detectors with the performance competitive with the electronic-only counterparts.[14, 92, 100-102] One of the biggest challenges is the seamless integration of robust and low-powered lasers with other silicon photonics devices, where the lasers need to be operated at relatively high ambient temperatures (70-80˚C) and the emission wavelengths need to be varied to achieve a multichannel laser array with large transmission bandwidth. The large lattice and thermal mismatch between Si and III-V materials limits the performance and reliability of III-V lasers monolithically grown on Si.[103, 104] In this context, III-V heterostructures bonded on substrate have accentuated the Si photonics research, where the III-V active materials are usually bonded on the Si platform and the emissions are evanescently coupled with the underneath silicon waveguides. Due to the 3D confinement and delta-function like density-of-states (DOS) in quantum dots, it is well understood that the QD lasers, compared to their QW counterparts, are advantageous in temperature stability and power consumption. In addition, due to the size inhomogeneity of QDs, QD lasers usually exhibit broad gain spectrum, and QD comb lasers with uniform and broad emission spectrum have been demonstrated.[105-107] Such unique broadband laser sources have the potential to replace a laser array with a single comb laser, and to enhance the total power consumption efficiency (power/bits). However, integrated QD comb lasers have not yet been demonstrated on Si substrates to take the advantage of the broad gain spectrum of QD

heterostructures. In this section, we present the growth and characterization of InAs comb lasers on Si substrates by low temperature metal-mediate wafer bonding techniques.

4.2 Experiment

Figure 4-1 illustrates the InAs quantum dot laser heterostructures grown on (001) GaAs substrates in a Veeco GEN II molecular beam epitaxy (MBE) system. The active region contains 7 stack of InAs QD layers. Each layer consists of 2.6 monolayer (ML) InAs QDs grown at 500 ˚C at the growth rate of 0.01 ML/s. The p-type and n-type doped $Al_{0.4}Ga_{0.6}As$ cladding layers are designed to confine the QD emissions in the III-V waveguides. Finally, an AlAs etch stop layer with the thickness of 20 nm was inserted between the GaAs substrates and InAs QD laser heterostructures. In order to achieve the broadband gain emission, each InAs QD active region was tuned by carefully changing the QD growth conditions. *In-situ* annealing under As2 overpressure before and after QD formation was also performed to enhance QD size inhomogeneity. In addition, the as-grown QD heterostructures were annealed *ex-situly* in a rapid thermal annealing (RTA) process at 700 ˚C for 60 sec, which can effectively enhance the inter-diffusion between the InAs QD and the affinity GaAs capping regions and further increase the gain linewidth. This annealing method has been employed by several groups to obtain broadband InAs QD based gain devices.[65] After the epitaxy growth, the QD laser heterostructures were bonded to silicon substrates in a Karl Suss substrate bonder. The bonding process was carried out at 250˚C and 1000 mbar pressure for 1.5 hours. The detail of the Pd-mediate bonding process has been previously reported and the low temperature bonding process is beneficial to the QD laser applications. After the wafer bonding process, the GaAs

substrates were removed by the combination of mechanical polishing and wet chemical etching, where the AlAs layer in the heterostructures act as the etch stop layer, and then the AlAs etch stop layers were removed by dipping in HF solution for 30 sec. In the end, the broad area QD lasers were fabricated by standard photolithography, wet chemical etching, contact metallization, and cleaving techniques, where the waveguide width and the cavity length were varied from **5 to 9 µm and 1000 – 2000 mm**, respectively. All the QD laser characterization results reported here were performed with the waveguide facets un-coated (as-cleaved).

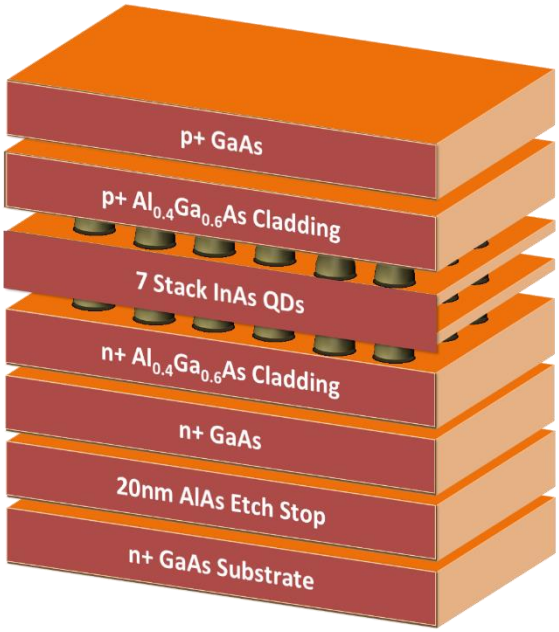

Figure 4-1 Schematic of the InAs QD superluminescence light emitting diode heterostructures

The structural properties of the InAs QDs were investigated by atomic force microscope (AFM) and high transmission electron microscope (HR-TEM) measurements. As illustrated in AFM image in Figure 4-2 inset, the InAs QDs have an areal density of ~8 x 10^{10} cm^{-2} and average size and height of 30 nm and 6 nm, respectively. It is also found that our optimized dot growth conditions and *in-situ* annealing techniques can effectively reduce the number of the coalesced QDs, which have previously been reported to behave as the dislocation and non-radiative recombination centers and play detrimental roles in the QD device applications. The cross-sectional TEM images in Figure 4-2 shows the 7 stack quantum dots with a dome shape. The TEM images were taken under [110] zone axis illumination with a FEI F20 TEM system.

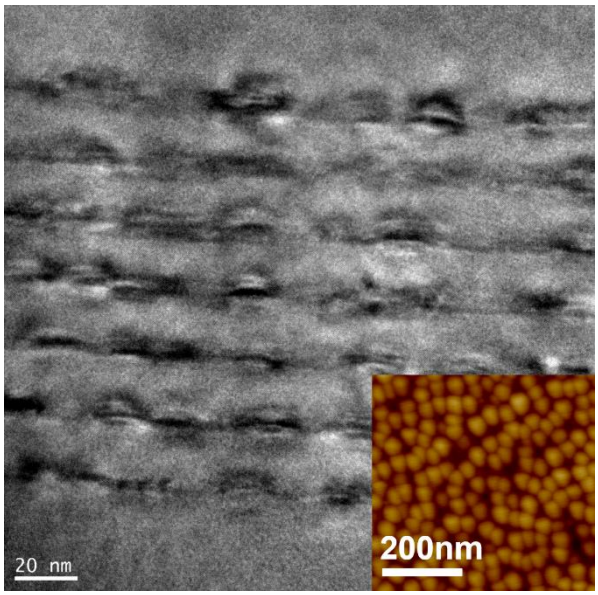

Figure 4-2 HR-TEM images of 7 stacks layers of the InAs QDs. Inset: AFM images of QDs.

4.3 Characterization and Discussion

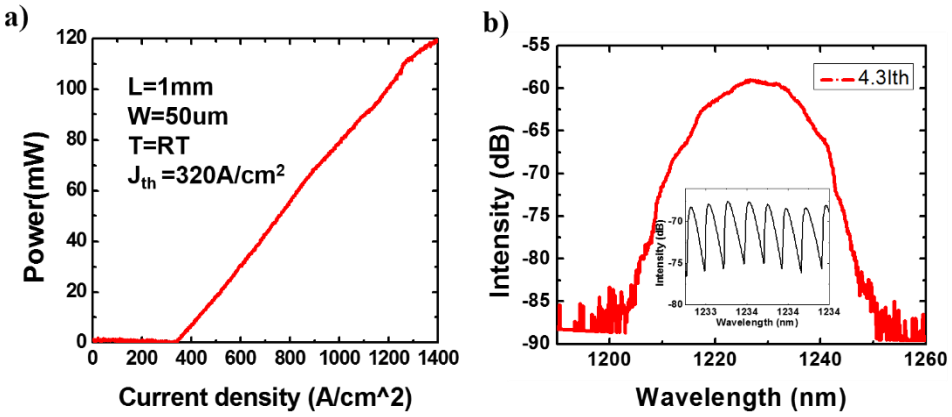

Figure 4-3(a) Light-current-voltage (L-I-V) characteristics of a SLED with the cavity and waveguide width of 1 mm and 50 µm, respectively; (b) EL spectra of InAs QD SLEDs at the injection current of 1400 A/cm^2, the emission spectrum has a linewidth of 20 nm and 30 nm at 3 dB and 10 dB, respectively.

The electrical characteristics of the QD lasers on silicon substrates were measured with a modified Cascade Microtech Alessi 3200 probe station, where the samples were loaded with n-side up on a thermoelectric cooler (TEC) stage and the sample temperature was precisely controlled and varied from 10 to 100 ˚C during the measurements. Figure 4-3a shows the light-current (L-I) characteristics of a QD comb laser with the cavity length and waveguide width of **1 mm and 50 µm**, respectively. The threshold current density, J_{th}, and slope efficiency, η, of 23.81% and 320 A/cm^2, respectively, are obtained from the L-I characteristics. Figure 4-3b illustrates the comb laser electroluminescence (EL) spectra under injection current 1400A/cm^2. The continuous broadening of the EL spectra can particularly benefit the silicon integration designs, where only 4 to 8 independent transmission channels are needed for current generation. It also provides the capability to extend to the design requiring more channels in the future without pursuing a different

comb sources. The insert Figure 4-3b shows a high-resolution spectrum at injection current of 4.3Jth measured at 300K, and each longitudinal mode can be clearly distinguished with the mode spacing of 0.1 nm. The measured mode spacing agreed very well with the theoretically predications. For the laser with a **1 mm** cavity length, there are 200 simultaneously emitted longitudinal modes in the spectral range of 1217–1237nm with a non-uniformity of the peak intensity of less than ~0.5 dB.

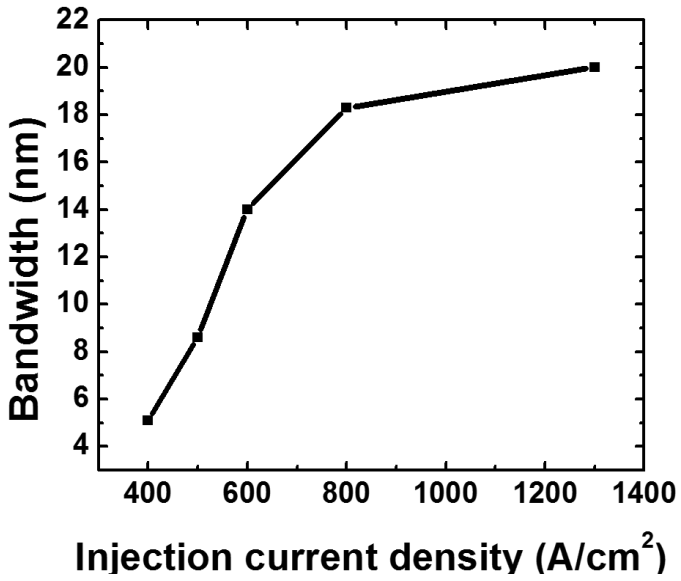

Figure 4-4 Injection current vs. peak wavelength position, where the continuous blue-shift of peak emission indicates the quasi-continuous interband transition characteristics in QDs

Finally, Figure 4-4 shows the bandwidth (dotted line) of the QD comb sources vs. injection currents. The bandwidth broadening effects started to saturate at injection current higher than 800A/cm2, which may due to the Joule heating effects and could be improved by the better packaging such as using heat sink submount and wire bonding. It is worth noting that, although the bandwidth of the reported QD comb laser sources on silicon

substrates is at least three time narrower than the state-of-the-art QD comb lasers on the native GaAs substrates, the 20 nm bandwidth is more than adequate for the current 4 channels design standards for both the dense wavelength-division multiplexing (DWDM) and 2 channel coarse wavelength-division multiplexing (CWDM) arrays.

4.4 Conclusion

In conclusion, we report the MBE growth and characteristics of the InAs comb lasers sources on silicon substrates. The post-growth annealing process can effectively enhance the InAs gain spectrum. The emission spectrum with the 3dB and 10 dB linewidth of 20nm and 30 nm, respectively, are obtained at the injection current of 1400A/cm^2. Further work is under way to optimize the device efficiencies and reduce the device Joule heating. Nonetheless, the characteristics reported here indicate that the InAs QD comb lasers after some improvement in growth and fabrication can become serious contenders in silicon photonics integrations.

5 PASSIVE MODE-LOCKED INAS QUANTUM DOT LASERS ON SILICON SUBSTRATE BY PD-GAAS WAFER BONDING

We demonstrate an electrically pumped InAs quantum dot (QD) two-section passively mode-locked laser (MLL) on a silicon substrate by low temperature (250 °C) Pd-GaAs wafer bonding technology. The saturable absorber of the QD-MLL is electrically isolated by a 15 μm wide dry-etching gap which resulted in ~30 kΩ resistance from the gain regions of the MLL. At room temperature the laser operates in the O-band (1.3 μm) telecommunication wavelength regime with threshold current of 94 mA, laser bar cavity and absorber lengths of 6 mm and 300 μm, respectively. The optimum mode-locked conditions are observed under injection current and reverse bias voltage of 124 mA and -7 V, which generates pulses at a repetition rate of 7.3 GHz, an optical bandwidth of 0.97 nm, and a nearly transform limited pulse width of 2 ps (sech2 pulse profile). These results enable QD-MLLs to be integrated with silicon photonic integrated circuits (PICs), such as optical time division multiplexing (OTDM) and optical clocks.

5.1 Introduction

Silicon photonics is one of the most promising solutions to achieve low cost CMOS-compatible photonic integrated circuits (PICs) and nearly all the components of silicon photonics interconnections have been individually demonstrated.[14, 71, 108-110] However, a proper way to monolithically integrate robust and efficient lasers into silicon photonics platform is still under investigation. Specifically, current approaches are highly inefficient (<1%) and not robust against temperature variations (requires T<40-60˚C for operation).[2, 111] An attractive solution to these problems is the use of InAs quantum dot (QD) lasers due to their capability for high temperature operation. [73-75] Recently, InAs QD lasers were monolithically grown on silicon substrates.[25, 112, 113] However, these novel direct growth technologies require 4-6˚ off-cut or pre-patterned silicon substrates and thick buffer layers to eliminate threading dislocations (TDs) between Si and GaAs, both of which limit CMOS compatibility. Alternatively, QD lasers on Si have been demonstrated using wafer bonding technologies where the performance is influenced by the high temperature during the bonding process.[79, 81] Recently we have demonstrated a metal wafer bonding platform using Palladium (Pd) to integrate InAs QD lasers on silicon substrates with a very low bonding temperature (<250 ˚C). [114] This metal mediated bonding process provides ohmic contact to Silicon and excellent thermal conductivity, resulting in p-side down bonded lasers with enhanced performance over counterparts on native GaAs substrates.[114] Here, we experimentally demonstrated a mode-locked QD laser on Si at a repetition rate of 7 GHz by using this Pd wafer bonding platform.

Mode-locked lasers generate ultrashort pulses from durations ranging from femtoseconds to tens of picoseconds with applications in optical clock generation, OTDM, WDM (Wavelength-Division-Multiplexing), and high speed electro-optic sampling systems. In addition to using bulky Ti:sapphire lasers or other vibronic lasers to generate pulses of light, semiconductor mode-locked lasers (MLLs) and hybrid quantum well MLLs have been demonstrated in the near infrared, which provide opportunities for photonic integration.[115-117] Compared to quantum well lasers, QD lasers are well suited for mode-locked applications due to their inhomogeneous gain spectrum and ultrafast carrier dynamics.[19] Currently, ultrafast, high repetition rate, low-jitter, temperature insensitive quantum dot mode-locked lasers (QD-MLLs) have been realized.[118-120] To further integrate QD-MLLs into an on-chip system, we have demonstrated an OTDM system using a QD-MLL which produces a 5 Gb/s clock signal externally coupled into a silicon photonics chip, generating a 40 Gb/s signal.[121] In order to integrate the QD-MLLs on chip, we have developed hybrid QD-MLLs on Si using the Pd-GaAs bonding technology. In this section the growth design, fabrication, and characterization of the bonded QD-MLLs will be discussed.

5.2 Experiment

The structure of the hybrid QD-MLL is shown in Figure 5-1(a). The active region was grown by molecular beam epitaxy (MBE) on an n-type GaAs (100) substrate, containing 10 stacks of self-assembled InAs QD layers (grown by Innolume Gmbh, Dortmund, Germany). In this laser heterostructure, the p-type and n-type doped $Al_{0.35}Ga_{0.6}As$ claddings are designed to confine the QD emission in the III-V waveguide.

A 200 nm $Al_{0.7}GaAs$ etch stop layer is grown between the laser structure and GaAs buffer layer for epitaxy membrane transfer. The low temperature Pd-GaAs wafer bonding technology used to fabricate QD- MLLs has been previously developed to make ridge

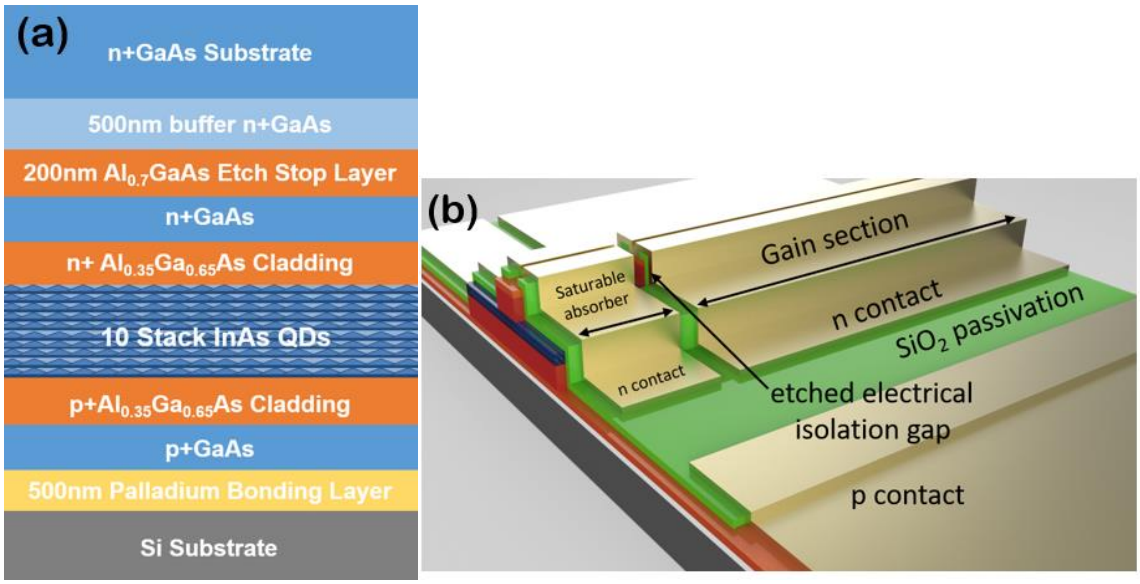

Figure 5-1(a) Heterostructure schematic and (b) diagram of the InAs QD mode-locked laser diode on silicon.

waveguide Fabry-Perot lasers.[114] Additionally, this p-side down low temperature wafer bonding technology shows the potential to enhance heat dissipation properties which lower the threshold current of bonded lasers compared to unbonded ones. The schematic of the passive QD-MLL is shown in Figure 5-1(b), where the MLL has a 6 mm gain section and a 300 μm saturable absorber section separated by a 15 μm wide electric isolation gap. The QD-MLLs are fabricated with waveguide and mesa widths of 5 μm and 25 μm, respectively (Figure 5-2a inset).[114] Electric isolation gaps are made together with the laser ridges by dry etching to a depth of 2 □m (Figure 5-2b). The resistance between the two laser sections is characterized by I-V measurements (Figure 5-2b inset). The measured resistance is ~30 kΩ which allows the sections to be independently biased. After fabricating the QD-MLLs

on Si, the silicon substrate is mechanically polished to a thickness of ~100 µm before cleaving in order to realize a high quality facet (Figure 5-2a). Though the facets could be highreflectivity (HR) coated, for this study the facets were left as cleaved.

5.3 Characterization and Discussion

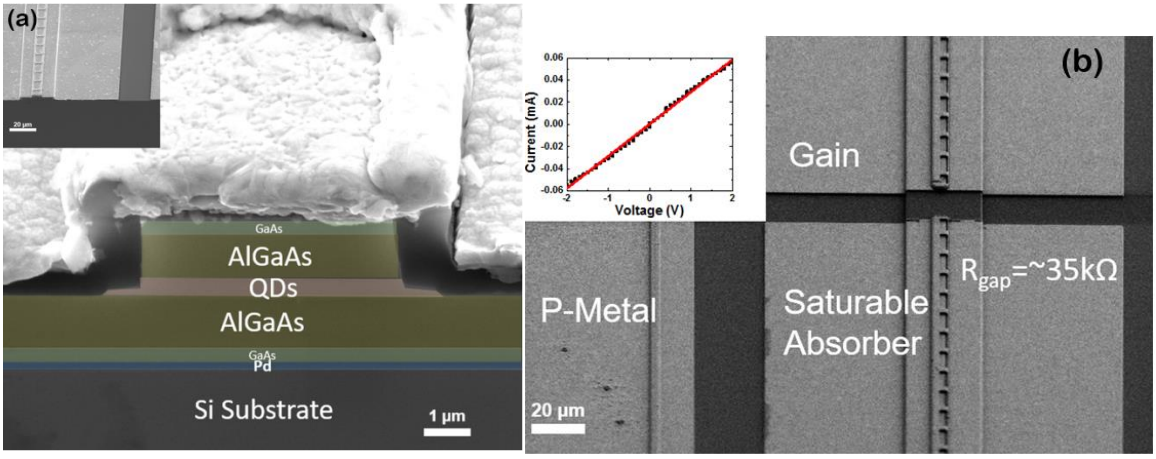

Figure 5-2 (a) Magnified cross-section SEM image of the laser facet with a 70° tilted angle and (inset) unmagnified SEM image of the same region. (b) Top view SEM image and I-V characteristics (inset) of dry etched electrical isolation gap between the gain and saturable absorber sections.

The DC characteristics of bonded QD-MLLs are tested with current injection (I_g) and a constant reverse bias voltage (V_a) applied to the saturable absorber section. The devices are mounted on an aluminum oxide submount using Indium-Tin solder (ribbonin-10809) on top of a thermoelectric cooler (TEC) to maintain room temperature (RT) operation during measurement. The continue wave (CW) light-current (L-I) characteristics of bonded QD-MLLs with forward and backward sweeping of the injection current under zero bias (0 V) and 4 V reverse bias conditions are shown Figure 5-3. When the absorber is short circuited (V_a=0V), the QD-MLL shows a threshold current (I_{th}) of 94mA, and a single facet output power of ~2 mW at an injection current of 130 mA. At a reverse bias of V_a=-4V, the threshold current is increased to 100 mA due to the higher cavity losses

generated from the reverse biased saturable absorber. It is seen that the reverse biased QD-MLL exhibits bistability near the point of threshold. This effect has been observed in unbonded QD-MLLs and is attributed to the nonlinear saturation of the QD absorption and the electro-absorption induced by the quantum confined Stark effect (QCSE). [122]

The RF properties are characterized using a high index single mode fiber (Nufern UHNA) directly coupled from the saturable absorber facet. The coupled light is then sent through an O-band semiconductor optical amplifier (SOA) (Thorlab S9FC1132P) to boost

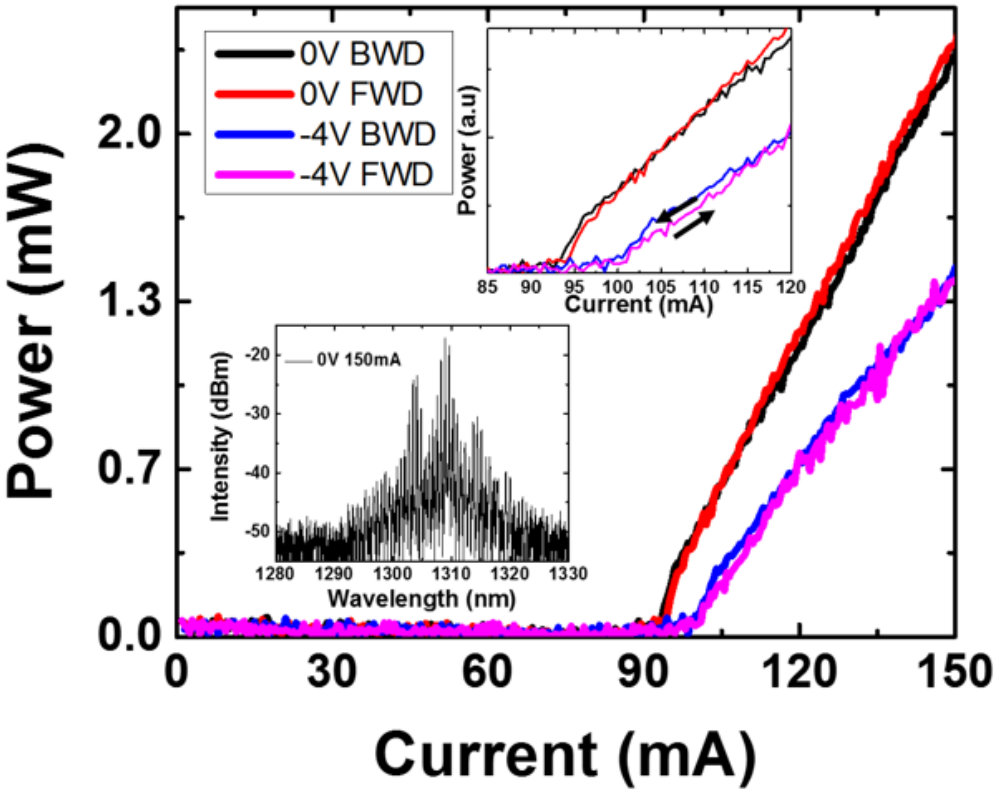

Figure 5-3 Light current (L-I) characteristics of the bonded mode-locked laser under reverse bias voltages of 0V and -4V with forward and backward sweep current. Upper right inset: close-in L-I around threshold current. Lower left inset: electroluminescence (EL) of bonded mode-locked laser with a reverse bias voltage of 0V with injection current of 150 mA.

the power intensity and is followed by an optical splitter for simultaneous characterization of the RF spectrum, optical spectrum, pulse train, and pulse width. In order to characterize the mode-locking dynamics of the bonded QD-MLL, optical and RF spectra 2D evolutions are generated from OSA (optical spectrum analyzer) and RF spectrum analyzer measurements simultaneously. These 2D optical and RF spectra evolutions are characterized over reverse bias voltages from 0 V to -7 V with -1 V steps. Figure 5-4 shows the evolution of the optical and RF spectra at reverse biases of -7V and 0V, respectively, which are selected to indicate the typical differences of bonded MLLs functioning at the two ends of the bias conditions. The RF spectra exhibits mode-locking under high or low reverse bias conditions, however, higher reverse bias voltages result in locking over larger conditions as well as a stronger RF signal due to the faster absorption recovery in the saturable absorber. It is worth noting that the laser operates at a higher RF frequency at higher reverse bias conditions since the elevated bias voltage induces more loss, essentially shortening the cavity length of the laser. In addition, under both reverse bias conditions, the bonded MLL shows a stable narrow RF spectrum around the threshold current, and the linewidth broadens as the optical spectrum transitions from single to dual band with increased injection current. This dual band phenomenon was also observed in InAs/InP QD lasers[123], the band splitting may due to internal optical power, AC stark effect or the pumping effects from another group of QDs. The gap between dual spectral bands results in refractive index differences, leading to two competing groups of pulses in the cavity, which destabilizes operation. Optimum mode-locking conditions are achieved under high

reverse bias with an injection current set below the bifurcation of the optical spectrum. This set of conditions usually occurs around the threshold current (V_a=-7 V and I_g=124 mA).

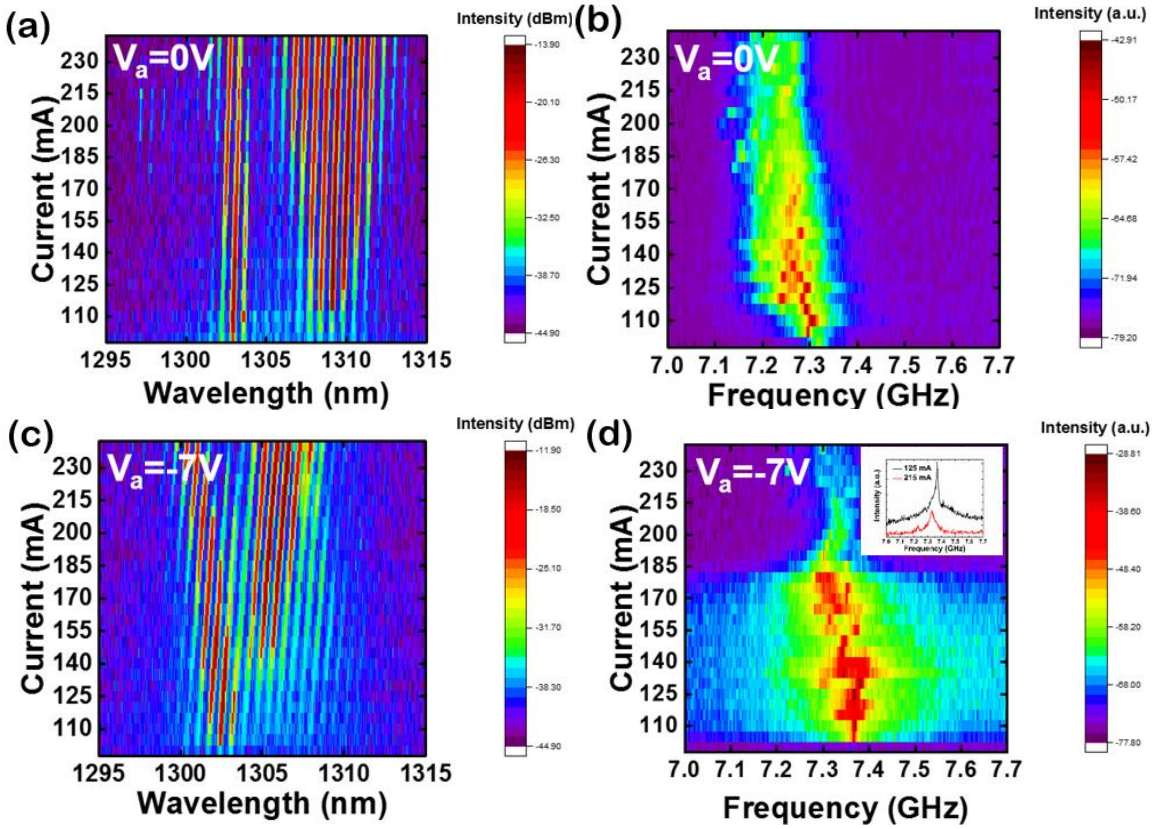

Figure 5-4 (a) Optical and (b) RF spectra evolutions with injection current from 100 mA to 240 mA at 0V bias. (c) Optical and (d) RF spectra evolutions with injection current from 100 mA to 240 mA at -7V bias. Inset: RF spectra at optimized injection (I_g=125 mA) and at bifurcated spectrum operation (I_g=215 mA). The RF signal degrades significantly at higher injection currents where the optical spectrum splits.

Under these optimized MLL conditions we have characterized the temporal and spectral characteristics of the laser. In Figure 5-5a inset, a pulse train is observed by using a digital sampling oscilloscope with an optical detection module and triggered with an amplified RF signal. The pulse period is approximately 136 ps, in agreement with the 7.3 GHz RF spectrum shown in Figure 5-5a, and corresponding to the fundamental cavity

repetition rate. The side peaks and broadened pulse width observed in each pulse are due to the non-ideal response of the photodetector. In order to measure the actual pulse width, the SOA amplified pulse train is sent into a Femtochrome autocorrelator (FR-130HS). Figure 5-5b inset shows the autocorrelation trace with a Full-Width-Half-Maximum (FWHM) of 2.96 ps, which corresponds to a deconvolved 1.9 ps pulse using a $sech^2$ fitting. The corresponding optical spectrum is measured to have a FWHM of 0.97 nm [~172 GHz] (Figure 5-5b). The resulting time-bandwidth product is 0.326 which is comparable to the $sech^2$ shape Fourier transfer limited theoretical value of 0.315, i.e. 1.029X the transform limit or within 5% of our experimental value. The asymmetric pulse shape is attributed to gain clipping in the SOA, or chirp effects inside the bonded MLL. [124, 125]

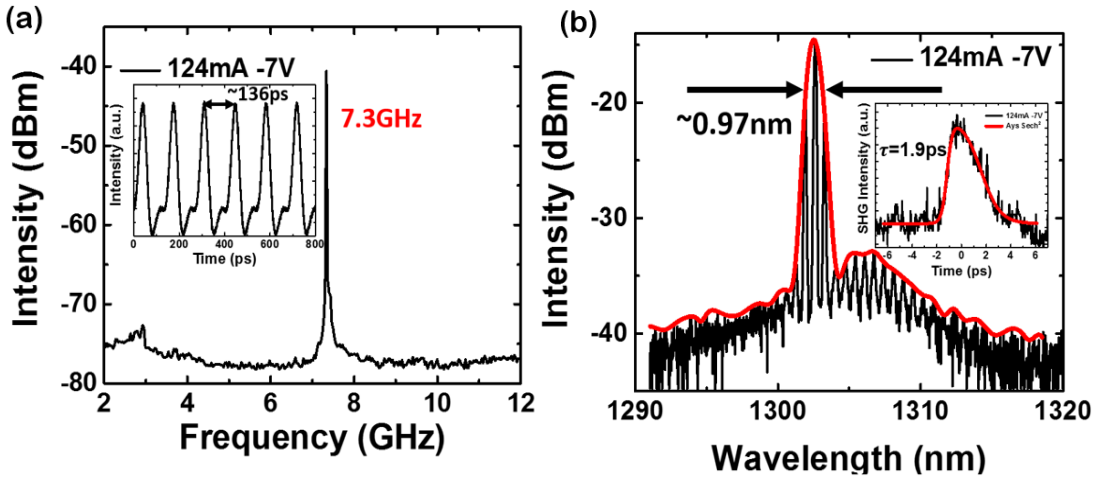

Figure 5-5 (a) RF spectrum and pulse train (inset); (b) optical spectrum and temporal pulse width (inset) of bonded mode-locked QD laser under the optimized bias condition of I_g=124 mA and V_a=-7 V, respectively.

Other than two-section mode-locked laser configurations, a single cavity mode-locked laser and colliding pulse mode locked laser are also investigated. The schematic device structures of these three configurations are shown in Figure 5-6.

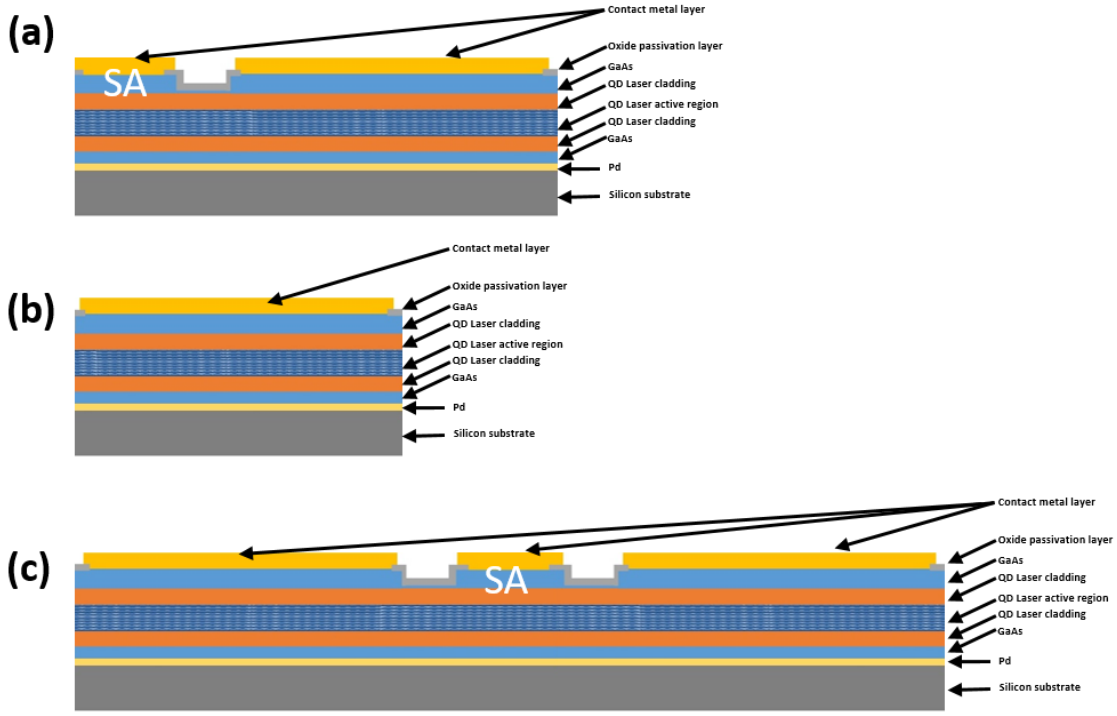

Figure 5-6 Schematic drawing of three configurations for passive mode-locked laser: a) two section mode-locked laser, b) single cavity mode-locked laser, and c) colliding pulse mode-locked laser.

For the single cavity mode-locked laser, the physics modeling still haven't fully modeled yet. One qualitied explanation is as laser turning on, the self-focusing effect made the middle region of laser having lower loss caused by the smaller mode profile reduced the interaction with surface of laser waveguide. As a result, the middle part become to be the saturable absorber of the single laser cavity and eventually mode-locked the whole cavity. Since there was no electro isolation in this configuration, which means lower loss and higher efficiency compared to the two section mode-locked laser. However, this

configuration cannot apply bias on the saturable absorber and the pulse may not be suppressed to very narrow pulse width in time domain. Figure 5-7 b shows the RF spectrum of a single cavity MLL bonded on Si substrate.

For the colliding pulse mode-locked (CPM) laser configuration, the mechanism is quite similar to the two section MLL, however, the saturable absorber is designed in the middle of the cavity. As a result, the two colliding pulses generated from the gain section on each end of laser cavity will transport against each other can be bleached out more easily in the middle SA section compared to the two section one. This process are supposed to generate in shorter and more stable pulses. Figure 5-7a shows the RF spectrum of InAs QD CPM lasers on Si by Pd-GaAs wafer bonding. As it configuration defines, the second harmonic of fundamental frequency were generated. As a tradeoff, these CPM configuration need the laser cavity to be designed two times longer than the two section one.

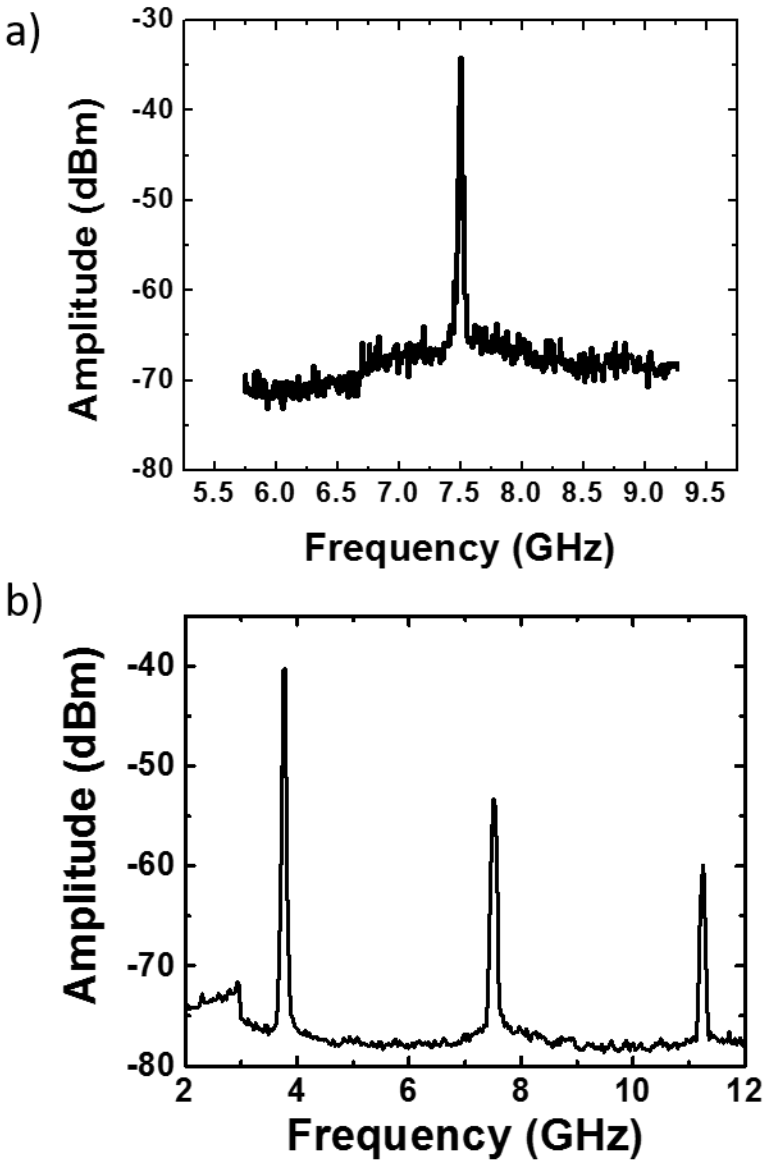

Figure 5-7 a)RF spectrum of colliding pulse QD mode-locked laser and b) RF spectrum of a single cavity mode locked laser bonded on Si.

5.4 Conclusion

In conclusion, we have demonstrated for the first time nearly transform limited quantum dot mode-locked lasers on silicon by low temperature Pd-GaAs wafer bonding

technology. The optimized mode-locked lasers operate near 1.3 μm with a 7 GHz repetition rate and 2 ps pulse width. In addition, mode-locking was investigated over a wide range of operating conditions by adjusting gain injection currents and reverse bias voltages of the saturable absorber. In addition, the single cavity mode-locked laser and colliding pulse mode-locked InAs QD laser are also demonstrated on Si with the preliminary results. These hybrid InAs QD MLLs are a promising solution to integrating laser sources together with silicon photonic integrated circuits (PICs).

6 CHARACTERIZATIONS OF OPTICAL FEEDBACK EFFECTS IN INAS QUANTUM DOT LASERS BUTT-JOINT COUPLED WITH SILICON PHOTONICS WAVEGUIDES

InAs quantum dot (QD) laser heterostructures have been grown by molecular beam epitaxy (MBE) system on GaAs substrates. The InAs QD lasers exhibit comparable properties of the state-of-the-art QD lasers on silicon substrates with the threshold current density J_{th} and efficiency η of 475A/cm^2 and 72.6%, respectively, at room temperature. The quantum dot laser emission was butt-joint coupled into silicon photonics waveguides by aligning the laser and silicon photonics chips with two translation stages. Due to the optical feedback from the air/Si interface to the laser cavity, the laser power self-pulsation and reduced threshold current density were observed. And the effective facet reflectivity, R_{eff}, of 62.7% is fitted. Furthermore, the silicon photonics waveguides interface was coated with the SiO_2/TiO_2 antireflection (AR) coating layers, and no laser performance interference is observed owing the reduced optical feedback.

6.1 Introduction

As one of the most promising alternatives to electronic interconnects, silicon photonics have been studied intensively, and nearly all of the components of silicon photonic interconnects have been individually demonstrated.[14, 68-71] While the performance of these devices are now competitive with electronic-only interconnects and almost reach their theoretical limits, there still remain significant challenges to the realization of a complete integration of III-V lasers with silicon photonics components Several different approaches have been taken to integrate III-V lasers into the silicon photonic platform.[2, 126-130] Among them, butt-joint coupling between the active III-V lasers and gain chips with passive silicon photonics components have drawn large attention recently due to the simplicity and high coupling efficiency, thus, it has been demonstrated that the silicon photonics integration can be effectively achieved by the butt-joint coupling of III-V quantum well (QW) and (quantum dot) gain chips and lasers with silicon photonics distributed Bragg reflectors (DBRs), modulators and waveguides and they have shown promising results to achieve the optical interconnections.[129-135] However, in the butt-joint coupling schematics, due to the presence of air gap between the laser output facet and waveguide input, there will be optical reflection at the laser facet/air and waveguide/air interface to provide optical feedbacks to the laser cavities, which can significantly affect the laser stability and performances. [136-139]These issues have been intensively investigated in the telecommunication industries when coupling laser devices with other optoelectronics components, however, little attentions in this regards have yet been made in the silicon photonics integrations. Thus, in the section, we present experimental and

theoretical investigation of the effect of the laser performance due to the additional optical feedbacks.

6.2 Experiments

In our experiments, high performance InAs quantum dot (QD) lasers were butt-joint coupled with silicon photonics waveguides and the QD lasers were characterized by light-current (L-I) and electroluminescence (EL) measurements. Furthermore, the SiO2/TiO2 antireflection (AR) coating structures at the silicon photonics import facet were deposit to reduce the optical feedback and the laser characteristics were systematically measured and compared. We employed InAs QD lasers as our active components due to their high temperature stability, which make it ideal candidate for silicon photonics integrations. In addition, a transfer matrix method (TMM) model was developed to model the optical feedback in Fabry-Pérot laser cavities and the corresponding effect on the laser characteristics.

6.2.1 InAs Quantum dot (QD) Laser

InAs quantum dot (QD) laser heterostructures were grown on (001) GaAs substrates in a Veeco GEN II molecular beam epitaxy (MBE) system. The active region contains 7 stacks of InAs QD layers. The details of the InAs QD laser growth and characterization have been reported elsewhere.[107] Ridge waveguide lasers were fabricated by standard photolithography, inductively coupled plasma-reactive ion etching (ICP-RIE), contact metallization, and cleaving techniques, where the waveguide width and

the cavity length were 5 μm and 1500 mm, respectively. All the laser devices reported in this article were measured with the waveguide facets un-coated (as-cleaved).

6.2.2 SOI silicon waveguide

A silicon single mode waveguide was fabricated on silicon-on-insulator (SOI) wafers by electron beam lithography and reactive ion etching. The silicon photonics waveguide has the width and height of 400 nm and 250 nm, respectively, to maintain single mode propagation for the 1.3 μm laser emission. The waveguide length of 4 mm was defined by cleaving, after which the waveguide facets were mechanically polished to reduce the facet scattering loss. In order to further reduce waveguide propagation loss, the SOI waveguide was cover with 1.2 um SiO_2 top cladding layers deposit by plasma enhanced chemical vapor deposition (PECVD) techniques. Finally, at the input port of the silicon waveguide, an inverted taper structure was designed and fabricated as the mode converter to enhance the coupling efficiency, where the waveguide was inverted tapered from 150 nm to 400 nm in a distance of 300 um.

6.2.3 Butt-joint coupling

After the device fabrication, the QD laser bars were mount on a thermoelectric cooler (TEC) with p-side up to keep the laser device temperature at 25 ˚C during operation, and the silicon photonics chips were placed on a 6-axis translation stage for active alignment. Figure 6-1 and inset illustrate the schematics and micrograph image of the experimental setup, respectively, where, the micrograph image shows the section of the butt-joint coupling between QD lasers and silicon photonics waveguides. The anode and

cathode electrodes of the QD lasers were probed by high precision Cascade Microtech probe micro-positioners to supply the bias current. The alignment procedure was monitored by a near InGaAs Infrared (NIR) camera and Ge power meter. During the alignment process, the QD laser was biased at a fixed current of 80 mA at continuous-wave (c-w) operation, and the bias current is corresponding to 2 $J_{th,}$ where the J_{th} (40 mA) is obtained from a separate light-current (L-I) measurement with the same standalone QD lasers. Two identical Ge integrating sphere power meters were placed at the output port of the silicon photonics waveguide and rear facet of the QD lasers to measure the optical power. During the alignment process, the Si waveguide output power was maximized by adjusting the position of the silicon photonics waveguides. The entire coupling process was monitored by an InGaAs camera as well. After successfully coupling the QD laser into the silicon photonics waveguides, the laser light current (L-I) characterizations were measured from the laser rear facet.

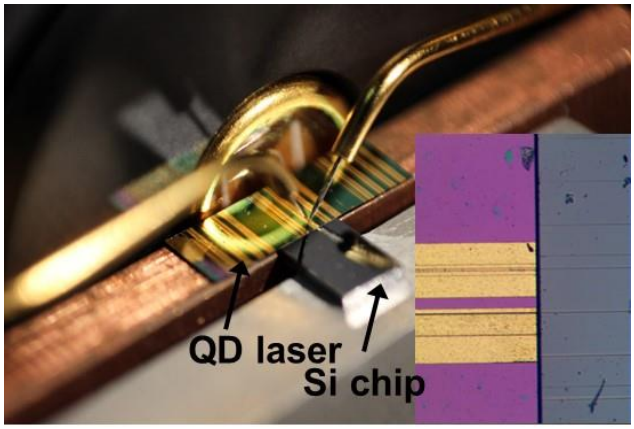

Figure 6-1 Schematics and micrograph image (inset) of the Si waveguide and QD laser butt joint couple experimental setup

6.3 Butt-joint couple characterization

Figure 6-2a illustrates the L-I characteristics, measured from the laser rear facet, of the QD laser coupled with silicon photonics waveguides. In this measurement, a QD laser with the cavity length and ridge waveguide width of 2 mm and 5 um, respectively, was employed. In comparison, the dotted line in Fig.7-2a shows the L-I curve of the same laser diode without butt-joint coupled silicon photonics waveguides. The inset of Figure 6-2a shows a NIR micrograph image of the silicon photonics waveguide coupled with the QD laser emission, where a bright line in the Si waveguide was observed. It is found that the butt-joint coupling between the QD lasers and Si waveguide is playing a significant role in the laser performances. The threshold current density is reduced from 455 A/cm^2 to 435 A/cm^2 compared to uncoupled QD lasers, in addition, when the laser is coupled with silicon photonics waveguide the output power oscillation is also observed. Figure 6- 2b illustrates the power self-pulsing vs. time, this is a signature feature when a Fabry-Perot diode lasers are exposed to optical feedback to the laser cavity. [139, 140]Despite of small threshold current density change, the inherit power self-pulsing and laser instability can be potentially detrimental. Finally, in order to reduce the Si/Air reflectance and optical feedback in the laser cavity, the silicon waveguide input facets was deposited with an antireflection coating (ARC) consisting of one pair of SiO2/TiO2 with the thickness of 215 nm and 125 nm, respectively. The reflectivity is reduced to < 2% in the wavelength window from 1.1 μm to 1.3 μm. As a results, when the Si/air reflection is reduced, almost identical L-I characteristics is obtained implying the unaltered laser characteristics coupled with Si waveguides.

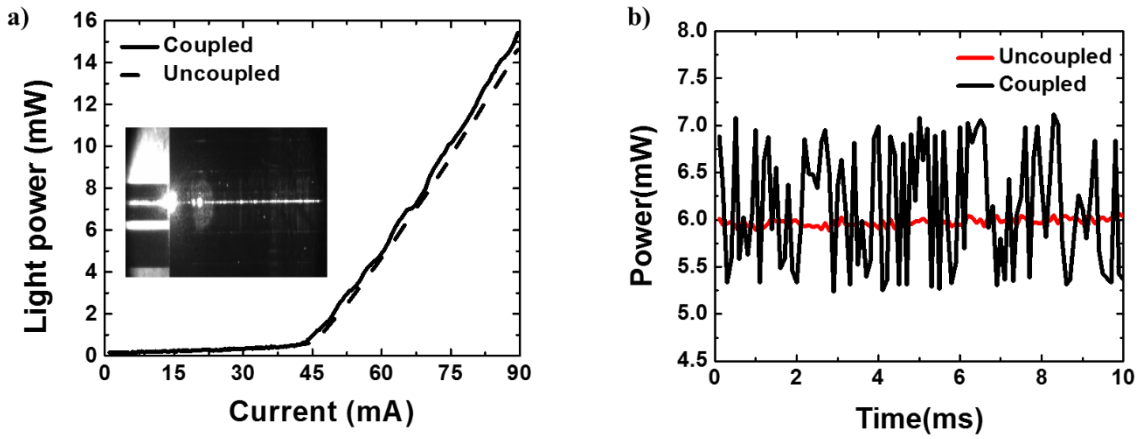

Figure 6-2: (a) L-I characteristics of butt-joint coupled (solid line) and uncoupled (dashed line) QD lasers, where a reduced threshold current from 455 A/cm2 to 435 A/cm2 compared to uncoupled QD lasers is observed; (b) Laser output power vs. time characteristics of uncoupled (red) and coupled (black) lasers, where a laser output power self-pulsing is measured from the coupled QD lasers.

6.4 Optical feedback by transfer matrix method

Furthermore, a one dimensional three-mirror cavity is developed by transfer matrix method (TMM) to describe the QD laser cavity with optical feedback from silicon photonics interface. Figure 6-3 illustrate the equivalent cavity model, where the r_1, r_2 and r_{ext} are the electric field reflectivity at the diode laser, rear face, coupling front facet and silicon waveguide import facet, respectively, and L and d are the diode laser cavity length and spacing between the laser output facet and silicon waveguide interface. The r_{eff} represents the equivalent electric field reflectivity by considering both the r_2 and r_{ext}.

From the TMM, the $r_{eff} = |r_{eff}| \cdot e^{-j\varphi_r} = r_2 \cdot (1 + k_{ext}\cos(2\pi\nu\tau_{ext})) \cdot$

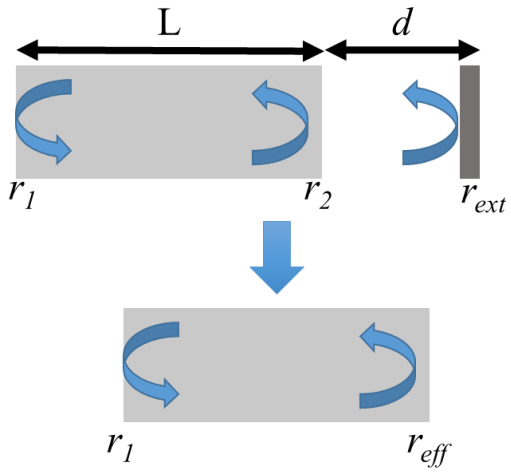

Figure 6-3 The schematic model of optical feedback from the silicon photonics interface and equivalent cavity model, which considered all the reflections on butt joint, coupled side as one effective reflectivity.

$e^{-j(1+k_{ext}sin(2\pi\nu\tau_{ext})}$, where ν is the emission frequency, $k_{ext} = \frac{r_{ext}}{r_2}(1 - r_2^2)$, r_{ext} is the light traveling time in the air space between r_2 and r_{ext} where $r_{ext} = \frac{2d}{c}$ and c the speed

of light. In a laser diode, the threshold gain $g_{th} = \alpha_i + \frac{1}{L}\ln(\frac{1}{r_1 r_2})$, where the α_i is the internal loss, L is the cavity length and r_1 and r_2 are electric field reflectivity. Thus, after introducing the external feedback and r_{eff}, the threshold gain change can be described, $\Delta g_{th} = \frac{1}{L}\ln(\frac{r_{eff}}{r_2})$. It is found that the laser threshold current and threshold gain are modulated by with the external cavity, which agrees well with our experimental observation as shown in Figure 6-2. In addition, the laser threshold current density is written as following

$$J_{th} = J_{tr} + \frac{\alpha_i}{A} + \frac{1}{2AL}\ln\left(\frac{1}{R_1 R_2}\right) \qquad (1)$$

where the Jtr is the transparency threshold current density, A is a material constant and R is the facet reflectivity, R=r2. Since Jtr and A are materials and structure constants and independent of cavity optical feedback. Figure 6-4b illustrates the laser threshold current density Jth and differential quantum efficiency ηd vs. cavity length, where the same laser diodes without optical feedback are utilized for simplicity. In addition, the internal loss α_i can be fitted by $\eta_d^{-1} = \eta_i^{-1}(1 + \frac{\alpha_i L}{\ln(\frac{1}{R1R2})})$, where η_d and η_i are differential quantum efficiency and internal quantum efficiency, respectively. As a result, Jtr of 446.8 A/cm2 and α_i of 1.37 cm-1 are obtained from the fitting. Finally, the Reff of 62.7% is calculated after plug the fitted Jtr and A (0.092) and measured J_{th} into equation 1.

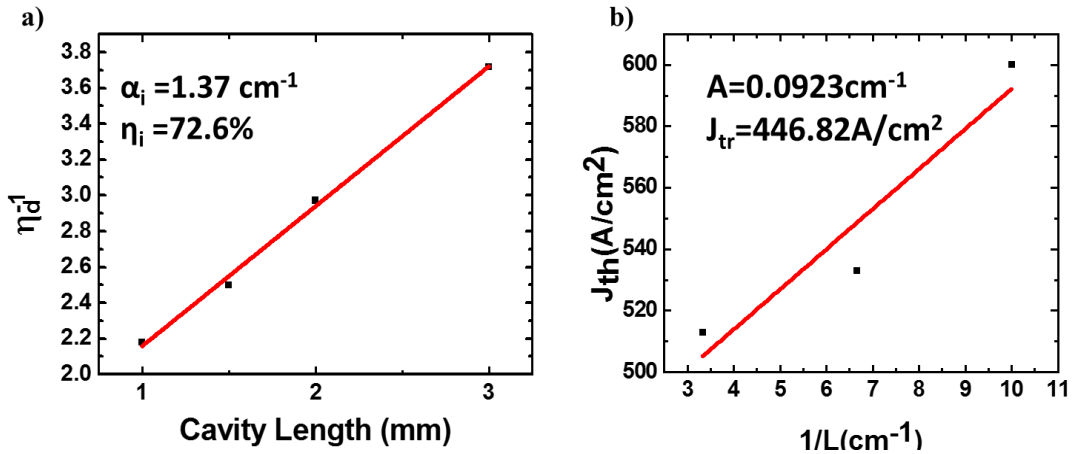

Figure 6-4 (a) Reciprocal differential efficiency η^{-1} vs. cavity length L; (b) Laser threshold current density J_{th} and vs. Reciprocal of cavity length

6.5 Conclusion

In conclusion, InAs QD lasers have successfully butt-joint coupled with silicon photonics waveguides by aligning the two chip by high precision translation stages. The optical feedback from the silicon photonics interface has been investigated both theoretically and experimentally, the laser threshold current density reduction and emission power self-pulsing were observed. Finally, the ARC layers were applied at the silicon photonics interface, and the laser characteristics stabilization was measured. It is argued that this work can provide valuable information for future silicon photonics integration.

7 INAS QUANTUM DOT LASERS WITH DRY ETCHED FACET BY BR-ION BEAM-ASSISTED ETCHING

The etching conditions of the AlGaAs materials in bromine ion beam-assisted etching (Br-IBAE) process have been determined. The etching rates can be varied from several nm/min to ~300 nm/min through controlling the bromine pressure and the substrate temperature. High-performance InAs quantum dot (QD) lasers have been grown by molecular beam epitaxy system. The broad area QD lasers are fabricated by standard photolithography and metallization processes, while the laser facets are formed by Br-IBAE dry etching process. With the dry-etched facets, the InAs QD lasers have a threshold current density J_{th}, and slope efficiency, η_i of 480 A/cm^2 and 34%, respectively. The Br-IBAE dry etched facet reflectivity of 0.28 is obtained from fitting the J_{th} versus reciprocal cavity length curves.

7.1 Introduction

Semiconductor laser diodes with dry-etched facets are of long interests for photonic integrated circuits (PICs) [141, 142]. With the recent development of silicon photonics research, such laser devices are ideal candidates for on-chip silicon photonics integrations as well [143]. In addition, the laser diodes fabricated with dry-etched facets also exhibit the ability to precisely control the laser position and dimension and are also of significance for fast and on-chip device testing to improve the photonics devices manufacturing throughput [144]. In this section, in addition to the traditional induce coupled plasma (ICP) dry-etching process which still can't provide reliable etching results for III-V lasers, both Bromine and Chlorine based ion beam assisted etching (IBAE) processes have shown success to be a versatile tool for etching laser facets in the GaAs and InP material systems [144]. However, due to the high aluminum contents in the AlGaAs materials, the etching conditions of AlGaAs materials are expected to be different compared to their GaAs counterparts and there have been lack of study of the IBAE etching conditions for AlGaAs materials [145]. Furthermore, in the applications of Silicon photonics integrations, it is important to have lasers that are robust against temperature variations. In this context, the InAs quantum dot (QD) lasers are attractive candidates due to their suitability for high temperature operation [26, 114, 146]. However, the high performance InAs QD lasers with dry etched facets have not been widely investigated [143, 147]. In this context, we report the investigation of the Br-IBAE etching process for the $Al_{0.4}Ga_{0.6}As$ materials and high performance InAs QD lasers with dry-etched facets. In this study, we choose to employ the Bromine as the etching chemicals in the IBAE etching process

instead of the Chlorine. This arises from its inability to etch vertical sidewalls in GaAs heterostructures with Cl_2-IBAE [148, 149].

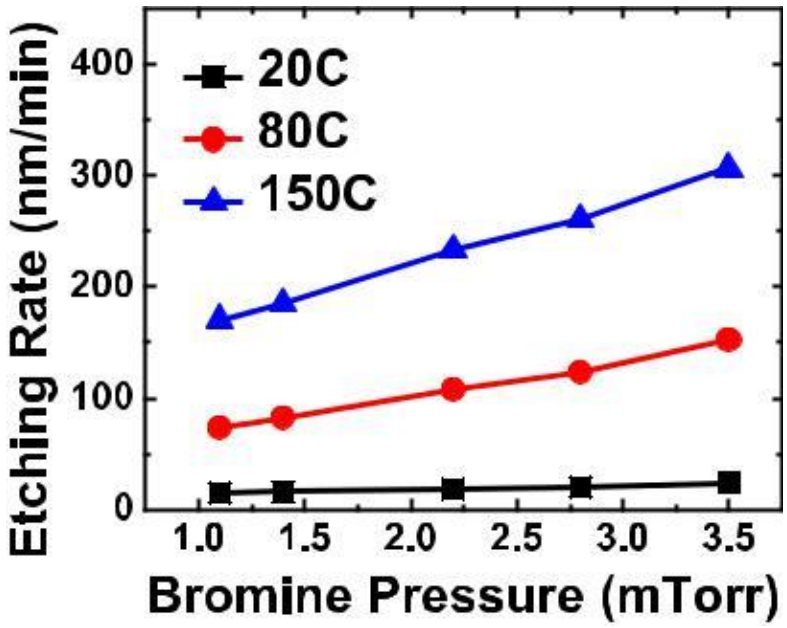

Figure 7-1 Etching rate vs. substrate temperature and Bromine pressure.

7.2 Br-IBAE Etching of $Al_x Ga_{1-x} As$

The $Al_{0.4}Ga_{0.6}As$ etching calibration samples with the thickness of 1.8 μm are grown by a Veeco molecular beam epitaxy (MBE) system on (100) GaAs substrates and a 10 nm GaAs capping layer is grown to prevent the oxidation of Aluminum contents when exposed to air. Here the Al content of 40% and 1.8 μm thickness of AlGaAs film is chosen to be identical to ones in the QD laser cladding layers. In this study, the SPR220-3.0 photoresist is used as the etching mask. The etching process is performed in a customized Br-IBAE system. The system has a load lock chamber and background pressure of 6×10^{-7}

Torr in the process chamber. Once the sample is loaded in the process chamber, the ion gauge is shut off, Ar flow rate of 3 sccm is established. The beam voltage is set and the beam current is adjusted until the current, measured by a Faraday cup, is at the proper value. The Faraday cup also serves as a shutter for the Ar and Br_2 beams. Once the Ar beam current is established and then neutralized, the sample is *in-situ* cleaned at room temperature using a 5 min, 40 A/cm^2, 600 V Ar beam sputter conditions. The substrate temperatures between 20 and 220 °C can be achieved in the customized Br-IBAE system. Figure 7-1 illustrates the etching rate vs. sub-strate temperature and bromine pressure, it is the found that, unlike etching GaAs [148], the $Al_{0.4}Ga_{0.6}As$ etching process can only exhibit reasonable etching rate at elevated substrate temperatures and, at the substrate temperature of 80 °C, an etching rate of 100 nm/min can be obtained with the Bromine pressure of 2.8 mTorr.

7.3 Quantum dot lasers with dry-etched facets

The InAs quantum dot laser heterostruc-tures grown on (100) GaAs substrates in the Veeco MBE system. The active region contains 7 stacks of InAs QD layers. Each layer consists of 2.6 monolayer (ML) InAs QDs grown at 500 °C at the growth rate of 0.1 ML/s. The p-type and n-type doped $Al_{0.4}Ga_{0.6}As$ cladding layers are designed to confine the QD emissions in the III-V waveguides. The broad area QD lasers are fabricated by standard photolithography, wet chemical etching, and contact metallization processes, where the waveguide width is 30 μm and the cavity length is varied from 1000 – 2000 mm. In the broad area lasers, one facet is achieved by the Br-IBAE etching process with the SPR220-3.0 photoresist as the etching mask and the laser output emission is measured from the

other un-coated as-cleaved facet. In the IBAE facet etching process, the substrate temperature and Bromine pressure of 80 °C and 2.8 mTorr are employed, respectively, which have resulted in the best laser performance among other combination in this study. In comparison, the QD lasers with both as-cleaved facets are fabricated with the same epitaxy wafers and device dimensions. The electrical characteristics of the QD lasers are measured with a modified probe station, where the samples are loaded with n-side up on a thermoelectric cooler (TEC) stage and the device temperature is precisely controlled and can be varied from 10 to 100 °C during the measurements.

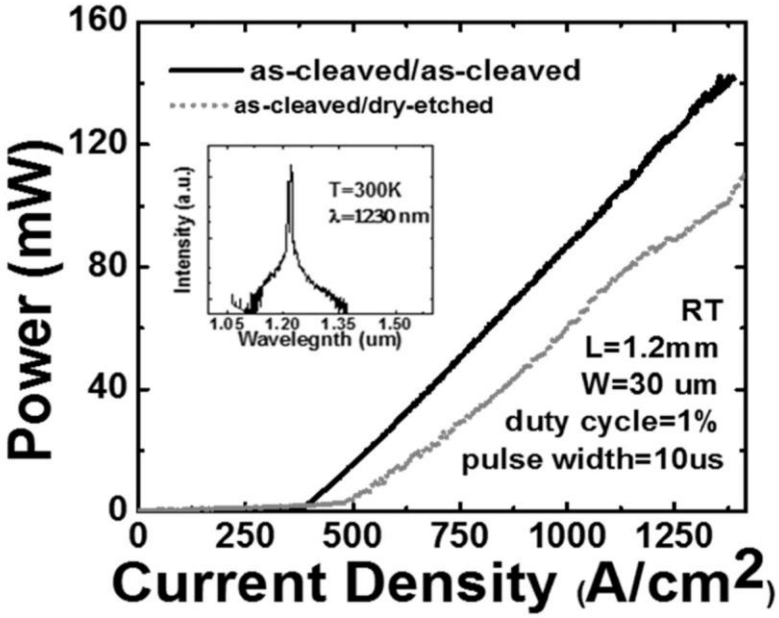

Figure 7-2 Light-current (L-I) characteristics of a QD laser with the cavity length and waveguide width of 1.2 mm and 30 μm, respectively, and dry-etched/as-cleaved facets (solid) and as-cleaved/as-cleaved facets (dash); inset: electroluminescent spectrum of QD laser.

Figure 7-2 shows the light-current (L-I) characteristic of a QD laser with the dry-etched/as-cleaved facets and cavity length and waveguide width of 1.2 mm and 30 μm, respectively. To eliminate the Joule heating effects, the L-I characteristics are measured under pulsed current injection conditions with the pulse width and duty cycle of 10 μs and 1%, respectively. The threshold current density, J_{th}, and slope efficiency, η_d, of 480 A/cm^2 and 34%, respectively, are obtained from the L-I characteristics. In comparison, the dashed gray curve in Figure 7-3b illustrates the L-I characteristic of a QD laser with the same dimensions and both as-cleaved facets. In the lasers with both as-cleaved facets, the threshold current density, J_{th}, and slope efficiency, η, of 320 A/cm^2 and 38%, respectively, are measured. Most notably, the QDs lasers exhibit state-of-the-art threshold current density and output power characteristics and the lasers with dry-etched facets shows limited performance degradation due to the larger mirror loss compared to the QD lasers with as-cleaved mirrors. The reflectivity of the dry-etched laser facet is estimated by using the equation [9]:

$$J_{th}(L) = J_{th}(\infty) + \frac{C}{2L}\ln\left(\frac{1}{R_1 R_2}\right)$$

where J_{th} is the threshold current density, L is laser cavity length, R_1 and R_2 are the mirror reflectivity, and C and $J_{th}(\infty)$ are constants extracted from laser diodes with cleaved facets.

Figure 7-3a illustrates the plot of J_{th} vs. reciprocal cavity length (*1/L*), and the mirror reflectivity R of the dry-etched facet of 0.28 is obtained from the fitting, given that the reflectivity R of the other as-cleaved facet is 0.32. The IBAE etched mirror reflectivity R

is comparable with the one measured from other dry etching techniques, in the range of 0.28 to 0.33, such as focus ion beam (FIB) and inductively coupled plasma (ICP) dry etching techniques for InP and GaAs based materials [150-153]. It is worth noting that, even though the IBAE etching technique doesn't offer significant advantage of the mirror reflectivity, it is still of great interests for photonics integration due to its versatile capability for device fabrica-tions [4]. The fitted $J_{th}(\infty)$ of 140 A/cm^2 of the dry-etched lasers agrees well with the one fitted from the as-cleaved laser devices, 108 A/cm^2, implying that the device characteristics disparity between the ones with as-cleaved and dry-etched facets is majorly due to the different mirror loss. Finally, Figure 7-3b shows the measured temperature dependence of threshold current density, J_{th}, and slope efficiency, η_d , of a typical laser with cleaved/dry-etched facets under pulsed bias emitting at λ = 1.23 μm (inset). The threshold current density of the lasers is slightly high due to the dry-etched facet and p-doping, which can increase Auger recombination [154]. The value of T_0 is fitted from $J_{th}(T) = J_{th}(0) \cdot \exp(T/T_0)$ [155], which is 110 K in the range 60 °C < T ≤ 100 °C. The high value of T_0 measured in this temperature range shows that QD lasers with dry-etched facets are ideal candidates for high temperature operations [156]. Similarly, the value of T_1, given by $\eta_d(T) = \eta_d(0) \cdot \exp(-T/T_1)$ where η_d is the differential efficiency [155], is 105 K in the range of 60 °C < T ≤ 100 °C.

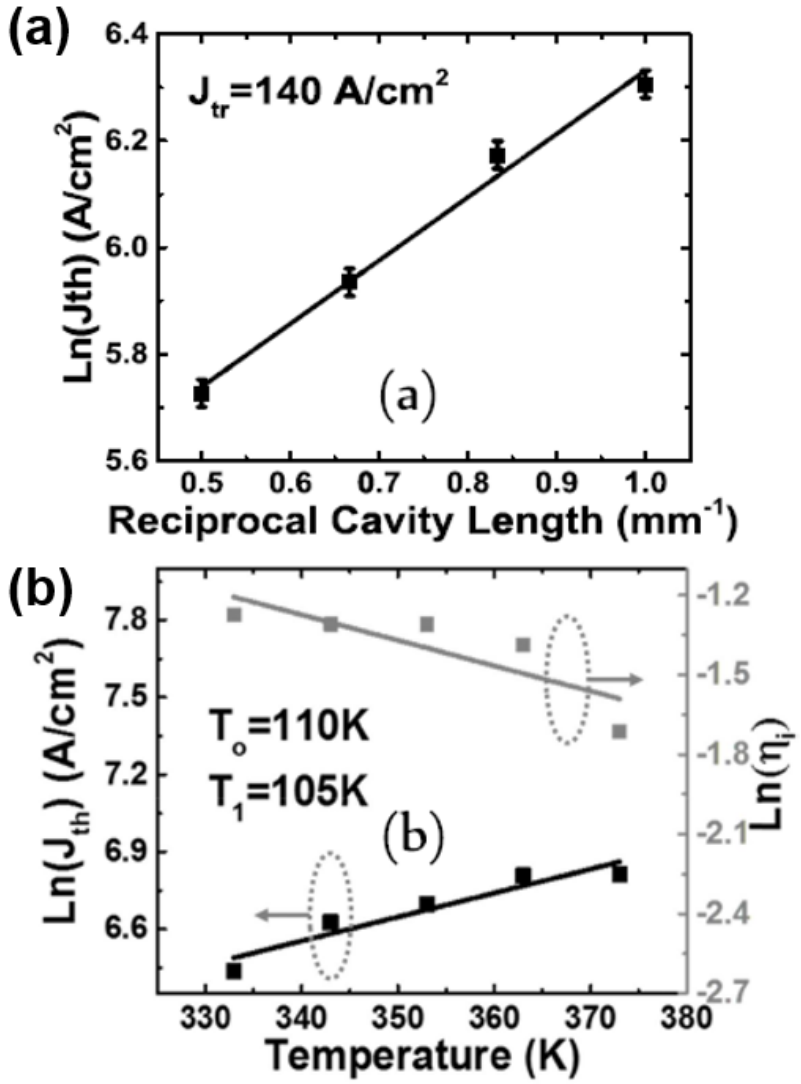

Figure 7-3(a) Plot of threshold current density (J_{th}) vs. reciprocal cavity length (1/L), and the mirror reflectivity R of the dry-etched fact of 0.28 is obtained; (b) Temperature dependence of threshold current density, J_{th}, (solid) and slope efficiency, η_d, (dash) of a typical QD laser with cleaved/dry-etched facets under pulsed bias operation.

7.4 Conclusion

We have demonstrated the Br-IBAE etching conditions of MBE grown $Al_{0.4}Ga_{0.6}As$ materials that are suitable for GaAs based dry-etched laser fabrications. The

etching rate of 100 nm/min for $Al_{0.4}Ga_{0.6}As$ is obtained at 80 °C. Furthermore, we have shown the fabrication and performance characteristics of a high performance 1.3 μm QD laser with dry-etched laser facet. A high degree of temperature stability is exhibited by the QD lasers.

8 BUTT-JOINT HETEROGENEOUS INTEGRATION PLATFORM BY PD-GAAS WAFER BONDING

As discussed in the above section, we have demonstrated a hybrid InAs QD laser by GaAs-Si wafer bonding technology. However, to further hybrid integration of the laser source with a silicon photonic integrated circuit (PIC), a CMOS compatible, high tolerance, high coupling efficiency, temperature insensitive platform needs to be developed. Here, a review of other integrated platforms will be discussed and a new platform will be proposed in which the low temperature Pd-GaAs bonding technology can be used to realize a butt-joint hybrid integration configuration. As an example, a hybrid tunable laser is proposed based on this platform. The details of simulation and layout are discussed and a proof of concept experiment was demonstrated by using a booster optical amplifier (BOA) externally fiber coupled to a silicon nitride ring resonator photonic integrated chip. A tunable laser is achieved with a 50mA threshold current, 35dB side mode suppression ratio (SMSR) and a 0.023nm/˚C thermal tuning coefficient.

8.1 Introduction

Currently, laser source integration platforms can be categorized in three regimes, fiber-to-chip integration, hybrid flip-chip integration, and hybrid monolithic integration as shown in Figure 8-1(a)-(c). The first solution could be treated as an advanced compact packaging approach (Figure 8-1a). A triangular groove or a U-shaped groove is created in the silicon photonic chip aligned with waveguide taper such that fiber can be effectively coupled to the waveguide by either passive or active alignment. IBM is one of leaders developing this platform, demonstrating fiber arrays successfully coupled to waveguide arrays with high efficiency (<1.3dB) [5]. IBM has also demonstrated mechanically compliant polymer waveguides coupled to silicon photonic chips under this regime. Quite different from the directly butt-coupled fiber arrays, the polymer waveguides are adiabatically coupled to the silicon waveguide, enabling mechanical coupling between the fiber connector and the chip.

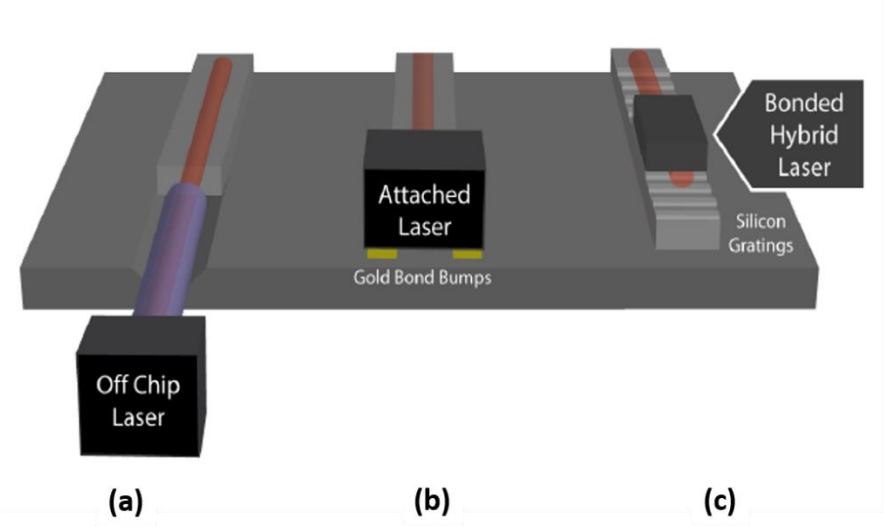

Figure 8-1 Three methods to integrate laser source to a photonic integrated circuit on silicon to form a hybrid laser: (a) fiber-to-chip integration, (b) flip-chip bonding, and (c) hybrid monolithic integration.[6]

The second approach is achieved by flip-chip bonding in which a prefabricated diode laser was aligned with the silicon waveguide during the bonding process. The state of the art results of the flip-chip bonding platform have been demonstrated by two different methods: backside alignment and self-aligned bump bonding [4, 5, 157]. As shown in Figure 8-2 a, this hybrid flip-chip bonded QD laser source was demonstrated by Arakawa el al. [4]. In this configuration, the laser arrays, as well as silicon photonic chip with etched trenches, were prefabricated and a flip-chip bonding process was later applied by using IR backside alignment with the pre-deposited alignment marks on each side. The other approach was demonstrate by IBM and Johnathan's group by using self-aligned bump bonding technology which has been used in traditional IC packaging for decades and has the potential to achieve sub-micron alignment accuracy. Compared to the first approach, this flip-chip bonding integration method shrinks the footprint of integrated lasers while

increaseing the complexity of alignment and the prefabricated workflow, limiting the fabrication flexibility when compared to the bottom-up integration platform.

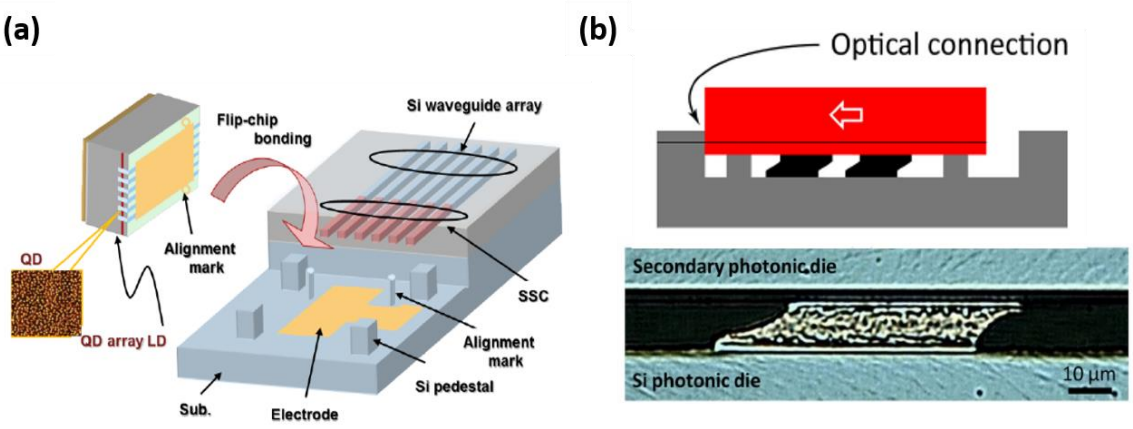

Figure 8-2 Flip-chip bonding laser source sehmatics of a)back side alignment and b) self-aligned bump bonding.[4, 5]

The third approach uses the III-V material as a gain medium that is evanescently coupled to the silicon substrate (Figure 8-3a). The laser cavity is formed by creating reflection gratings or rings on the silicon photonic circuit. This approach was first demonstrated by John Bower's group, and several PICs were later demonstrated based on this platform, such as mode-locked evanescent lasers, hybrid tunable lasers and uncooled datacom WDM hybrid laser arrays [158, 159]. This evanescent hybrid laser was further optimized by using adiabatic coupling as shown in Figure 8-3b. Different from the evanescently coupled laser, the spontaneous emission optical mode was completely confined within the III\V (quantum well) layer in this configuration. The optical mode was coupled to the silicon waveguide only at the two ends of the III\V gain region, enhancing the quantum efficiency due to the higher confinement factor in the gain region when compared with the evanescently coupled lasers[5, 160]. This laser integration approach has

a small foot-print and is very promising for silicon photonic integration as it is without the difficult alignment steps of the other two approaches discussed above. The direct bonding process is quite critical as a single particle on either side of the wafer may lead to unsuccessful bonding. In addition, both III\V-oxide bonding and BCB adhesive bonding have poor heat dissipation which influences laser performance during high temperature (80˚C) operation. To optimize the thermal performance of these oxide bonded lasers, further processing was needed to add thermal shunts via deep etching and thick metal plating, increasing the cost and complexity of devices.

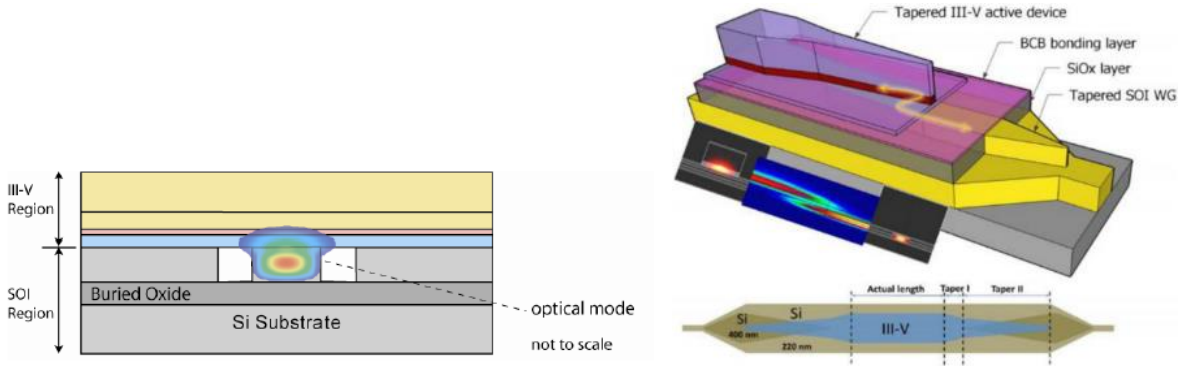

Figure 8-3 Shematic of a) a silicon evanescent laser and b) a adiabatic III-V/Si laser integration platform.[1-3]

8.2 Butt-joint heterogeneous integration platform by Pd-GaAs wafer bonding

In section 8.1, three laser source integration platforms were introduced. The fiber-to-chip coupling scheme has higher tolerance but also has a larger footprint compared to the others. The flip-chip bonding approach requires precise backside alignment during the integration process and also has limited flexibility in the laser design after bonding to the

PICs. The last approach, the evanescently coupled wafer bonding platform has a small footprint as well as CMOS compatible bottom-up fabrication flow. However, it may suffer

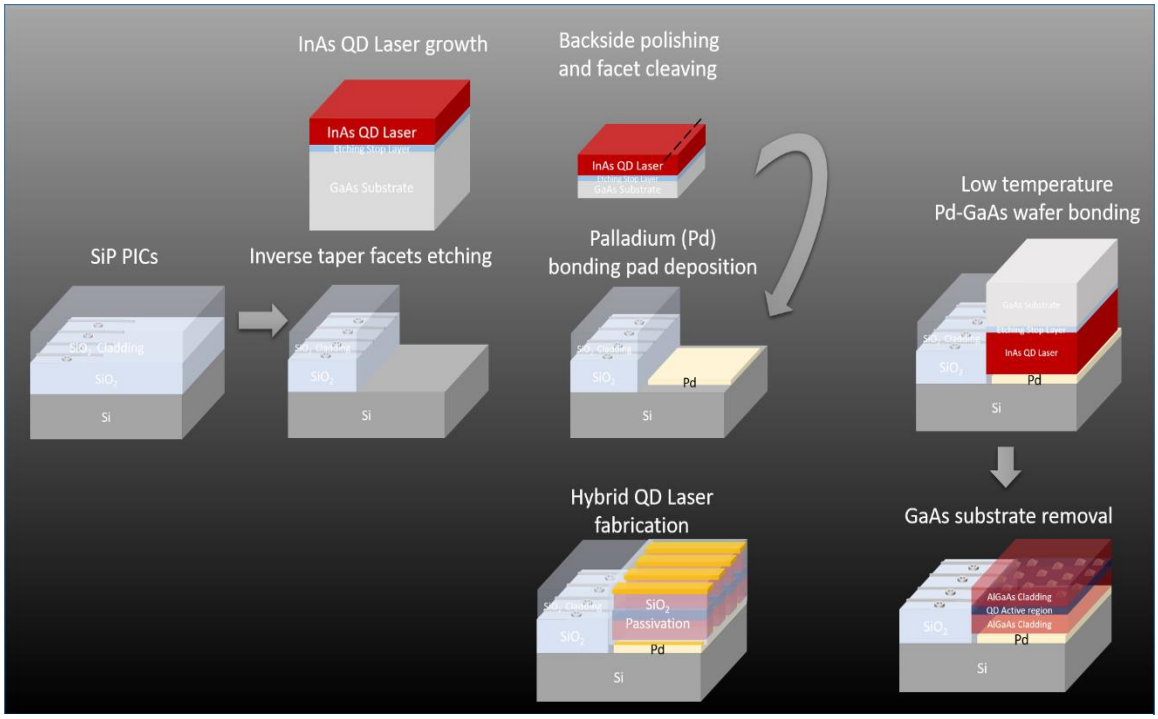

Figure 8-4 Fabrication flow of butt-joint heterogeneous integration platform by Pd-GaAs wafer bonding

from low coupling efficiency and poor thermal dissipation properties.

Here, we propose an integration platform based on the demonstrated low temperature Pd-GaAs wafer bonding technology. The process flow is shown in Figure 8-4. Before bonding, the InAs quantum dot epitaxial wafer and silicon photonic integrated circuits are individually prepared. The InAs QD laser epitaxial wafer is grown by MBE with a sacrificial etching stop layer underneath the generic QD laser structure. The wafer is then mechanically polished down to ~120 um for cleaving. One side of laser facet is cleaved and an anti-reflection coating is applied by using E-beam evaporation to reduce

the feedback reflection from the silicon photonic waveguide taper. The silicon photonic integrated circuit (SiPIC) chip is made by standard processing techniques, such as e-beam lithography, dry etching and oxide cladding on an SOI wafer. After that, the silicon waveguides on the side to be coupled to the integrated lasers are etched down to the silicon substrate. The etched area is then coated with a Pd film for low temperature wafer bonding, specifically, the cleaved facet side of laser epitaxy wafer is pushed against the etched SiP waveguide. In the end, the GaAs substrate of the InAs laser epitaxy is removed, and laser devices are made by standard laser fabrication techniques. The flip-chip bonding process is similar to the second approach discussed in section 8.1, however, no active alignment is required during the bonding process. To control the thickness of the bonding metal, a two-step oxide etching method can be used. The first etched trench in the oxide defines the height to align the laser's active region with silicon waveguide tapers while the second etch will remove the whole cladding oxide with the exception of some height control pedestals that have been masked by photoresist. The Pd bonding film will be deposited in the middle of the pedestals and exceed the thickness of pedestal by a small amount. As a result, the active region of QD lasers could be passively aligned and well controlled by these pedestals. A schematic drawing of a butt-joint heterogeneous QD laser chip integrated by Pd-GaAs wafer bonding is shown in Figure 8-5.

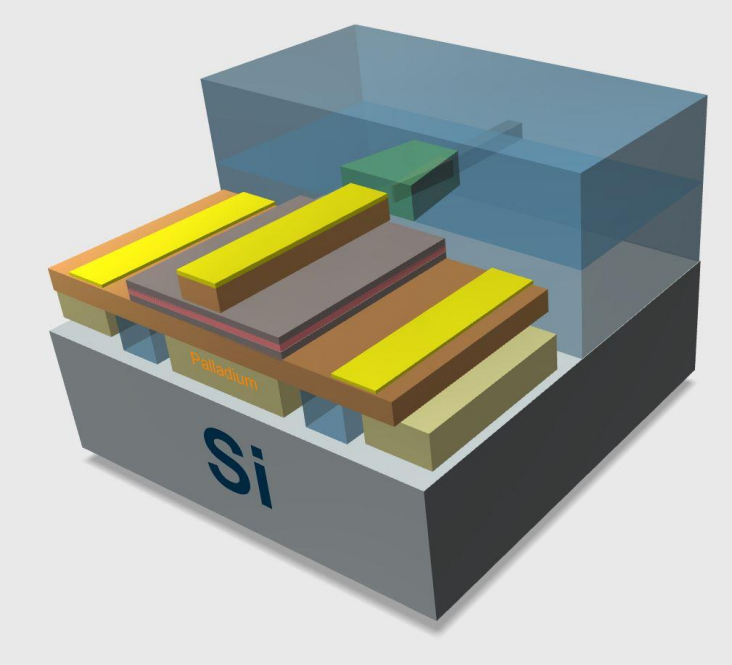

Figure 8-5 Butt-joint heterogeneous integration platform by Pd-GaAs wafer bonding

In table 8.1, different laser source integration configurations are compared from perspectives of integration density, fabrication complexity, and coupling efficiency. Since the mode size can be well controlled on both the laser and the silicon waveguide, the butt-coupled integration regime is supposed to have a higher coupling efficiency compared with the evanescent and adiabatic coupling schemes. Due to the post fabrication of the laser or other active III/V devices, there are no limitations to large volume integration of high-density components into this platform, one of the problems faced by the flip-chip bonding

Table 8-1 Comparisons of different integration approaches

Integration Configuration	Integration density	Complexity	Coupling efficiency
Fiber to chip [8.1a]	●	●	● ● ●
Flip-chip [8.1b]	● ●	● ●	● ●
Hybrid Integration [8.1c]	● ● ●	● ● ●	●
Butt-joint heterogeneous integration [8.5]	● ● ●	● ●	● ● ●

configuration. The complexity of the proposed configuration is similar to that of the flip-chip configuration since the butt-joint coupling relies on high precision flip-chip bonding. However, it should be easier to achieve the void free bonding compare to the evanescent oxide bonding. Although the fiber coupled configuration is the simplest method of integration, the low density may limit its applications. Furthermore, this metal bonding process, with p-side down laser mounting and QD gain medium, results in an integration platform with good heat dissipation properties and temperature insensitivity.

8.3 Detailed design and simulation of butt-joint heterogeneous integration

In section 8.2, we proposed a fabrication process to achieve a high efficiency, temperature insensitive butt-joint heterogeneous integration platform by using Pd-GaAs low temperature bonding technology. However, there are several key technical approaches that need to be well investigated and will be discussed in this section.

In this butt-joint heterogeneous integration platform, the most critical specification is the coupling efficiency between the bonded laser and silicon photonic waveguide. More specifically, a highly efficient coupler on the silicon photonic chip need to be designed and simulated along with the offset distances between bonded laser and SiP waveguide before real devices can be fabricated. For the silicon photonic waveguide design, an inverse taper structure may be used as a first approach while a more advanced spot-size converter (SSC) making use of tapers in both the III\V and SOI parts is developed to realize higher coupling efficiency.

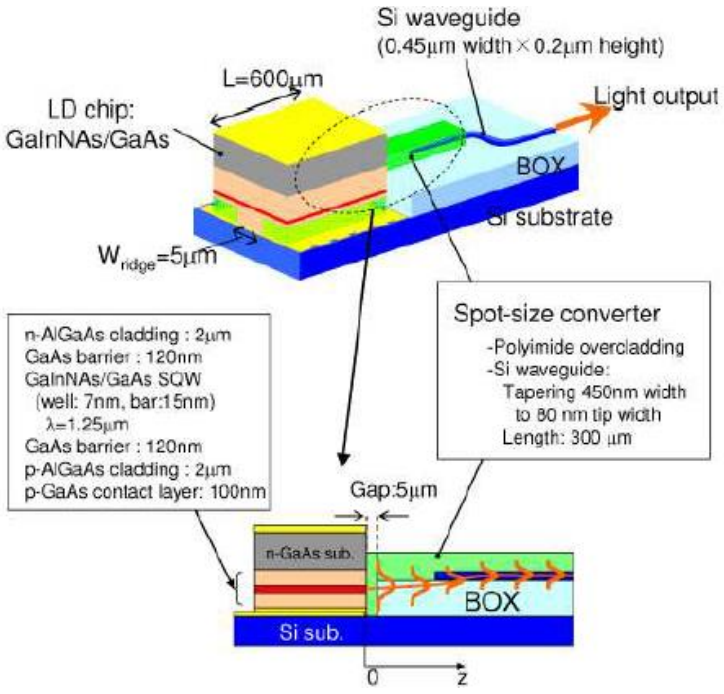

Figure 8-6 Schematic illustration of laser diode chip integrated on Si waveguide with the spot-size converter.[161]

Figure 8-6 shows the schematic of the flip-chip bonded laser integration platform demonstrated by Toshiba Corporation [161]. Although the laser made use of a quantum well and was prefabricated before bonding, the model of the SSC design is well suited to our bonding platform design. Similar simulation methods will be used to design the SSC for the Pd-Gas bonding platform according to our QD laser heterostructures. It is important to note that the Z direction alignment of the laser coupling can be well controlled by adjusting the thickness of the bonding metal while the X-Y alignment can be well defined by lithography, a more accurate alignment and cost-effective method than the flip-chip backside alignment bonding process. With this SSC design, a theoretical coupling

efficiency could of 85% can be achieved which is promising for monolithic laser source integration.

A proof of concept device is designed by using a silicon nitride on silicon structure both for the SSC and the photonic integrated circuit to leverage the fabrication complexity. A comparison of the integration specifications between Si and silicon nitride systems are listed in Table 8.2. The SiN waveguide should have lower loss and relaxed fabrication tolerance when compared to the Si waveguide. It can also transmit more power than silicon

Table 8-2 Specification of Si vs. SiN waveguide platform

	Si	SiN	Note
Spectral transparency: shortest λ (um)	1.1	0.4	Si\SiN bandgap
Spectral transparency: longest λ (um)	4	4	SiO_2 absorption
Power limitation (mW)	10's	100's	Two-photon absorption
Loss (dB/cm)	1	2-3	SiN has lower fabrication tolerance
Layer stack flexibility	limited	good	SOI made by bonding
Footprint	small	large	SiN lower Δn
High speed modulator/detector	Easy	Hard	SiN need co-integration with SOI

since two-photon absorption is less of an issue. The thickness of Si_3N_4 can be customized by using low pressure chemical vapor deposition (LPCVD), which is cheaper than silicon SOI wafers. The main downsides of the nitride waveguide are that its footprint is significantly larger than silicon due to its lower refractive index and that high speed modulators (>1GHz) cannot be achieved by the large bandgap (5 eV) passive nitride dielectric. To solve this problem, a tri-layer silicon nitride on silicon waveguide could be used to make a low loss (<2.1dB) transition between the silicon nitride and the silicon which could be co-integrated with a standard Si SOI platform as a low loss interconnect waveguide[162].

8.4 Hybrid tunable InAs QD lasers butt-joint heterogeneously integrated on a Si substrate

A heterogeneous butt-coupled integration platform is proposed above. However, the laser itself is multimode in the transverse direction. For most telecommunication and data center applications, it is more useful to build up a single mode operation laser integrated on this platform. An alternative to DFB or DBR lasers, which require submicron gratings as well as complex re-growth techniques, a silicon photonic ring reflector can be used to define the single mode operation. Several groups have demonstrated tunable lasers on silicon using external butt-coupled, flip-chip bonding and evanescently coupled platforms. [163-167] Based on their designs, we propose a hybrid tunable InAs QD laser butt-joint coupled to a silicon chip with integration enabled by our Pd-GaAs wafer bonding technology. As shown in Figure 8-7, the gain chip is a QD-RSOA instead of an FP laser such that the ring reflector can select a mode throughout a large flat optical gain. Otherwise, the ring reflector resonance needs to be thermally tuned to match up with the narrow longitudinal lasing modes, increasing power consumption. An SSC will be used in this design to minimize coupling loss and a directional coupler is included to allow for characterization of the laser performance. The ring reflector may use two different designs. Since ring resonators typically have a relatively small FSR compared to the broadband light source, the first design makes use of both a ring reflector and a distributed Bragg reflector (DBR). As is shown in Figure 8-7, the DBR can be designed to filter out a single resonant mode from the ring reflector, limiting the cavity to single mode operation. The second design uses a special ring configuration known as an adiabatic microring resonator

(AMR) which has a large FSR enabling single mode selection from the broadband gain chip without further filtering.[131]

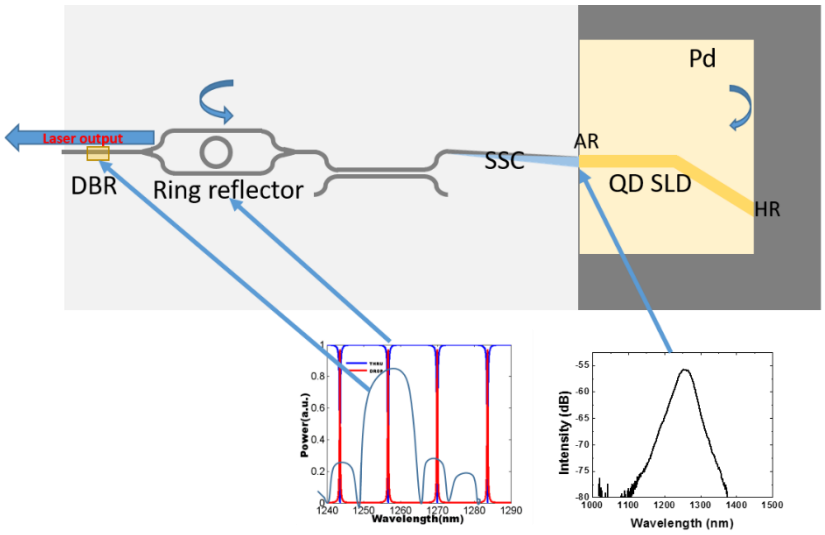

Figure 8-7 Top: Schematic of tunable QD lasers monolithically integrated on silicon by Pd-GaAs wafer bonding platform. Bottom right: the broad band QD-SLD optical spectrum. Bottom left: simulation reflection spectrum of traditional ring resonator and DBR.

8.5 Proof of concept demonstration of the hybrid tunable lasers

8.5.1 Design and simulation

A proof of concept demonstration is made by using an external booster optical amplifier (BOA) coupled to the Silicon photonic PIC as shown in Figure 8-7. The individual components including the directional coupler and multi-mode interferometer (MMI) are simulated by Lumerical Finite-Difference Time-Domain (FDTD) software. As shown in Figure 8-8a, the directional coupler is designed with a 15 um long coupling length, 800 nm gap and 150 um bend radius, respectively. Figure 8-8b shows the resulting wavelength dependent transmission response where the two output port power transmissions are 90% and 8% at wavelength of 1.3 um. In the hybrid tunable laser circuit, the majority of the power will be going through the ring reflector and laser output would be coupled out he 8% port. Figure 8-8c shows the power distribution profile of a designed

1×2 MMI which is 26.5 um long and 5.6 um wide. Figure 8-8d shows the transmission of input and two output ports which are 99%, 45.4% and 45.4% for each.

The high reflection (HR) and anti-reflection (AR) coatings of the SOA are also

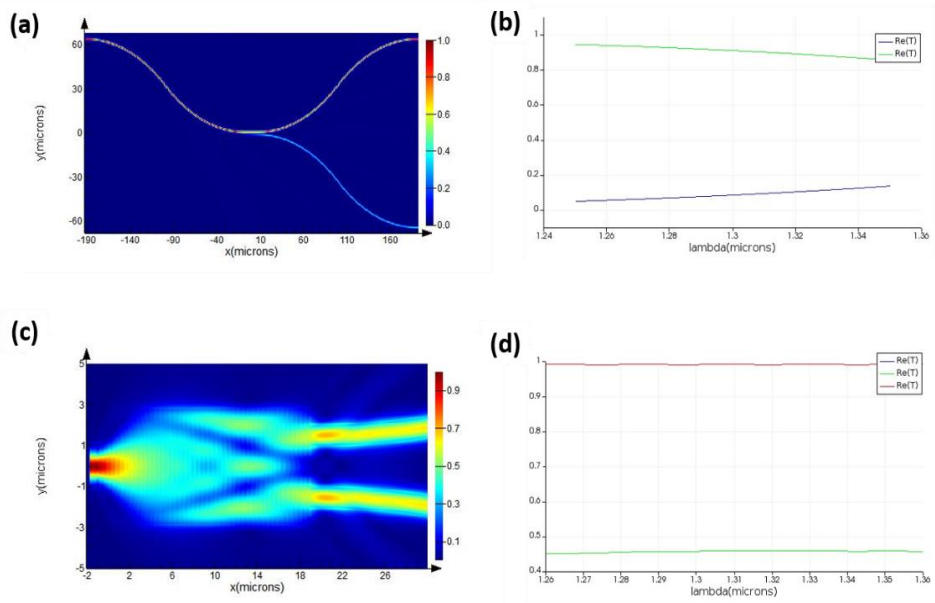

Figure 8-8 3D FDTD simulation results: (a) power distribution and (b) wavelength dependent response of directional coupler for TE mode; (c) power distribution and (d) wavelength dependent response of 1×2 multi-mode interferometer (MMI) for TE mode

simulated using the transfer matrix method (TMM). Figure 8-9 shows the resulting transmission of the HR and AR coatings which are 99% and 0.1%, respectively. The simulated HR coating structure consists of 6 pairs of SiO_2 and TiO_2 layers with thicknesses of 215nm and 126nm, respectively. The simulated AR coating structure consists of 125nm TiO_2 and 215nm SiO_2.

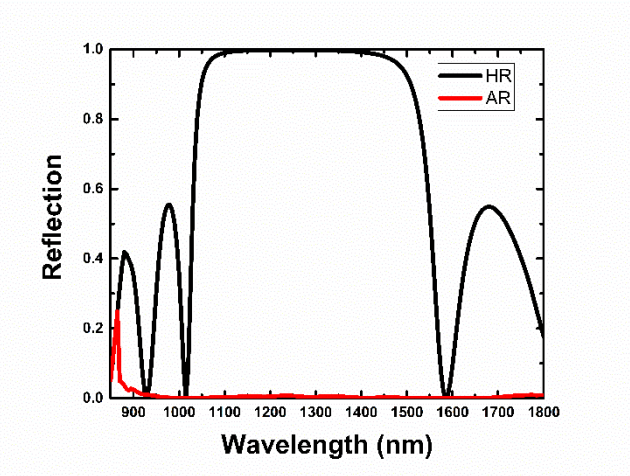

Figure 8-9 Simulation results of HR and AR SOA facet coating

The layout was designed in Tanner L-Edit with the above simulated dimensions. Although the QD gain chips are not bonded in the proof of concept experiment, the layout of the QD gain chip is designed as shown in Figure 8-10. The QD gain part has 7 degree tilted semiconductor optical amplifiers (SOA) to minimize the back reflection from the interface between QD gain and Si_3N_4 PIC. The width of SOAs are varied from 3um to 5 um. Ridge waveguide lasers are also designed to measure the coupling loss from the QD laser to straight silicon nitride waveguides with varied taper dimensions. The inverse tapers are designed with front tip sizes from 300nm to 500nm. The normal tapers front tip sizes are varied from 6um to 4um. All the taper lengths are 100um to the 1um wide silicon nitride waveguides. In addition, a GSG design is also applied to the ridge waveguide laser in order to test the high speed characteristics of the hybrid QD laser.

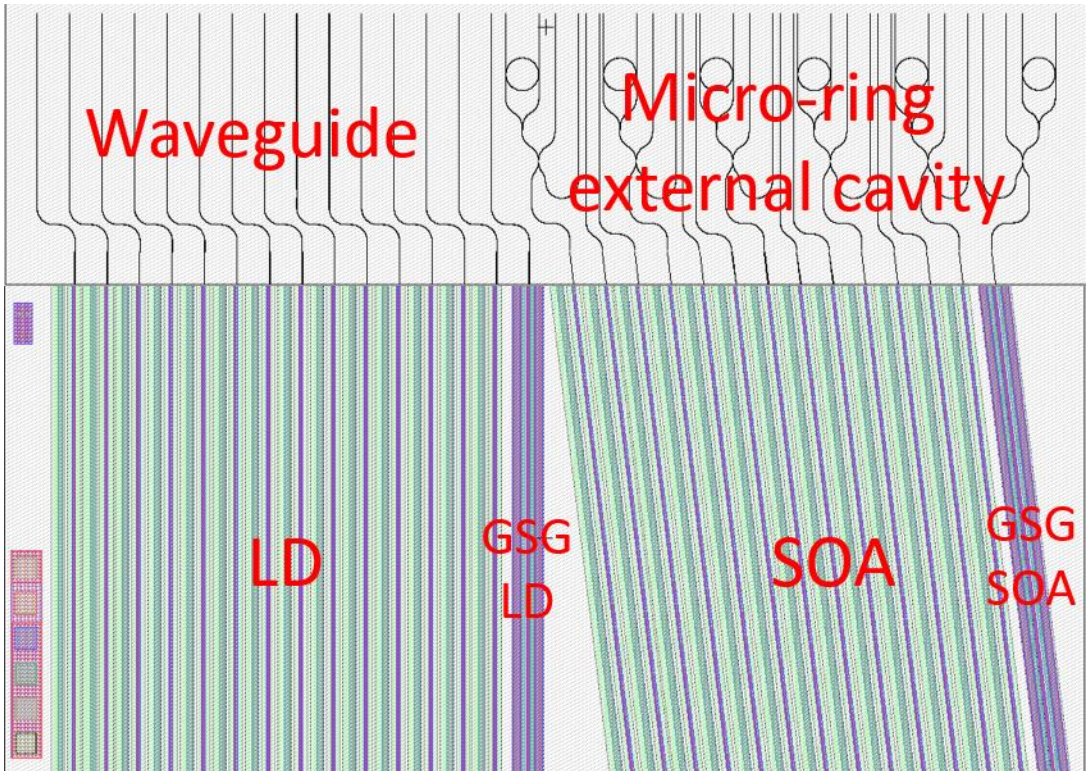

Figure 8-10 Layout designs of QD gain chip (SOA and LD) and silicon nitride passive devices (straight waveguide and ring reflectors).

8.5.2 Experiment

The silicon nitride PIC chips were fabricated by standard processes such as LPCVD of the silicon nitride film, thermal annealing, DUV photolithography, PECVD oxide cladding and deep etching of trenches for fiber coupling. An optical microscope image of a fabricated Si_3N_4 ring reflector PIC is shown in the inset of Figure 8-11. The chip is then tested by external coupling from an SOA source (Thorlab BOA1017P). To mimic the proposed design, the HR coating function is included in the setup by using a sagnac loop fiber circuit or a fiber retroreflector (Thorlab P1-SMF28-P01-1). A polarization controller is also used to optimize the polarization of the external cavity since the final integrated configuration is optimized for TE polarization both inside the QD laser cavity and the

silicon nitride waveguide. Ultra-high numerical aperture (UHNA) fibers are used for silicon nitride chip coupling to achieve coupling efficiencies of ~45%.

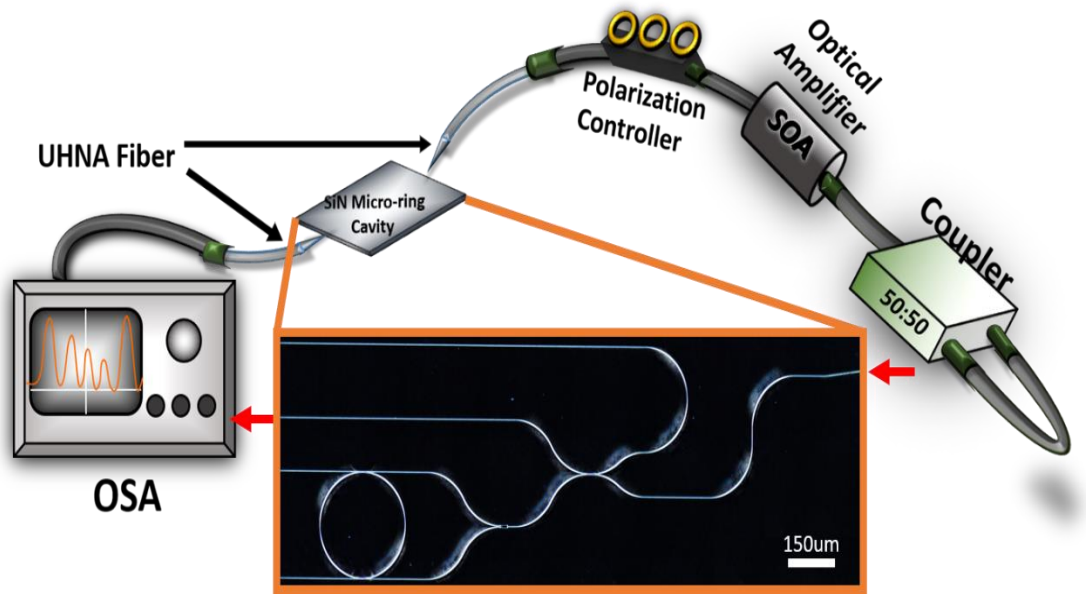

Figure 8-11 Schematic diagram of the experimental setup to characterize the hybrid tunable laser Si_3N_4 PICs. Inset is the optical microscope picture of a Si_3N_4 ring reflector PIC.

8.5.3 Characterization and discussion

With the setup introduced in section 8.5.2, the light-intensity (L-I) characterization was measured by coupling the output light off-chip to a calibrated infrared InGaAs photodetector (Newport 818-IR/DB). The threshold current of this external cavity laser was found to be ~50mA. Figure 8-13a shows the optical spectrum of the external laser before threshold current with an injection current of 50 mA which only exhibits spontaneous emission. It also shows the spectrum of the laser just starting to lase at a 53mA operation current. Since the Si_3N_4 rings are designed with a 150um ring, the FSR is not large enough to provide single mode optical feedback inside the external cavity. As a result, when increasing the injection current up to 210mA, as shown in Figure 8-13b, other longitudinal modes arise. These additional longitudinal modes can be suppressed by adding

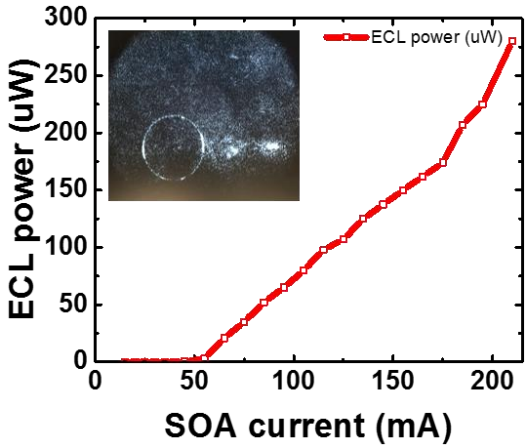

Figure 8-12 L-I characterization of external-cavity laser. Inset shows the infrared picture of silicon nitride ring in resonance.

a DBR design either on the Si_3N_4 chip or on the SOA gain chip. By optimizing the injection current, a stable single mode laser with the optimum power can be achieved at an injection current of 60mA at an emission wavelength of 1343.5nm as shown in Figure 8-13c. The side mode suppression ratio (SMSR) and full width half maximum (FWHM) linewidth of the laser were measured to be 35dB and 0.3nm, respectively. The linewidth of the laser can be even narrower with the use of a Si_3N_4 ring resonator with a higher quality factor. The Si_3N_4 chips used in this experiment were not annealed to remove the dangling bond in the

Si_3N_4 films, and as a result, the highest Q-factor of the rings was only ~80k. Also, as shown in the inset of Figure 8-13b, the overlapping laser peaks indicate that the OSA has a limited resolution. The actual laser linewidth may smaller than 0.3nm. The two close peaks are

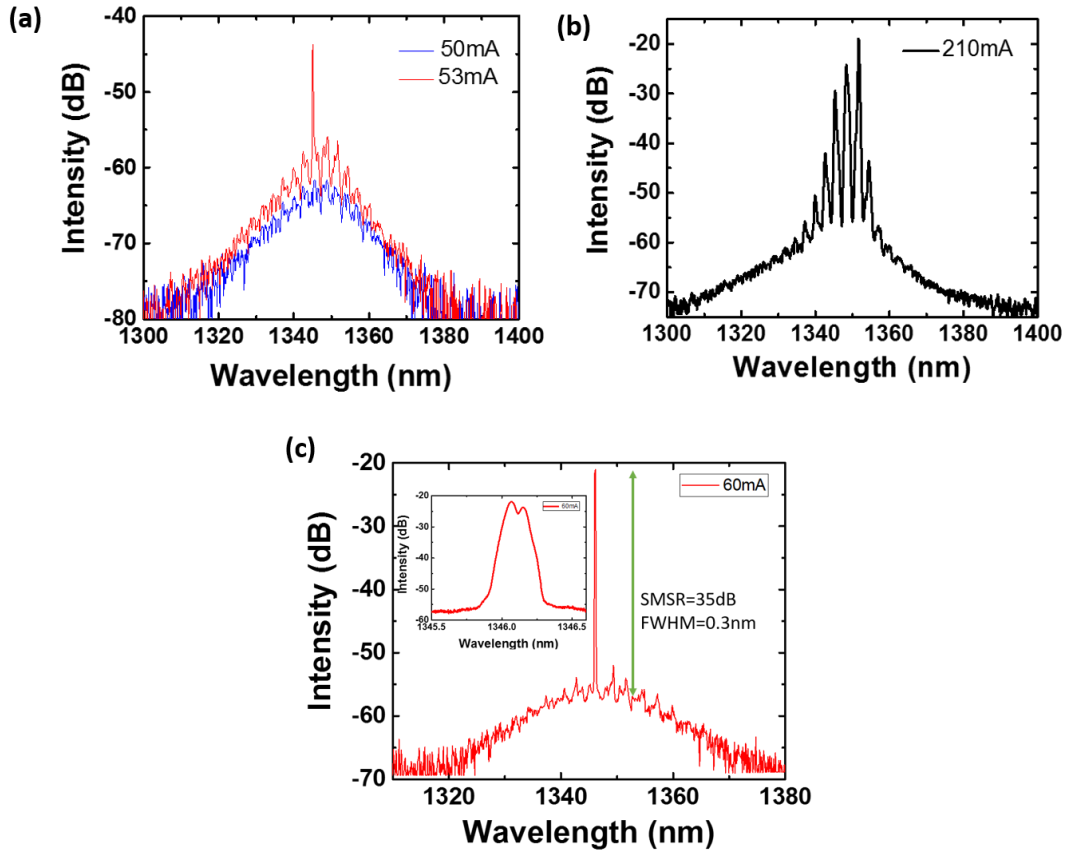

Figure 8-13 Optical spectrum of the external cavity laser with the injection currents at a) 50mA, 53mA, b) 210mA and c) 60mA (inset: zoom in optical spectrum at 60mA injection current).

introduced as a result of the counter-propagating waves within the ring reflector.

The thermal tuning properties were tested by external heating of the chip using a thermo-electric cooler (TEC) mounted underneath the copper stage as shown in the inset of Figure 8-14b. The external laser was operated at 60mA, so as to only allow emission in a single longitudinal mode during the thermal tuning characterization. In Figure 8-14a, the external laser is shown to operate at 1345.88nm at 22.8˚C. As the temperature was increased to 27.5˚C, the operating wavelength of laser shifted to 1345.99nm due to the

thermo-optic effect of the nitride ring resonator. Figure 8-13b shows a fit of the thermo-optic coefficient which is ~0.23nm/ ˚C. The off-chip TEC cannot heat the chip to high

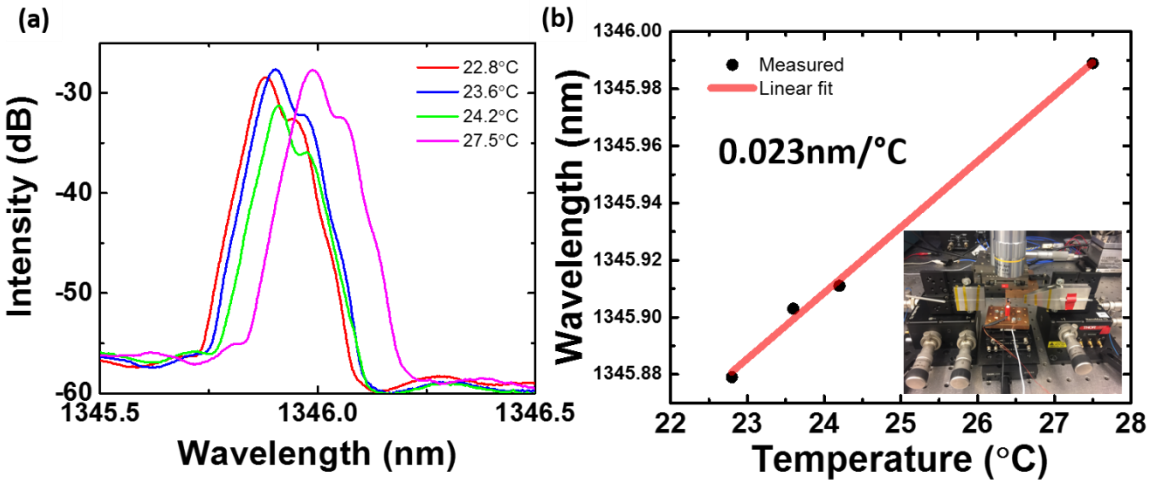

Figure 8-14 (a) Laser tuning optical spectra with temperatures ranging from 22.8 to 27.5 ˚C. (b) Linear fitting of the thermal tuning coefficient of Si_3N_4 feedback ring resonator. Inset: picture of external laser set up.

temperatures due to its poor heating efficiency. A more efficient on-chip heater can be designed in the future, enabling localized heating of the nitride ring so that the ring resonance can be tuned over a broader range.

At higher temperatures, a mode hopping effect is observed as shown in Figure 8-15. When the temperature is changed from 27.8 to 28.2 ˚C, the operating wavelength of the laser jumps from 1346.02 to 1348.36nm. This mode hopping effect is mainly caused by the mode mismatch between the external gain and the nitride waveguide which is induced by the thermal drift of the nitride chip. This problem can be solved by designing a feedback loop to monitor the wavelength drift and control the injection current of the gain chip such that the mode can be matched between the gain and nitride PIC chip.

8.6 Conclusion

In this chapter, we have proposed a butt-joint coupled heterogenous integration platform that uses Pd-GaAs wafer bonding. The details of the fabrication steps are discussed, and the design of the platform is simulated. By using the proposed platform, a hybrid tunable laser device is investigated. A proof of concept tunable laser is demonstrated by externally coupling light from a BOA to a Si_3N_4 PIC chip. The external-cavity tunable laser could operate with a single mode at O-band with a SMSR of 35dB at 60mA. The

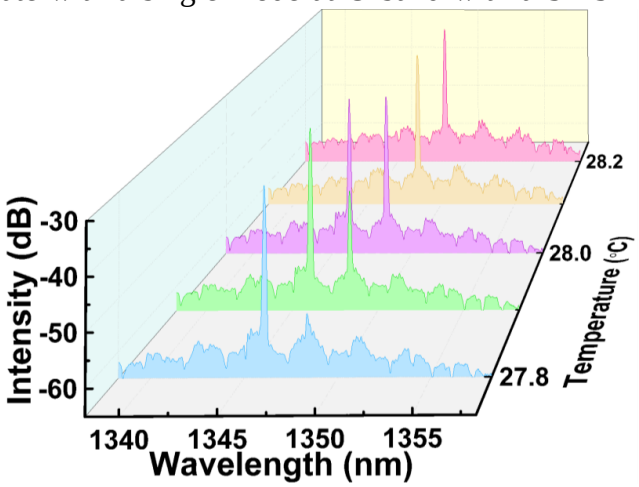

Figure 8-15 Optical spectrum of external laser with temperature tuned from 27.8 to 28.2˚C

thermal tuning coefficient of the laser is measured to be ~0.023nm/ ˚C. From the results of

the external cavity tunable laser, it is promising to achieve an SOA QD gain chip butt-joint heterogeneously integrated with a Si_3N_4 PIC chip.

9 SUMMARY AND FUTURE WORK

The purpose of the work discussed in this dissertation is to solve one of the key challenges faced by silicon photonic integrated circuits: laser integration. The major contribution of this dissertation is the development of hybrid InAs quantum dot lasers integrated on silicon by Pd-GaAs wafer bonding technology. The key to our approach is the Pd-GaAs wafer bonding that provides both decent electric and heat dissipation properties between the III/V epitaxial material and the silicon substrate. This wafer bonding platform avoids the lattice mismatch problems between the III\V and the silicon substrate, resulting in a simpler bonding process compared with oxide plasma enhanced bonding. In addition, the QD laser has unique properties such as high temperature stability, large modulation bandwidth and low power consumption which make it a good candidate as a laser source for hybrid integration to a silicon photonic PIC. The major achievements of this work include: 1) Design and fabrication of a broadband QD gain chip by taking advantage of the homogeneous broadening properties of QDs to provide the base material for integrated comb lasers and MLLs; 2) Developed a Pd-GaAs low temperature bonding process that was used to demonstrate several types of lasers on Si: hybrid ridge waveguide lasers, broadband comb lasers and mode-locked lasers; 3) Investigated two key steps to build up the integration platform: chip to chip butt-joint coupling between a QD laser and a silicon photonic waveguide and a smooth surface etch profile induced by a bromine ion beam-assisted etching (Br-IBAE) process; 4) Proposed butt-joint heterogeneous

integration platform by Pd-GaAs wafer bonding and demonstrate a proof of concept external cavity Si_3N_4 tunable laser based on the same platform.

9.1 InAs QD broadband gain chip

As discussed in Chapter 2, a dip-free broadband InAs QD gain chip was demonstrated. Due to the inhomogeneous broadening effect of QDs, three groups of InAs QDs were designed and intermixed by a combination of in-situ and ex-situ annealing to achieve a broadband electronic light emission spectrum. **With current injection of 100 mA, a broad and uniform spectrum with linewidths of 100 nm and 218 nm at 3 dB and 10 dB, respectively, was obtained. In addition, no significant dip was observed in the spectrum with injection currents ranging from 50 μA to 100 mA.** This broadband QD gain chip laid the ground work to develop the comb laser and mode-locked QD laser to integrate with Si.

9.2 Hybrid QD Laser on Silicon by Pd-GaAs wafer bonding

Presented in Chapters 3,4 and 5, different types of InAs QD lasers were investigated using the Pd-GaAs wafer bonding platform. The focuse of Chapter 3 was the Pd-GaAs bonding process between an epitaxially grown InAs QD laser and a Si substrate. **A uniform void-free bonding interface was achieved at temperatures low enough (250˚C) to maintain the quality of the III/V materials. The low interfacial resistivity of 0.2 Ωcm^2 was formed during the bonding which gives fabrication flexibilities to make the bottom contacts on either the top or bottom of the Si substrate.** Based on the low temperature bonding process, a hybrid InAs QD ridge waveguide laser was demonstrated

with **continuous wave (CW) operation at up to 100˚C with a ~2mW output.** Due to the p-side down bonding configuration and enhanced thermal dissipation of the silicon substrate, **the bonded laser showed a lower threshold current than the unbonded laser.**

Chapter 4 demonstrated a bonded broadband comb laser that made use of the gain chip material developed in Chapter 2. **An InAs QD comb laser was realized with a 3dB linewidth of 20 nm, measured with electroluminescence. The comb spectrum exhibited uniform power with less than 1 dB variation.**

An InAs quantum dot mode-locked laser was demonstrated in Chapter 5. Due to inhomogeneous broadening and ultrafast carrier dynamics, InAs quantum dots have key advantages that make them well suited for Mode-locked lasers (MLLs). **A passively mode-locked InAs quantum dot laser on Si was first demonstrated at a repetition rate of ~7.3 GHz under appropriate bias conditions. A nearly transfer limited pulse was achieved with a pulse width and optical bandwidth of 2 ps and 0.97 nm, respectively. In addition, the single cavity mode-locked laser and colliding pulse mode-locked laser were also demonstrated on Si by Pd-GaAs bonding.**

9.3 Preparation of InAs QD Laser integration to PICs

The optical feedback effect observed in the chip to chip butt-joint integration configuration was investigated in Chapter 6. Light was successfully coupled from a QD laser to a Si waveguide. An anti-reflection (AR) coating was used on the Si photonic chip to minimize the feedback from the interface between the QD chip and the SOI chip.

Stabilization of the laser by use of the AR coating provided valuable information for further development of the butt-joint heterogeneous integrated configuration.

Chapter 7 explored the use of a bromine ion beam-assisted etching (Br-IBAE) process for realizing etched facet lasers. For integrated photonic circuits, the laser cavity defined by cleaving may limit the design. An inter-chip laser design could solve this problem by creating laser facet by dry etching technology. By using a Br-IBAE process, a dry-etched facet laser was achieved with a threshold current density J_{th}, and slope efficiency, η_i of 480 A/cm^2 and 34%, respectively. **The etched facet reflectively is ~0.28 which is an improvement over the cleaved facet (0.32).** We believe the reflectivity can be further optimized by tuning the etching recipe or by replacing the etch through facet configuration with a DBR design to control the reflectivity.

9.4 Butt-joint heterogeneous integration platform by Pd-GaAs wafer bonding

Chapter 8 proposed a butt-joint heterogeneous integration platform by Pd-GaAs wafer bonding. Compared with other laser integration platforms, this platform is a good compromise between integration density, fabrication complexity and coupling efficiency. Details of the design, simulation and fabrication of the platform were also discussed. A proof of concept external tunable laser was demonstrated with an externally coupled BOA source to a Si_3N_4 PIC. **The laser exhibited single mode operation at O-band with a SMSR of 35dB at 60mA. The thermal tuning coefficient of the laser was measured to be ~0.023nm/ ˚C.**

9.5 Future work

The work presented in this dissertation is focused on the integration of QD laser sources with silicon photonic integrated circuits. There is certainly a huge scope for further development in several aspects of the work. Continued research in the QD laser integration platform can be divided in the following areas:

1) Fully integrated hybrid tunable laser based on a butt-joint heterogeneous integration platform

The platform demonstrated in Chapter 8 has not been fully integrated yet. The quantum dot gain chip needs to be bonded onto a silicon PIC chip as proposed. The AR coating deposition is required before the precise flip-chip bonding step (also requiring further investigation). Currently, the heterogeneous butt-joint coupling integration platform is designed for coupling from the laser from only one side, it also can be extended to butt-joint coupling from both sides of the gain chip. In that configuration, both sides of the laser cavity can be defined on a passive PIC chip, such as DBR gratings, ring resonator etc. A more advanced narrow linewidth tunable laser can also be designed by inserting two microring reflectors with the Vernier effect.

2) Optimization of bonded QD lasers

In Chapter 3, the bonded InAs QD lasers were successfully demonstrated with a state of the art threshold current of 240 A/cm^2 and high operation temperature of up to 100ºC. However, the high-speed specifications are not well investigated. Currently, the laser can only be directly modulated at 5GHz because of the lack of high speed design of the

epitaxy structure and device layout. In order to increase the high-speed performance of InAs QD laser, a narrower barrier height, P-doped modulation barrier and a tunneling injection structure design could be used as reported in [168-170] . In addition, the bonded InAs QD laser chips can be designed with an impedance matching circuit to further enhance the modulation speed.[171]

3) QD modulator on Si

Not only are InAs QDs well suited for making lasers but also as a novel material for fabricating electrooptic (EO) modulators due to their high EO coefficient (>20 pm/V) caused by the quantum confined stark effect. [172] Since both a laser source and an EO modulator could be fabricated with same epitaxial structure, an integrated design consisting of a QD laser and a modulator can be on the III\V part and further integrated with the passive Arrayed Waveguide Grating (AWG) silicon nitride or SOI PIC by using the butt-joint heterogenous integration platform as proposed in Chapter 8.

4) Hybrid TOSA for OTDM system

In Chapter 5, a passive InAs QD mode-locked laser was demonstrated. We have also demonstrated a high-speed optical-time-division-multiplexing (OTDM) system by externally coupling a mode-locked laser into a silicon photonics OTDM PIC chip as shown in Figure 9-1. The next step is to fully integrate this OTDM system by using the butt-joint heterogenous integration platform demonstrated in Chapter 8.

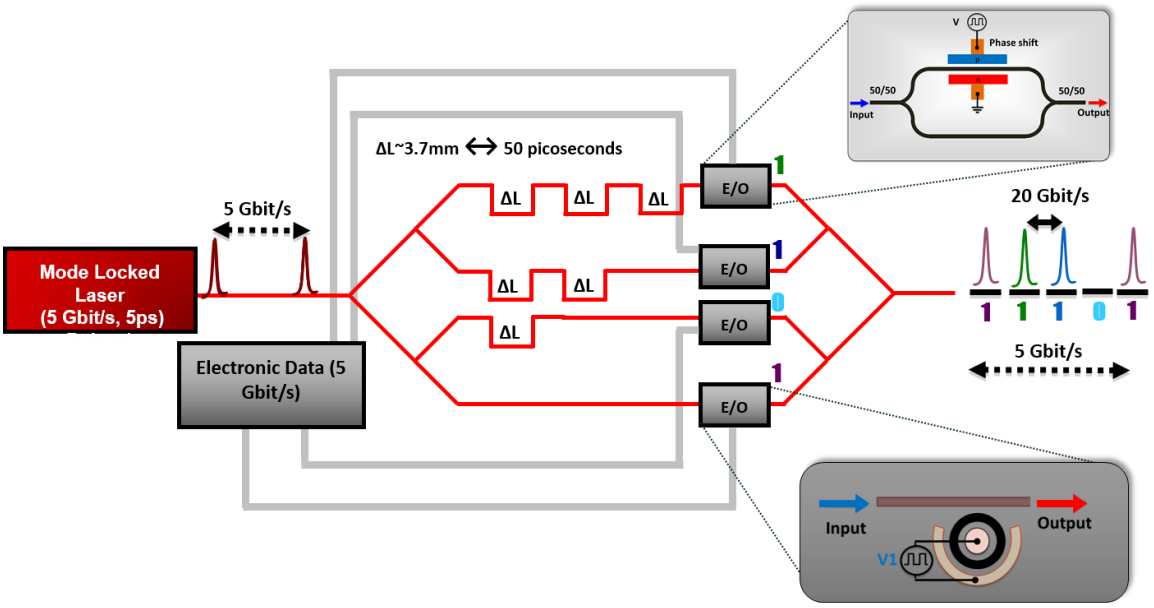

Figure 9-1 OTDM takes in short optical pulses operating at 5Gb/s (left) and multiplexes them to 5N Gbit/s (right) by splitting the original pulses into N separate channels and then recombining them after they go through bit-rate determined delays ΔL.[173]

In addition to the future work listed above, I believe the Pd-GaAs wafer bonded hybrid QD lasers and versatile butt-joint heterogenous integration platform can be leveraged to realize hybrid PICs for a variety of applications such as fully integrated coherent transceivers and LIDAR systems.

10 PUBLICATIONS

Journal Papers

1. Tison CC, Steidle JA, Fanto ML, **Wang Z**, Mogent NA, Rizzo A, Preble SF, Alsing PM. Path to increasing the coincidence efficiency of integrated resonant photon sources. Optics Express. 2017 Dec 25;25(26):33088-96.R.
2. Fan, X. Chen**, Z. Wang**, D. Custer, and J. Wan, "Flow-Regulated Growth of Titanium Dioxide (TiO2) Nanotubes in Microfluidics," Small, pp. 1701154-n/a, Art. no. 1701154
3. **Z. Wang**, M. L. Fanto, J. A. Steidle, A. A. Aboketaf, N. A. Rummage, P. M. Thomas, et al., "Passively mode-locked InAs quantum dot lasers on a silicon substrate by Pd-GaAs wafer bonding," Applied Physics Letters, vol. 110, p. 141110, 2017.
4. Steidle, J. A., Fanto, M. L., Preble, S. F., Tison, C. C., Howland, G. A., **Wang, Z.,** et al. Measurement of Quantum Interference in a Silicon Ring Resonator Photon Source. J. Vis. Exp. (122), e55257, doi:10.3791/55257 (2017).
5. **Wang, Zihao**, Ruizhe Yao, Stefan F. Preble, Chi-Sen Lee, Luke F. Lester, and Wei Guo. "High performance InAs quantum dot lasers on silicon substrates by low temperature Pd-GaAs wafer bonding." Applied Physics Letters 107, no. 26 (2015): 261107
6. Preble, S. F., Fanto, M. L., Steidle, J. A., Tison, C. C., Howland, G. A., **Wang, Z**., & Alsing, P. M. (2015). On-chip quantum interference from a single silicon ring-resonator source. Physical Review Applied, 4(2), 021001.
7. Cao, Liang, Abdelsalam Aboketaf, **Zihao Wang**, and Stefan Preble. "Hybrid amorphous silicon (a-Si: H)–LiNbO 3 electro-optic modulator." Optics Communications 330 (2014): 40-44.
8. Huang, Y., Kim, T.W., Xiong, S., Mawst, L.J., Kuech, T.F., Nealey, P.F., Dai, Y., **Wang, Z**., Guo, W., Forbes, D. and Hubbard, S.M., "InAs Nanowires Grown by Metal–Organic Vapor-Phase Epitaxy (MOVPE) Employing PS/PMMA Diblock Copolymer Nanopatterning." Nano letters 13.12 (2013): 5979-5984.

Conference Papers

1. Fanto, M. L., C. C. Tison, J. A. Steidle, T. Lu**, Z. Wang**, N. A. Mogent, A. Rizzo et al. "Integrated photon sources for quantum information science applications." In Quantum Information Science and Technology III, vol. 10442, p. 104420K. International Society for Optics and Photonics, 2017.
2. **Z. Wang**, S. F. Preble, M. L. Fanto, J. A. Steidle, C. Lee, and W. Guo, "InAs quantum dot mode-locked lasers on a Si substrate by Pd-GaAs wafer bonding," in Frontiers in Optics 2016, OSA Technical Digest (online) (Optical Society of America, 2016), paper FF5F.5.
3. J. A. Steidle, M. L. Fanto, C. C. Tison, **Z. Wang**, P. Alsing, and S. F. Preble, "High Performance Photon Sources for Quantum Silicon Photonics," in Frontiers in Optics 2016, OSA Technical Digest (online) (Optical Society of America, 2016), paper FTu3G.4.
4. R. Yao, N. Weir, C. Lee, **Z. Wang**, S. F. Preble, and W. Guo, "Broadband Swept-Source Laser in 1.1 to 1.3 μm with InAs Quantum Dot Gain Chip Devices," in Frontiers in Optics 2016, OSA Technical Digest (online) (Optical Society of America, 2016), paper FW5C.4.
5. Yao, R., **Wang, Z**., Preble, S., Lee, C. S., & Guo, W. (2016, November). Integration of InAs QD comb lasers with silicon photonics ring resonators. In Progress in Electromagnetic Research Symposium (PIERS) (pp. 3163-3163). IEEE.
6. Steidle, J. A., Fanto, M. L., Tison, C. C., **Wang, Z**., Alsing, P. M., & Preble, S. F. (2016, May). Efficiently heralded silicon ring resonator photon-pair source. In SPIE Commercial+ Scientific Sensing and Imaging (pp. 987304-987304). International Society for Optics and Photonics.
7. **Zihao Wang**, Ruizhe Yao, Stefan Preble, Chi-Sen Lee, Wei Guo. "Characterizations of optical feedback effects in InAs quantum dot lasers butt-joint coupled with silicon photonics wacveguides" *SPIE OPTO. International Society for Optics and Photonics, 2016.*
8. **Zihao Wang**, Ruizhe Yao, Stefan Preble, Chi-Sen Lee, Wei Guo. "Integration of InAs quantum dot comb lasers with silicon photonics components" *31th North American Molecular Beam Epitaxy Conference* (NAMBE), Mayan Riviera, Oct4-7, 2015

9. **Zihao Wang**, Ruizhe Yao, Stefan Preble, Chi-Sen Lee, Jeffrey Steidle, Wei Guo. "Room temperature CW operation of 1.3um quantum dot lasers on a Si substrate by Pd-mediated wafer bonding" *Integrated Photonics* Research. Optical Society of America, 2015.
10. Steidle, Jeffrey A., Michael L. Fanto, Christopher C. Tison**, Zihao Wang**, Stefan F. Preble, and Paul M. Alsing. "High spectral purity silicon ring resonator photon-pair source." In SPIE Sensing Technology+ Applications, pp. 950015-950015. International Society for Optics and Photonics, 2015.
11. Lee, Chi-Sen, **Zihao Wang**, and Wei Guo. "Integration of passive components with high performance quantum dot lasers on silicon." Optical Interconnects Conference, 2013 IEEE.
12. **Wang, Z**., Yao, R., Kuperinik, J., Wang, W., & Guo, W. (2013, June). Photovoltaic Specialists Conference (PVSC), 2013 IEEE 39th (pp. 2483-2485). IEEE.

Patent

1. Wan, Jiandi, Rong Fan, and **Zihao Wang**. "Flow-Regulated Growth of Nanotubes." U.S. Patent Application 15/669,034, filed February 8, 2018.
2. Patent pending, “InAs quantum Dot Mode-Locked Lasers on Si by Pd-GaAs Wafer Bonding” filed April 5th, by Stefab Preble, **Zihao Wang**, Michael Fanto Rochester Institute of Technology.

11 APPENDICES

Electrically Pumped bonded QD-MLL Process Follower

1. Wafer bonding and film transfer
   - 1.1 RCA clean the Si wafer.
   - 1.2 Evaporate 500nm Pd by odd hour e-beam evaporator
   - 1.3 Ultrasonic clean GaAs pieces by Acetone, IPA, Ethanol and DI water in sequence, 5 min each step.
   - 1.4 Bonding GaAs to Si by Pd using Suss SB8e wafer bonder
     - 1.4.1 Cleave the Si wafer and GaAs sample in same size and align the edges from each other.
     - 1.4.2 Arrange 3 piece of GaAs/Si in equilateral triangle shape and left a 1cm diameter circle space in the center.
     - 1.4.3 Cut the graphite paper in right size the cover the GaAs pieces. Before covering, clean the graphite paper edges with IPA by cleanroom. Cover the GaAs pieces with graphite paper by using injector with adhesive rubber disc.
     - 1.4.4 Use a 1um thick Si wafer cover on top of the graphite paper and clip the sandwich structure with holder.
     - 1.4.5 Put the holder into bonder and cho0se the right bonding recipe. The temperature in recipe is 260C and steady hold for 90mins. Top pressure is 1000mbar for three 0.5*0.5cm^2 pieces.
   - 1.5 After bonding, use wax protect the GaAs piece, then polish the GaAs piece to 100um. Use citric acide(50%w/w) to hydrogenperoxide with ratio 5:1 and heated up to 60C to wet etching the GaAs. It takes around two hour etching to the stop layer.
   - 1.6 Remove AlGaAs etching stop layer by BOE (1:6)

2. Alignment mark metal deposition
   2.1 DI Rinse & Dehydration Bake (115C 2 min)
   2.2 LOR 3A 3000RPM 3000Ramp 60s, 5min 180C_____
   620 7i 2000RPM 1000Ramp 60s, 1min 90C____
   Auto step 0.4s____(Jobname:MLLONSI\1)
   1min 115C PEB___
   MIF726 70-75s___
   2.3 Oxford 81 O2 descum 30s__
   2.4 Remove native oxide in HCl:H20(1:10) for 10s
   2.5 Load into e-beam evaporator and deposit
   Ti:Au(200A;400A)
   Ti:____ Au:____
   2.6 Lift off in 1165 80C. Rinse in ISO, DI. O2 desucum in necessary to remove resist residue.
3. Ridge etching
   3.1 Oxford PECVD SiO2 Deposition
   Clean Chamber 10min
   SiO2 thickness: 500nm____
   3.2 PATTERN SiO2 For RIDGE ETCH
   Acetone/Iso/N2 Clean
   115C 2min dehydrate
   O2 descum 30 seconds
   Spin P20 3000RPM 1000RMP 60s
   Spin SPR220 3.0 3000RPM 1000RMP 60s
   Softbake115C 90s
   AS200 Stepper exposure 0.30sec
   PEB 115C 2min
   Develop in MIF726 90sec
   O2 descum 30 seconds
   3.3 P2 measure resist Height____
   3.4 Oxford 81 etch oxide
   3.5 Receipe: CHF3/Ar ER=24nm/min
   Need O2 clean chamber 10min every 10min etching

O2 descum 30 seconds

3.6 Strip PR in YES asher using recipe 8 10min*3

3.7 Or using Oxford 81 O2 clean recipe, need to clean chamber 15 min before loading samples.
Stripping time: 20min _____

3.8 Rinse in ISO\DI

3.9 RIE RIDGE ETCH (PT770)
Seasoning chamber with recipe DOE.rcp
(Ar/BCl3 5/15; RF1:100W, RF2:200W)
ER(GaAs)=81.2nm/min ER(Innolume)=81.4-87.4nm/min
ER(oxide)=11nm/min
Run Laser sample with GaAs control wafer with same patterns and same size

4. Mesa etching

4.1 Strip Oxide hard mask (option)

4.2 Deposit low rate oxide 500nm by Oxford PECVD

4.3 Same process flow as 3

5. P-metal deposition

5.1 DI Rinse & Dehydration Bake (115C 2 min)

5.2 LOR 5A
500RPM 100 5sec
3000RPM 1000Ramp 60s, 5min 180C_____
SPR 3.0 3000RPM 1000Ramp 60s, 1min 90C____
Auto step 0.4s____(Jobname:MLLONSI\4)
1min 115C PEB___
MIF726 70-75s___

5.3 Oxford 81 O2 descum 1min __

5.4 Remove native oxide in HCl:H20(1:10) for 15s

5.5 Load into e-beam evaporator and deposit
Ti\Pt\Ti\Au(200\200\200\5000A)
Ti:____ Pt:____Ti:_____Au:_____

5.6 Lift off in 1165 80C. Rinse in ISO, DI. O2 desucum in necessary to remove resist residue.

5.7 Annealing with GaAs wafer covered @400C 1min

6. VIA
   6.1 Oxford PECVD deposit 800 nm SiO2, Low T recipe 9min 30s_____nm
   6.2 Acetone/Iso/N2 Clean
   115C 2min dehydrate
   O2 descum 30 seconds
   Spin P20 3000RPM 1000RMP 60s
   Spin SPR220 3.0 3000RPM 1000RMP 60s
   Softbake115C 90s
   AS200 Stepper exposure 0.30sec
   PEB 115C 2min
   Develop in MIF726 90sec
   O2 descum 30 seconds
   6.3 Oxford81 chamber clean 10min and etch VIA using recipe CHF3\O2 10min*4 and clean the chamber every 10min
7. N-metal
   7.1 DI Rinse & Dehydration Bake (115C 2 min)
   7.2 LOR 5A
   500RPM 100 5sec
   3000RPM 1000Ramp 60s, 5min 180C_____
   SPR 3.0 3000RPM 1000Ramp 60s, 1min 90C____
   Auto step 0.45s____ (Jobname:MLLONSI\4)
   1min 115C PEB___
   MIF726 120s___
   7.3 Oxford 81 O2 descum 1min __
   7.4 Remove native oxide in HCl:H20(1:10) for 15s
   7.5 Load into e-beam evaporator and deposit Ni\Ge\Au\Ti\Au(250\325\650\200\5000A)
   Ni:____ Ge:____Au:_____Ti:_____Au:_____
   7.6 Lift off in 1165 80C. Rinse in ISO, DI. O2 desucum in necessary to remove resist residue.

7.7 Annealing with GaAs wafer covered @385C 1min

12 REFERENCE

[1] G. Roelkens, A. Abassi, P. Cardile, U. Dave, A. De Groote, Y. de Koninck, *et al.*, "III-V-on-Silicon photonic devices for optical communication and sensing," in *Photonics*, 2015, pp. 969-1004.

[2] A. W. Fang, H. Park, O. Cohen, R. Jones, M. J. Paniccia, and J. E. Bowers, "Electrically pumped hybrid AlGaInAs-silicon evanescent laser," *Optics express*, vol. 14, pp. 9203-9210, 2006.

[3] M. J. Heck, H.-W. Chen, A. W. Fang, B. R. Koch, D. Liang, H. Park, *et al.*, "Hybrid silicon photonics for optical interconnects," *IEEE Journal of Selected Topics in Quantum Electronics*, vol. 17, pp. 333-346, 2011.

[4] T. Shimizu, N. Hatori, M. Okano, M. Ishizaka, Y. Urino, T. Yamamoto, *et al.*, "Multichannel and high-density hybrid integrated light source with a laser diode array on a silicon optical waveguide platform for interchip optical interconnection," *Photonics Research*, vol. 2, pp. A19-A24, 2014.

[5] T. Barwicz, Y. Taira, T. W. Lichoulas, N. Boyer, Y. Martin, H. Numata, *et al.*, "A Novel Approach to Photonic Packaging Leveraging Existing High-Throughput Microelectronic Facilities," *IEEE Journal of Selected Topics in Quantum Electronics*, vol. 22, pp. 455-466, 2016.

[6] A. W.-L. Fang, *Silicon evanescent lasers*: ProQuest, 2008.

[7] G. E. Moore, "Cramming more components onto integrated circuits, Electronics, Volume 38, Number 8, April 19, 1965," *Also available online from ftp://download. intel. com/research/silicon/moorespaper. pdf*, 1965.

[8] D. A. Miller, "Device requirements for optical interconnects to silicon chips," *Proceedings of the IEEE*, vol. 97, pp. 1166-1185, 2009.

[9] A. V. Krishnamoorthy, K. W. Goossen, W. Jan, X. Zheng, R. Ho, G. Li, *et al.*, "Progress in low-power switched optical interconnects," *IEEE Journal of Selected Topics in Quantum Electronics*, vol. 17, pp. 357-376, 2011.

[10] R. A. Soref, J. Schmidtchen, and K. Petermann, "Large single-mode rib waveguides in GeSi-Si and Si-on-SiO/sub 2," *IEEE Journal of Quantum Electronics*, vol. 27, pp. 1971-1974, 1991.

[11] C. Zhao, G. Li, E. Liu, Y. Gao, and X. Liu, "Silicon on insulator Mach–Zehnder waveguide interferometers operating at 1.3 μm," *Applied physics letters*, vol. 67, pp. 2448-2449, 1995.

[12] P. Trinh, S. Yegnanarayanan, F. Coppinger, and B. Jalali, "Silicon-on-insulator (SOI) phased-array wavelength multi/demultiplexer with extremely low-polarization sensitivity," *IEEE Photonics Technology Letters*, vol. 9, pp. 940-942, 1997.

[13] F. Gardes, D. Thomson, N. Emerson, and G. Reed, "40 Gb/s silicon photonics modulator for TE and TM polarisations," *Optics express*, vol. 19, pp. 11804-11814, 2011.

[14] Q. Xu, B. Schmidt, S. Pradhan, and M. Lipson, "Micrometre-scale silicon electro-optic modulator," *nature*, vol. 435, pp. 325-327, 2005.

[15] Y. Kang, H.-D. Liu, M. Morse, M. J. Paniccia, M. Zadka, S. Litski, *et al.*, "Monolithic germanium/silicon avalanche photodiodes with 340 GHz gain–bandwidth product," *Nature photonics*, vol. 3, pp. 59-63, 2009.

[16] B. Jalali and S. Fathpour, "Silicon photonics," *Journal of lightwave technology*, vol. 24, pp. 4600-4615, 2006.

[17] O. Bisi, S. Ossicini, and L. Pavesi, "Porous silicon: a quantum sponge structure for silicon based optoelectronics," *Surface science reports*, vol. 38, pp. 1-126, 2000.

[18] L. T. Canham, "Silicon quantum wire array fabrication by electrochemical and chemical dissolution of wafers," *Applied Physics Letters*, vol. 57, pp. 1046-1048, 1990.

[19] W. L. Wilson, P. Szajowski, and L. Brus, "Quantum confinement in size-selected, surface-oxidized silicon nanocrystals," *SCIENCE-NEW YORK THEN WASHINGTON-*, vol. 262, pp. 1242-1242, 1993.

[20] Z. Lu, D. Lockwood, and J. Baribeau, "Quantum confinement and light emission in SiO2/Si superlattices," *Nature*, vol. 378, p. 258, 1995.

[21] S. G. Cloutier, P. A. Kossyrev, and J. Xu, "Optical gain and stimulated emission in periodic nanopatterned crystalline silicon," *Nature materials*, vol. 4, pp. 887-891, 2005.

[22] H. Rong, S. Xu, Y.-H. Kuo, V. Sih, O. Cohen, O. Raday, *et al.*, "Low-threshold continuous-wave Raman silicon laser," *Nature Photonics*, vol. 1, pp. 232-237, 2007.

[23] M. Lamponi, S. Keyvaninia, C. Jany, F. Poingt, F. Lelarge, G. De Valicourt, *et al.*, "Low-threshold heterogeneously integrated InP/SOI lasers with a double adiabatic taper coupler," *IEEE photonics technology letters*, vol. 24, pp. 76-78, 2012.

[24] J. Yang, P. Bhattacharya, and Z. Mi, "High-Performance $\ hbox {In} _ {0.5}\ hbox {Ga} _ {0.5}\ hbox {As/GaAs} $ Quantum-Dot Lasers on Silicon With Multiple-Layer

Quantum-Dot Dislocation Filters," *IEEE Transactions on Electron Devices*, vol. 54, pp. 2849-2855, 2007.

[25] S. Chen, W. Li, J. Wu, Q. Jiang, M. Tang, S. Shutts, *et al.*, "Electrically pumped continuous-wave III–V quantum dot lasers on silicon," *Nature Photonics*, 2016.

[26] Y. Wan, Q. Li, A. Y. Liu, A. C. Gossard, J. E. Bowers, E. L. Hu, *et al.*, "Optically pumped 1.3 μm room-temperature InAs quantum-dot micro-disk lasers directly grown on (001) silicon," *Optics letters*, vol. 41, pp. 1664-1667, 2016.

[27] N. Basov, O. Krokhin, and Y. M. Popov, "Possibility of using indirect transitions to obtain negative temperatures in semiconductors," *J. Exp. Theo. Phys*, vol. 39, p. 1033, 1961.

[28] Z. I. Alferov, "Nobel Lecture: The double heterostructure concept and its applications in physics, electronics, and technology," *Reviews of modern physics*, vol. 73, p. 767, 2001.

[29] Y. Arakawa and H. Sakaki, "Multidimensional quantum well laser and temperature dependence of its threshold current," *Applied Physics Letters*, vol. 40, pp. 939-941, 1982.

[30] N. Kirstaedter, N. Ledentsov, M. Grundmann, D. Bimberg, V. Ustinov, S. Ruvimov, *et al.*, "Low threshold, large T/sub o/injection laser emission from (InGa) As quantum dots," *Electronics Letters*, vol. 30, pp. 1416-1417, 1994.

[31] G. Liu, A. Stintz, H. Li, K. Malloy, and L. Lester, "Extremely low room-temperature threshold current density diode lasers using InAs dots in In/sub 0.15/Ga/sub 0.85/As quantum well," *Electronics Letters*, vol. 35, pp. 1163-1165, 1999.

[32] S. Fathpour, Z. Mi, P. Bhattacharya, A. Kovsh, S. Mikhrin, I. Krestnikov, *et al.*, "The role of Auger recombination in the temperature-dependent output characteristics (T 0=∞) of p-doped 1.3 μm quantum dot lasers," *Applied Physics Letters*, vol. 85, pp. 5164-5166, 2004.

[33] K. Barnham and D. Vvedensky, *Low-dimensional semiconductor structures: Fundamentals and device applications*: Cambridge University Press, 2008.

[34] P. M. Smowton, E. Herrmann, Y. Ning, H. D. Summers, P. Blood, and M. Hopkinson, "Optical mode loss and gain of multiple-layer quantum-dot lasers," *Applied Physics Letters*, vol. 78, pp. 2629-2631, 2001.

[35] S. C. Woodworth, D. T. Cassidy, and M. J. Hamp, "Sensitive absorption spectroscopy by use of an asymmetric multiple-quantum-well diode laser in an external cavity," *Applied optics*, vol. 40, pp. 6719-6724, 2001.

[36] N. Kuramoto and K. Fujii, "Volume determination of a silicon sphere using an improved interferometer with optical frequency tuning," *IEEE transactions on instrumentation and measurement,* vol. 54, pp. 868-871, 2005.

[37] B. Stevens, D. Childs, K. Groom, M. Hopkinson, and R. Hogg, "All semiconductor swept laser source utilizing quantum dots," *Applied Physics Letters,* vol. 91, p. 1119, 2007.

[38] S. B. Yoo, "Wavelength conversion technologies for WDM network applications," *Lightwave Technology, Journal of,* vol. 14, pp. 955-966, 1996.

[39] D. Bimberg and U. W. Pohl, "Quantum dots: promises and accomplishments," *Materials Today,* vol. 14, pp. 388-397, 2011.

[40] A. J. Zilkie, J. Meier, M. Mojahedi, P. J. Poole, P. Barrios, D. Poitras, *et al.*, "Carrier Dynamics of Quantum-Dot, Quantum-Dash, and Quantum-Well Semiconductor Optical Amplifiers Operating at 1.55 μm," *Quantum Electronics, IEEE Journal of,* vol. 43, pp. 982-991, 2007.

[41] H. S. Djie, C. E. Dimas, and B. S. Ooi, "Wideband quantum-dash-in-well superluminescent diode at 1.6 μm," *Photonics Technology Letters, IEEE,* vol. 18, pp. 1747-1749, 2006.

[42] M. Z. M. Khan, M. A. Majid, T. K. Ng, and B. S. Ooi, "High performance superluminescent diode with InAs quantum-dashes and chirped AlGaInAs barriers active region," ed: IEEE.

[43] H. S. Djie, C. E. Dimas, and B. S. Ooi, "Wideband quantum-dash-in-well superluminescent diode at 1.6 μm," *IEEE photonics technology letters,* vol. 18, pp. 1747-1749, 2006.

[44] M. Z. M. Khan, M. A. Majid, T. K. Ng, and B. S. Ooi, "High performance superluminescent diode with InAs quantum-dashes and chirped AlGaInAs barriers active region," 2013.

[45] S. B. Yoo, "Wavelength conversion technologies for WDM network applications," *Journal of Lightwave Technology,* vol. 14, pp. 955-966, 1996.

[46] A. J. Zilkie, J. Meier, M. Mojahedi, P. J. Poole, P. Barrios, D. Poitras, *et al.*, "Carrier dynamics of quantum-dot, quantum-dash, and quantum-well semiconductor optical amplifiers operating at 1.55 μm," *IEEE Journal of Quantum Electronics,* vol. 43, pp. 982-991, 2007.

[47] N. Perret, D. Morris, L. Franchomme-Fossé, R. Côté, S. Fafard, V. Aimez, *et al.*, "Origin of the inhomogenous broadening and alloy intermixing in InAs/GaAs self-assembled quantum dots," *Physical Review B,* vol. 62, p. 5092, 2000.

[48] R. Heitz, M. Veit, N. N. Ledentsov, A. Hoffmann, D. Bimberg, V. M. Ustinov, *et al.*, "Energy relaxation by multiphonon processes in InAs/GaAs quantum dots," *Physical Review B,* vol. 56, p. 10435, 1997.

[49] D. M. Bruls, J. W. A. M. Vugs, P. M. Koenraad, H. W. M. Salemink, J. H. Wolter, M. Hopkinson, *et al.*, "Determination of the shape and indium distribution of low-growth-rate InAs quantum dots by cross-sectional scanning tunneling microscopy," *Applied Physics Letters,* vol. 81, p. 1708, 2002.

[50] J. M. García, G. Medeiros-Ribeiro, K. Schmidt, T. Ngo, J. L. Feng, A. Lorke, *et al.*, "Intermixing and shape changes during the formation of InAs self-assembled quantum dots," *Applied Physics Letters,* vol. 71, pp. 2014-2016, 1997.

[51] A. A. Guzelian, U. Banin, A. V. Kadavanich, X. Peng, and A. P. Alivisatos, "Colloidal chemical synthesis and characterization of InAs nanocrystal quantum dots," *Applied Physics Letters,* vol. 69, p. 1432, 1996.

[52] C. E. Dimas, H. S. Djie, and B. S. Ooi, "Superluminescent diodes using quantum dots superlattice," *Journal of Crystal Growth,* vol. 288, pp. 153-156, 2/2/ 2006.

[53] F. Ginovart, J. C. Simon, and I. Valiente, "Gain recovery dynamics in semiconductor optical amplifier," *Optics Communications,* vol. 199, pp. 111-115, 11/15/ 2001.

[54] M. L. Nielsen, J. Mørk, R. Suzuki, J. Sakaguchi, and Y. Ueno, "Experimental and theoretical investigation of the impact of ultra-fast carrier dynamics on high-speed SOA-based all-optical switches," *Optics Express,* vol. 14, pp. 331-347, 2006/01/09 2006.

[55] I. O'Driscoll, T. Piwonski, J. Houlihan, G. Huyet, R. J. Manning, and B. Corbett, "Phase dynamics of InAs⁄GaAs quantum dot semiconductor optical amplifiers," *Applied Physics Letters,* vol. 91, p. 263506, 2007.

[56] X. Li, P. Jin, Q. An, Z. Wang, X. Lv, H. Wei, *et al.*, "A high-performance quantum dot superluminescent diode with a two-section structure," *Nanoscale research letters,* vol. 6, pp. 1-5, 2011.

[57] W.-S. Wang, M.-L. Zhang, and Z.-D. Chen, "Influence of a phonon bath in a quantum dot cavity QED system: Dependence of the shape," *Chinese Physics B,* vol. 23, p. 094205, 2014.

[58] Q. An, P. Jin, Z. C. Wang, X. K. Li, and Z. G. Wang, "The Effect of Double-Pass Gain on the Performances of a Quantum-Dot Superluminescent Diode Integrated With a

Semiconductor Optical Amplifier," *Lightwave Technology, Journal of,* vol. 30, pp. 2684-2688, 2012.

[59] Z. Y. Zhang, Q. Jiang, I. J. Luxmoore, and R. A. Hogg, "A p-type-doped quantum dot superluminescent LED with broadband and flat-topped emission spectra obtained by post-growth intermixing under a GaAs proximity cap," *Nanotechnology,* vol. 20, p. 055204, 2009.

[60] H. Su and S. L. Chuang, "Room temperature slow and fast light in quantum-dot semiconductor optical amplifiers," *Applied physics letters,* vol. 88, p. 061102, 2006.

[61] M. Sugawara, T. Akiyama, N. Hatori, Y. Nakata, K. Otsubo, and H. Ebe, "Quantum-dot semiconductor optical amplifiers," 2002, pp. 259-275.

[62] W.-S. Liu and J.-I. Chyi, "Optical properties of InAs quantum dots with InAlAs⁄InGaAs composite matrix," *Journal of Applied Physics,* vol. 97, p. 024312, 2005.

[63] R. Jia, D. S. Jiang, H. Y. Liu, Y. Q. Wei, B. Xu, and Z. G. Wang, "Influence of combined InAlAs and InGaAs strain-reducing laser on luminescence properties of InAs/GaAs quantum dots," *Journal of Crystal Growth,* vol. 234, pp. 354-358, 1// 2002.

[64] O. Qasaimeh, "Effect of doping on the optical characteristics of quantum-dot semiconductor optical amplifiers," *Journal of Lightwave Technology,* vol. 27, pp. 1978-1984, 2009.

[65] X. Q. Lv, P. Jin, W. Y. Wang, and Z. G. Wang, "Broadband external cavity tunable quantum dot lasers with low injection current density," *Optics Express,* vol. 18, pp. 8916-8922, 2010/04/26 2010.

[66] L. Qiaoyin, A. Abdullaev, M. Nawrocka, G. Wei-Hua, J. O'Callaghan, and J. F. Donegan, "Slotted Single Mode Lasers Integrated With a Semiconductor Optical Amplifier," *Photonics Technology Letters, IEEE,* vol. 25, pp. 564-567, 2013.

[67] J. Tatebayashi, M. Nishioka, and Y. Arakawa, "Over 1.5 μm light emission from InAs quantum dots embedded in InGaAs strain-reducing layer grown by metalorganic chemical vapor deposition," *Applied Physics Letters,* vol. 78, pp. 3469-3471, 2001.

[68] I. Young, E. Mohammed, J. T. Liao, A. M. Kern, S. Palermo, B. Block, *et al.*, "Optical I/O technology for tera-scale computing," *Solid-State Circuits, IEEE Journal of,* vol. 45, pp. 235-248, 2010.

[69] W. Bogaerts, R. Baets, P. Dumon, V. Wiaux, S. Beckx, D. Taillaert, *et al.*, "Nanophotonic waveguides in silicon-on-insulator fabricated with CMOS technology," *Lightwave Technology, Journal of*, vol. 23, pp. 401-412, 2005.

[70] S. McNab, N. Moll, and Y. Vlasov, "Ultra-low loss photonic integrated circuit with membrane-type photonic crystal waveguides," *Optics express*, vol. 11, pp. 2927-2939, 2003.

[71] M. Notomi, A. Shinya, S. Mitsugi, E. Kuramochi, and H. Ryu, "Waveguides, resonators and their coupled elements in photonic crystal slabs," *Optics express*, vol. 12, pp. 1551-1561, 2004.

[72] D. Liang, M. Fiorentino, S. Srinivasan, J. E. Bowers, and R. G. Beausoleil, "Low threshold electrically-pumped hybrid silicon microring lasers," *Selected Topics in Quantum Electronics, IEEE Journal of*, vol. 17, pp. 1528-1533, 2011.

[73] S. Mikhrin, A. Kovsh, I. Krestnikov, A. Kozhukhov, D. Livshits, N. Ledentsov, *et al.*, "High power temperature-insensitive 1.3 μm InAs/InGaAs/GaAs quantum dot lasers," *Semiconductor science and technology*, vol. 20, p. 340, 2005.

[74] D. Bimberg, M. Grundmann, and N. N. Ledentsov, *Quantum dot heterostructures*: John Wiley & Sons, 1999.

[75] M. Sugawara, N. Hatori, M. Ishida, H. Ebe, Y. Arakawa, T. Akiyama, *et al.*, "Recent progress in self-assembled quantum-dot optical devices for optical telecommunication: temperature-insensitive 10 Gb s− 1 directly modulated lasers and 40 Gb s− 1 signal-regenerative amplifiers," *Journal of Physics D: Applied Physics*, vol. 38, p. 2126, 2005.

[76] A. Y. Liu, C. Zhang, J. Norman, A. Snyder, D. Lubyshev, J. M. Fastenau, *et al.*, "High performance continuous wave 1.3 μm quantum dot lasers on silicon," *Applied Physics Letters*, vol. 104, p. 041104, 2014.

[77] T. Wang, H. Liu, A. Lee, F. Pozzi, and A. Seeds, "1.3-μm InAs/GaAs quantum-dot lasers monolithically grown on Si substrates," *Optics express*, vol. 19, pp. 11381-11386, 2011.

[78] A. Y. Liu, R. W. Herrick, O. Ueda, P. M. Petroff, A. C. Gossard, and J. E. Bowers, "Reliability of InAs/GaAs Quantum Dot Lasers Epitaxially Grown on Silicon," *Selected Topics in Quantum Electronics, IEEE Journal of*, vol. 21, pp. 1-8, 2015.

[79] K. Tanabe, D. Guimard, D. Bordel, S. Iwamoto, and Y. Arakawa, "Electrically pumped 1.3 μm room-temperature InAs/GaAs quantum dot lasers on Si substrates by metal-mediated wafer bonding and layer transfer," *Optics express*, vol. 18, pp. 10604-10608, 2010.

[80] K. Tanabe, D. Guimard, D. Bordel, S. Iwamoto, and Y. Arakawa, "Fabrication of electrically pumped InAs/GaAs quantum dot lasers on Si substrates by Au-mediated wafer bonding," *physica status solidi (c),* vol. 8, pp. 319-321, 2011.

[81] T. Tatsumi, K. Tanabe, K. Watanabe, S. Iwamoto, and Y. Arakawa, "1.3 μm InAs/GaAs quantum dot lasers on Si substrates by low-resistivity, Au-free metal-mediated wafer bonding," *Journal of Applied Physics,* vol. 112, p. 033107, 2012.

[82] F. Kish, D. Vanderwater, M. Peanasky, M. Ludowise, S. Hummel, and S. Rosner, "Low-resistance Ohmic conduction across compound semiconductor wafer-bonded interfaces," *Applied physics letters,* vol. 67, pp. 2060-2062, 1995.

[83] Y. Okuno, K. Uomi, M. Aoki, and T. Tsuchiya, "Direct wafer bonding of III-V compound semiconductors for free-material and free-orientation integration," *Quantum Electronics, IEEE Journal of,* vol. 33, pp. 959-969, 1997.

[84] F. Salomonsson, K. Streubel, J. Bentell, M. Hammar, D. Keiper, R. Westphalen, *et al.*, "Wafer fused p-InP/p-GaAs heterojunctions," *Journal of applied physics,* vol. 83, pp. 768-774, 1998.

[85] F. Shi, K.-L. Chang, J. Epple, C.-F. Xu, K. Cheng, and K. Hsieh, "Characterization of GaAs-based nn and pn interface junctions prepared by direct wafer bonding," *Journal of applied physics,* vol. 92, pp. 7544-7549, 2002.

[86] J. R. Bickford, D. Qiao, P. Yu, and S. Lau, "Electrical characterization of GaAs metal bonded to Si," *Applied physics letters,* vol. 89, p. 012106, 2006.

[87] H. Tan, C. Reaves, J. J. Dudley, A. L. Holmes Jr, D. Babić, E. L. Hu, *et al.*, "Low-temperature Pd direct bonding and electrical transport across InP-Pd-GaAs interfaces," in *Indium Phosphide and Related Materials, 1994. Conference Proceedings., Sixth International Conference on*, 1994, pp. 628-631.

[88] E. Yablonovitch, T. Sands, D. Hwang, I. Schnitzer, T. Gmitter, S. Shastry, *et al.*, "Van der Waals bonding of GaAs on Pd leads to a permanent, solid-phase-topotaxial, metallurgical bond," *Applied Physics Letters,* vol. 59, pp. 3159-3161, 1991.

[89] M. Maximov, A. Tsatsul'nikov, B. Volovik, D. Sizov, Y. M. Shernyakov, I. Kaiander, *et al.*, "Tuning quantum dot properties by activated phase separation of an InGa (Al) As alloy grown on InAs stressors," *Physical Review B,* vol. 62, p. 16671, 2000.

[90] A. A. Ukhanov, A. Stintz, P. G. Eliseev, and K. J. Malloy, "Comparison of the carrier induced refractive index, gain, and linewidth enhancement factor in quantum dot and quantum well lasers," *Applied Physics Letters*, vol. 84, pp. 1058-1060, 2004.

[91] M. Tang, J. Wu, S. Chen, Q. Jiang, A. J. Seeds, H. Liu, *et al.*, "Optimisation of the dislocation filter layers in 1.3-μm InAs/GaAs quantum-dot lasers monolithically grown on Si substrates," *IET Optoelectronics*, vol. 9, pp. 61-64, 2015.

[92] A. Lee, Q. Jiang, M. Tang, A. Seeds, and H. Liu, "Continuous-wave InAs/GaAs quantum-dot laser diodes monolithically grown on Si substrate with low threshold current densities," *Optics express*, vol. 20, pp. 22181-22187, 2012.

[93] Z. Mi, P. Bhattacharya, J. Yang, and K. Pipe, "Room-temperature self-organised In0. 5Ga0. 5As quantum dot laser on silicon," *Electronics letters*, vol. 41, pp. 742-744, 2005.

[94] S. M. Sze and K. K. Ng, *Physics of semiconductor devices*: John Wiley & Sons, 2006.

[95] A. P. Neto, H. Vargas, N. Leite, and L. Miranda, "Photoacoustic characterization of semiconductors: transport properties and thermal diffusivity in GaAs and Si," *Physical Review B*, vol. 41, p. 9971, 1990.

[96] G.-H. Duan, S. Olivier, S. Malhouitre, A. Accard, P. Kaspar, G. de Valicourt, *et al.*, "New Advances on Heterogeneous Integration of III–V on Silicon," *Journal of Lightwave Technology*, vol. 33, pp. 976-983, 2015.

[97] M. N. Sysak, H. Park, A. W. Fang, J. E. Bowers, R. Jones, O. Cohen, *et al.*, "Experimental and theoretical thermal analysis of a hybrid silicon evanescent laser," *Optics Express*, vol. 15, pp. 15041-15046, 2007.

[98] C.-Y. Jin, T. J. Badcock, H.-Y. Liu, K. M. Groom, R. J. Royce, D. J. Mowbray, *et al.*, "Observation and modeling of a room-temperature negative characteristic temperature 1.3-m p-type modulation-doped quantum-dot laser," *Quantum Electronics, IEEE Journal of*, vol. 42, pp. 1259-1265, 2006.

[99] M. Sugawara and M. Usami, "Quantum dot devices: Handling the heat," *Nature Photonics*, vol. 3, pp. 30-31, 2009.

[100] H. Yang, D. Zhao, S. Chuwongin, J. H. Seo, W. Yang, Y. Shuai, *et al.*, "Transfer-printed stacked nanomembrane lasers on silicon," *Nature Photonics*, vol. 6, pp. 617-622, 2012.

[101] Z. Mi, P. Bhattacharya, J. Yang, and K. Pipe, "Room-temperature self-organised In< sub> 0.5</sub> Ga< sub> 0.5</sub> As quantum dot laser on silicon," *Electronics letters*, vol. 41, pp. 742-744, 2005.

[102] D. Ahn, C. Hong, J. Liu, W. Giziewicz, M. Beals, L. C. Kimerling, *et al.*, "High performance, waveguide integrated Ge photodetectors," *Optics Express,* vol. 15, pp. 3916-3921, 2007.

[103] T. Wang, H. Liu, A. Lee, F. Pozzi, and A. Seeds, "1.3-?m InAs/GaAs quantum-dot lasers monolithically grown on Si substrates," *Opt. Express,* vol. 19, pp. 11381-11386, 06/06 2011.

[104] M. Zetian, Y. Jun, P. Bhattacharya, Q. Guoxuan, and M. Zhenqiang, "High-Performance Quantum Dot Lasers and Integrated Optoelectronics on Si," *Proceedings of the IEEE,* vol. 97, pp. 1239-1249, 2009.

[105] N. Yamamoto, K. Akahane, T. Kawanishi, R. Katouf, and H. Sotobayashi, "Quantum Dot Optical Frequency Comb Laser with Mode-Selection Technique for 1-mum Waveband Photonic Transport System," *Japanese Journal of Applied Physics, Volume 49, Issue 4, pp. 04DG03-04DG03-4 (2010).* vol. 49, 2010.

[106] G. L. Wojcik, D. Yin, A. R. Kovsh, A. E. Gubenko, I. L. Krestnikov, S. S. Mikhrin, *et al.*, "A single comb laser source for short reach WDM interconnects," in *SPIE OPTO: Integrated Optoelectronic Devices*, 2009, pp. 72300M-72300M-12.

[107] C.-S. Lee, W. Guo, D. Basu, and P. Bhattacharya, "High performance tunnel injection quantum dot comb laser," *Applied Physics Letters,* vol. 96, p. 101107, 2010.

[108] W. Bogaerts, R. Baets, P. Dumon, V. Wiaux, S. Beckx, D. Taillaert, *et al.*, "Nanophotonic waveguides in silicon-on-insulator fabricated with CMOS technology," *Journal of Lightwave Technology,* vol. 23, pp. 401-412, 2005.

[109] S. J. McNab, N. Moll, and Y. A. Vlasov, "Ultra-low loss photonic integrated circuit with membrane-type photonic crystal waveguides," *Optics express,* vol. 11, pp. 2927-2939, 2003.

[110] S. Saeedi and A. Emami, "Silicon-photonic PTAT temperature sensor for micro-ring resonator thermal stabilization," *Optics express,* vol. 23, pp. 21875-21883, 2015.

[111] D. Liang, M. Fiorentino, S. Srinivasan, J. E. Bowers, and R. G. Beausoleil, "Low threshold electrically-pumped hybrid silicon microring lasers," *IEEE Journal of Selected Topics in Quantum Electronics,* vol. 17, pp. 1528-1533, 2011.

[112] Y. Wan, Q. Li, A. Y. Liu, W. W. Chow, A. C. Gossard, J. E. Bowers, *et al.*, "Sub-wavelength InAs quantum dot micro-disk lasers epitaxially grown on exact Si (001) substrates," *Applied Physics Letters,* vol. 108, p. 221101, 2016.

[113] A. Y. Liu, J. Peters, X. Huang, D. Jung, J. Norman, M. L. Lee, *et al.*, "Electrically pumped continuous-wave 1.3 μm quantum-dot lasers epitaxially grown on on-axis (001) GaP/Si," *Optics Letters,* vol. 42, pp. 338-341, 2017.

[114] Z. Wang, R. Yao, S. F. Preble, C.-S. Lee, L. F. Lester, and W. Guo, "High performance InAs quantum dot lasers on silicon substrates by low temperature Pd-GaAs wafer bonding," *Applied Physics Letters,* vol. 107, p. 261107, 2015.

[115] P. Vasil'ev, "Ultrafast Laser Diodes: Fundamentals and Applications," *Artech House, London,* 1995.

[116] A. W. Fang, B. R. Koch, K.-G. Gan, H. Park, R. Jones, O. Cohen, *et al.*, "A racetrack mode-locked silicon evanescent laser," *Optics express,* vol. 16, pp. 1393-1398, 2008.

[117] B. R. Koch, A. W. Fang, O. Cohen, and J. E. Bowers, "Mode-locked silicon evanescent lasers," *Optics express,* vol. 15, pp. 11225-11233, 2007.

[118] X. Huang, A. Stintz, H. Li, L. Lester, J. Cheng, and K. Malloy, "Passive mode-locking in 1.3 μm two-section InAs quantum dot lasers," *Applied Physics Letters,* vol. 78, pp. 2825-2827, 2001.

[119] E. Rafailov, M. Cataluna, W. Sibbett, N. Il'inskaya, Y. M. Zadiranov, A. Zhukov, *et al.*, "High-power picosecond and femtosecond pulse generation from a two-section mode-locked quantum-dot laser," *Applied Physics Letters,* vol. 87, p. 081107, 2005.

[120] J. Mee, M. Crowley, N. Patel, D. Murrell, R. Raghunathan, A. Aboketaf, *et al.*, "A passively mode-locked quantum-dot laser operating over a broad temperature range," *Applied Physics Letters,* vol. 101, p. 071112, 2012.

[121] A. A. Aboketaf, A. W. Elshaari, and S. F. Preble, "Optical time division multiplexer on silicon chip," *Optics express,* vol. 18, pp. 13529-13535, 2010.

[122] X. Huang, A. Stintz, H. Li, A. Rice, G. Liu, L. Lester, *et al.*, "Bistable Operation of a Two-Section 1.3-mum InAs Quantum Dot Laser-Absorption Saturation and the Quantum Confined Stark Effect," *IEEE journal of quantum electronics,* vol. 37, pp. 414-417, 2001.

[123] M. Tahvili, L. Du, M. Heck, R. Nötzel, M. Smit, and E. Bente, "Dual-wavelength passive and hybrid mode-locking of 3, 4.5 and 10 GHz InAs/InP (100) quantum dot lasers," *Optics express,* vol. 20, pp. 8117-8135, 2012.

[124] Y. Li, L. F. Lester, D. Chang, C. Langrock, M. Fejer, and D. J. Kane, "Characteristics and instabilities of mode-locked quantum-dot diode lasers," *Optics express,* vol. 21, pp. 8007-8017, 2013.

[125] M. Margalit, M. Orenstein, G. Eisenstein, and V. Mikhaelshvili, "Injection locking of an actively mode-locked semiconductor laser," *Optics letters*, vol. 19, pp. 2125-2127, 1994.

[126] G.-H. Duan, C. Jany, A. Le Liepvre, A. Accard, M. Lamponi, D. Make, *et al.*, "Hybrid III--V on Silicon Lasers for Photonic Integrated Circuits on Silicon," *Selected Topics in Quantum Electronics, IEEE Journal of,* vol. 20, pp. 158-170, 2014.

[127] G. Roelkens, U. Dave, A. Gassenq, N. Hattasan, C. Hu, B. Kuyken, *et al.*, "Silicon-based photonic integration beyond the telecommunication wavelength range," *Selected Topics in Quantum Electronics, IEEE Journal of,* vol. 20, pp. 394-404, 2014.

[128] Y. Arakawa, T. Nakamura, Y. Urino, and T. Fujita, "Silicon photonics for next generation system integration platform," *Communications Magazine, IEEE,* vol. 51, pp. 72-77, 2013.

[129] T. Kita, N. Yamamoto, T. Kawanishi, and H. Yamada, "Ultra-compact wavelength-tunable quantum-dot laser with silicon-photonics double ring filter," *Applied Physics Express,* vol. 8, p. 062701, 2015.

[130] S. Yang, Y. Zhang, Q. Li, X. Zhu, K. Bergman, P. Magill, *et al.*, "Quantum dot semiconductor optical amplifier/silicon external cavity laser for O-band high-speed optical communications," *Optical Engineering,* vol. 54, pp. 026102-026102, 2015.

[131] S. Yang, Y. Zhang, D. W. Grund, G. A. Ejzak, Y. Liu, A. Novack, *et al.*, "A single adiabatic microring-based laser in 220 nm silicon-on-insulator," *Optics express,* vol. 22, pp. 1172-1180, 2014.

[132] Y. Zhang, S. Yang, X. Zhu, Q. Li, H. Guan, P. Magill, *et al.*, "Quantum dot SOA/silicon external cavity multi-wavelength laser," *Optics express,* vol. 23, pp. 4666-4671, 2015.

[133] A. Zilkie, P. Seddighian, B. Bijlani, W. Qian, D. Lee, S. Fathololoumi, *et al.*, "Power-efficient III-V/Silicon external cavity DBR lasers," *Optics express,* vol. 20, pp. 23456-23462, 2012.

[134] J. H. Lee, I. Shubin, J. Yao, J. Bickford, Y. Luo, S. Lin, *et al.*, "High power and widely tunable Si hybrid external-cavity laser for power efficient Si photonics WDM links," *Optics express,* vol. 22, pp. 7678-7685, 2014.

[135] Y. Zhang, S. Yang, H. Guan, A. E.-J. Lim, G.-Q. Lo, P. Magill, *et al.*, "Sagnac loop mirror and micro-ring based laser cavity for silicon-on-insulator," *Optics express,* vol. 22, pp. 17872-17879, 2014.

[136] L. Goldberg, H. F. Taylor, A. Dandridge, J. F. Weller, and R. O. Miles, "Spectral characteristics of semiconductor lasers with optical feedback," *Microwave Theory and Techniques, IEEE Transactions on,* vol. 30, pp. 401-410, 1982.

[137] D. Chen, Z. Fang, H. Cai, J. Geng, and R. Qu, "Instabilities in a grating feedback external cavity semiconductor laser," *Optics express,* vol. 16, pp. 17014-17020, 2008.

[138] R. Lang and K. Kobayashi, "External optical feedback effects on semiconductor injection laser properties," *Quantum Electronics, IEEE Journal of,* vol. 16, pp. 347-355, 1980.

[139] J.-D. Park, D.-S. Seo, and J. G. McInerney, "Self-pulsations in strongly coupled asymmetric external cavity semiconductor lasers," *Quantum Electronics, IEEE Journal of,* vol. 26, pp. 1353-1362, 1990.

[140] W. Loh, Y. Ozeki, and C. L. Tang, "High-frequency polarization self-modulation and chaotic phenomena in external cavity semiconductor lasers," *Applied Physics Letters,* vol. 56, pp. 2613-2615, 1990.

[141] L. Coldren, K. Furuya, B. Miller, and J. Rentschler, "Etched mirror and groove-coupled GaInAsP/InP laser devices for integrated optics," *IEEE Journal of Quantum Electronics,* vol. 18, pp. 1679-1688, 1982.

[142] D. C. Byrne, J. P. Engelstaedter, W.-H. Guo, Q. Y. Lu, B. Corbett, B. Roycroft, *et al.*, "Discretely tunable semiconductor lasers suitable for photonic integration," *IEEE Journal of Selected Topics in Quantum Electronics,* vol. 15, pp. 482-487, 2009.

[143] C.-S. Lee, T. Frost, W. Guo, and P. Bhattacharya, "High Temperature Stable Operation of 1.3-m Quantum-Dot Laser Integrated With Single-Mode Tapered Si N Waveguide," *IEEE Photonics Technology Letters,* vol. 24, pp. 918-920, 2012.

[144] M. Green, A. Behfar, A. Morrow, A. Schremer, and C. Stagarescu, "Horizontal cavity vertically emitting lasers with integrated monitor photodiodes," in *Asia-Pacific Optical Communications*, 2006, pp. 63520U-63520U-8.

[145] T. Windhorn and W. Goodhue, "Monolithic GaAs/AlGaAs diode laser/deflector devices for light emission normal to the surface," *Applied physics letters,* vol. 48, pp. 1675-1677, 1986.

[146] H. Liu, T. Wang, Q. Jiang, R. Hogg, F. Tutu, F. Pozzi, *et al.*, "Long-wavelength InAs/GaAs quantum-dot laser diode monolithically grown on Ge substrate," *Nature Photonics,* vol. 5, pp. 416-419, 2011.

[147] J. Yang, Z. Mi, and P. Bhattacharya, "Groove-coupled InGaAs/GaAs quantum dot laser/waveguide on silicon," *Journal of lightwave technology,* vol. 25, pp. 1826-1831, 2007.

[148] J. Rossler, Y. Royter, D. Mull, W. Goodhue, and C. Fonstad, "Bromine ion-beam-assisted etching of InP and GaAs," *Journal of Vacuum Science & Technology B,* vol. 16, pp. 1012-1017, 1998.

[149] J. Donnelly, K. Anderson, J. Woodhouse, W. Goodhue, D. Yap, M. Gaidis, *et al.*, "Some applications of ion beams in III-V compound semiconductor device fabrication," in *MRS Proceedings*, 1988, p. 421.

[150] P. Vettiger, M. K. Benedict, G.-L. Bona, P. Buchmann, E. C. Cahoon, K. Datwyler, *et al.*, "Full-wafer technology-A new approach to large-scale laser fabrication and integration," *IEEE journal of quantum electronics,* vol. 27, pp. 1319-1331, 1991.

[151] M. Uchida, S. Ishikawa, N. Takado, and K. Asakawa, "An AlGaAs laser with high-quality dry etched mirrors fabricated using an ultrahigh vacuum in situ dry etching and deposition processing system," *IEEE journal of quantum electronics,* vol. 24, pp. 2170-2177, 1988.

[152] J. Yang, P. Bhattacharya, and Z. Wu, "Monolithic integration of InGaAs–GaAs quantum-dot laser and quantum-well electroabsorption modulator on silicon," *IEEE Photonics Technology Letters,* vol. 19, pp. 747-749, 2007.

[153] S. Ou, J. Yang, and M. Jansen, "5 W GaAs/GaAlAs laser diodes with a reactive ion etched facet," *Applied physics letters,* vol. 57, pp. 1861-1863, 1990.

[154] S. Mokkapati, M. Buda, H. H. Tan, and C. Jagadish, "Effect of Auger recombination on the performance of p-doped quantum dot lasers," *Applied Physics Letters,* vol. 88, p. 161121, 2006.

[155] P. Bhattacharya, *Semiconductor optoelectronic devices*: Prentice-Hall, Inc., 1994.

[156] G. Liu, A. Stintz, H. Li, K. Malloy, and L. Lester, "Extremely low room-temperature threshold current density diode lasers using InAs dots in In0. 15Ga0. 85As quantum well," *Electron. Lett,* vol. 35, pp. 1163-1165, 1999.

[157] B. Song, C. Stagarescu, S. Ristic, A. Behfar, and J. Klamkin, "3D integrated hybrid silicon laser," *Optics Express,* vol. 24, pp. 10435-10444, 2016.

[158] A. W. Fang, E. Lively, Y.-H. Kuo, D. Liang, and J. E. Bowers, "A distributed feedback silicon evanescent laser," *Optics express,* vol. 16, pp. 4413-4419, 2008.

[159] S. Keyvaninia, G. Roelkens, D. Van Thourhout, C. Jany, M. Lamponi, A. Le Liepvre, *et al.*, "Demonstration of a heterogeneously integrated III-V/SOI single wavelength tunable laser," *Optics express,* vol. 21, pp. 3784-3792, 2013.

[160] G.-H. Duan, C. Jany, A. Le Liepvre, A. Accard, M. Lamponi, D. Make, *et al.*, "Hybrid III--V on Silicon Lasers for Photonic Integrated Circuits on Silicon," *IEEE Journal of selected topics in quantum electronics,* vol. 20, pp. 158-170, 2014.

[161] K. Ohira, K. Kobayashi, N. Iizuka, H. Yoshida, M. Ezaki, H. Uemura, *et al.*, "On-chip optical interconnection by using integrated III-V laser diode and photodetector with silicon waveguide," *Optics express,* vol. 18, pp. 15440-15447, 2010.

[162] W. D. Sacher, J. C. Mikkelsen, P. Dumais, J. Jiang, D. Goodwill, X. Luo, *et al.*, "Tri-layer silicon nitride-on-silicon photonic platform for ultra-low-loss crossings and interlayer transitions," *Optics express,* vol. 25, pp. 30862-30875, 2017.

[163] P. Dong, W. Qian, H. Liang, R. Shafiiha, D. Feng, G. Li, *et al.*, "Thermally tunable silicon racetrack resonators with ultralow tuning power," *Optics express,* vol. 18, pp. 20298-20304, 2010.

[164] G. Li, X. Zheng, J. Yao, H. Thacker, I. Shubin, Y. Luo, *et al.*, "25Gb/s 1V-driving CMOS ring modulator with integrated thermal tuning," *Optics Express,* vol. 19, pp. 20435-20443, 2011.

[165] Y. Zhang, S. Yang, M. J. Hochberg, and T. Baehr-Jones, "Quantum dot SOA-silicon external cavity multi-wavelength laser," ed: Google Patents, 2016.

[166] B. Stern, X. Ji, A. Dutt, and M. Lipson, "Compact narrow-linewidth integrated laser based on a low-loss silicon nitride ring resonator," *Optics letters,* vol. 42, pp. 4541-4544, 2017.

[167] J. Hulme, J. Doylend, and J. Bowers, "Widely tunable Vernier ring laser on hybrid silicon," *Optics express,* vol. 21, pp. 19718-19722, 2013.

[168] D. Gready, G. Eisenstein, V. Ivanov, C. Gilfert, F. Schnabel, A. Rippien, *et al.*, "High speed 1.55 μm InAs/InGaAlAs/InP quantum dot lasers," *IEEE Photonics Technology Letters,* vol. 26, pp. 11-13, 2014.

[169] D. Arsenijević and D. Bimberg, "Quantum-dot lasers for 35 Gbit/s pulse-amplitude modulation and 160 Gbit/s differential quadrature phase-shift keying," in *Semiconductor Lasers and Laser Dynamics VII*, 2016, p. 98920S.

[170] Y. Tanaka, M. Ishida, K. Takada, T. Yamamoto, H.-z. Song, Y. Nakata, *et al.*, "25 Gbps Direct Modulation in 1.3-? m InAs/GaAs High-density Quantum Dot Lasers," in *Conference on Lasers and Electro-Optics*, 2010, p. CTuZ1.

[171] M. Moehrle, H. Klein, C. Bornholdt, G. Przyrembel, A. Sigmund, W.-D. Molzow, *et al.*, "InGaAlAs RW-based electro-absorption-modulated DFB-lasers for high-speed applications," in *Semiconductor Lasers and Laser Dynamics VI*, 2014, p. 913419.

[172] W. Liu, R. S. Kim, B. Liang, D. L. Huffaker, and H. R. Fetterman, "High-speed InAs quantum-dot electrooptic phase modulators," *IEEE Photonics Technology Letters*, vol. 23, pp. 1748-1750, 2011.

[173] A. A. Aboketaf, L. Cao, D. Adams, A. W. Elshaari, S. F. Preble, M. T. Crowley, *et al.*, "Hybrid OTDM and WDM for multicore optical communication," in *Green Computing Conference (IGCC), 2012 International*, 2012, pp. 1-5.